AD-A241 756

PL-TR-91-2174

MEASUREMENT AND INTERPRETATION OF CONTAMINANT RADIATIONS
IN THE SPACECRAFT ENVIRONMENT

I. L. Kofsky
D. L. A. Rall
R. B. Sluder

DTIC
ELECTE
OCT 16 1991
S D
D

PhotoMetrics, Inc.
4 Arrow Drive
Woburn, MA 01801-2067

28 June 1991

Final Report
01 June 1988 -- 31 May 1991

91-13237

Approved for public release; distribution unlimited.

PHILLIPS LABORATORY
AIR FORCE SYSTEMS COMMAND
HANSCOM AFB, MASSACHUSETTS 01731-5000

"This technical report has been reviewed and is approved for publication"

Edmond Murad
EDMOND MURAD
Contract Manager

Charles P. Pike
CHARLES P. PIKE, Chief
Spacecraft Interactions Branch

Charles P. Pike
CHARLES P. PIKE, Chief
Spacecraft Interactions Branch

This report has been reviewed by the ESD Public Affairs Office (PA) and is releasable to the National Technical Information Service (NTIS)

REPORT DOCUMENTATION PAGE

Public reporting burden for this collection of information is estimated to average 1 hour per response, including the time for reviewing instructions, searching existing data sources, gathering and maintaining the data needed, and completing and reviewing the collection of information. Send comments regarding this burden estimate or any other aspect of this collection of information, including suggestions for reducing this burden, to Washington Headquarters Services, Directorate for Information Operations and Reports, 1215 Jefferson Davis Highway, Suite 1204, Arlington, VA 22202-4302, and to the Office of Management and Budget, Paperwork Reduction Project (0704-0188), Washington, DC 20503

1. AGENCY USE ONLY (Leave blank)	2. REPORT DATE	3. REPORT TYPE AND DATES COVERED
	28 June 1991	Final (1 Jun 88 - 31 May 91)

4. TITLE AND SUBTITLE	5. FUNDING NUMBERS
Measurement and Interpretation of Contaminant Radiations in the Spacecraft Environment	PE 63220C PR S321 TA 31 WU AA Contract No. F19628-88-C-0070

6. AUTHOR(S)

I. L. Kofsky
D. L. A. Rall
R. B. Sluder

7. PERFORMING ORGANIZATION NAME(S) AND ADDRESS(ES)	8. PERFORMING ORGANIZATION REPORT NUMBER
PhotoMetrics, Inc. 4 Arrow Drive Woburn, MA 01801-2067	

9. SPONSORING/MONITORING AGENCY NAME(S) AND ADDRESS(ES)	10. SPONSORING/MONITORING AGENCY REPORT NUMBER
Phillips Laboratory Hanscom AFB, MA 01731-5000 Contract Manager Edmond Murad/PHK	PL-TR-91-2174

11. SUPPLEMENTARY NOTES

12a. DISTRIBUTION/AVAILABILITY STATEMENT	12b. DISTRIBUTION CODE
APPROVED FOR PUBLIC RELEASE: DISTRIBUTION UNLIMITED	

13. ABSTRACT (Maximum 200 words)

Video photographs and spectra of the optical radiations excited by reactions of the energetic exhaust gases from space shuttle's aspect-controlling bipropellant rocket engines with the orbital atmosphere are analyzed. The data were taken with the Air Force Maui Optical Station's cameras and a new imaging spectrograph as these 400 kgf Primary Reaction Control System thrusters operated in ram-wake-perpendicular to the trajectory sequences planned by Geophysics Directorate. Emission originated from a few km parallel and transverse to the symmetry axis of the exhaust; the surface brightness distributions from the firings to windward are well fit by Gaussians; and the total sterances determined by calibration against known stars were in the approximate ratio 10 (ram) : 5 (perpendicular) : 1 (wake), showing that the kinetic energy of the combustion products plays a major part in exciting chemiluminescence. Three orders of magnitude less radiation arose from the spacecraft region than from the much larger volume in which the exhaust interacts, from which the hard body appeared physically separated. The luminosity associated with thruster turnon and turnoff, which is presumably due to reactions of incompletely-burned monomethyl hydrazine rocket fuel with oxygen atoms, is characterized. Preliminary spectrum data indicate that the principal emitting species are NH(A $^3\Pi$), O(^{1}D), OH(X $^2\Pi$, v to ~6), and an unidentified source of bands-plus continuum between ~3600 and 4700Å that is responsible for most of the exposure. Some of the accompanying infrared radiant intensities are estimated.

14. SUBJECT TERMS		15. NUMBER OF PAGES
Rocket exhaust reactions	Video photometry	116
Thruster engines	Spacecraft optical signatures	16. PRICE CODE
Spacecraft contamination	Chemical kinetics	

17. SECURITY CLASSIFICATION OF REPORT	18. SECURITY CLASSIFICATION OF THIS PAGE	19. SECURITY CLASSIFICATION OF ABSTRACT	20. LIMITATION OF ABSTRACT
Unclassified	Unclassified	Unclassified	SAR

CLASSIFIED BY:

DECLASSIFY ON:

FOREWORD

This Final Report on USAF Phillips Laboratory/Geophysics Directorate Contract F19628-88-C-0070 documents research by PhotoMetrics to characterize the optical radiations excited by reactions with the atmosphere of the energetic combustion-product molecules from the thruster rockets that control the aspect and trajectory of Shuttle Orbiter and several other types of spacecraft of interest to DoD. The previous tasks on this program, which we reported in detail in Scientific Reports No. 1 and 2 (Ref's 1, 2; June 1989 and June 1990), are identified below.

We describe here progress in understanding the interaction of these gases with the local thermospheric O, N_2, and O^+ that resulted from analysis of visible-near ultraviolet images and spectra recorded from the Air Force's (Mt. Haleakala) Maui Optical Station. Section 1 is a brief review of the expected composition of the bipropellant rocket engine exhaust (which appears to contain incompletely combusted fuel) and the theory of reaction processes at its several-eV's relative translational energy (Ref 3), intended to provide technical background for interpreting the experiments. Section 2 describes the groundbased optical sensors and their calibration (Ref 2), particulars of which are also needed for analyzing the data. In Section 3 we review the spatial radiance distributions (a preliminary report is in Ref 4), which are in reasonable agreement with predictions of a detailed kinetic transport-excitation code model developed by Geophysics Directorate ("SOCRATES", Ref 5); and in Section 4 we present a preliminary report of very recently acquired spectral distributions, which indicate that some largely-unanticipated reactions are responsible for the luminosity. Section 5 quantifies the visible radiation from the surface and immediate vicinity of the low earth-orbiting space vehicle itself during and after the few-second periods when its thruster engines operated, which is of interest for discriminating this hard body from the very much larger volume of residual atmosphere in which its exhaust gases produce optical radiations, and Section 6 summarizes the program results to date and recommends further groundbased measurements.

The tasks previously documented were as follows.

1. (Ref 1)   Identification of the critical technical issues in measuring from ground stations the radiant intensities of ultraviolet hydroxyl (OH) electronic bands that are excited by reactions of water molecules, which besides being a major component of liquid-fueled control rocket exhaust are persistently outgassed from the spacecraft body. We concluded that acceptable signal/noise ratios could be achieved with relatively small-scale dedicated photometers operated at AMOS (or similar high-altitude observatories).

2. (Ref 1)   Preliminary design of an active probe of the concentrations of outgas H_2O in the near-vicinity of orbiting spacecraft, which is based on excitative photolysis of the water molecules by a powerful vacuum-ultraviolet lamp onboard. This approach to determining the local water vapor contamination, originated by GD/WSSI, is being implemented by DoD for environment monitoring in both the forthcoming Midcourse Space Experiment (which involves a longlived satellite) and a ballistic rocket-based experiment.

3. (Ref 1)   Assessment of the potential of measurements of the spectral irradiances resulting from sunlight scattering and thermal emission by particulate matter near orbiting spacecraft, for identifying the source(s) of this spaceborne material. We concluded that a synthetic database of the spectra from candidate such contaminant particles is the logical next step in qualifying this remote-sensing concept.

4. (Ref 2)   Complete reduction, analysis, and interpretation of shuttle- and groundbased low-light-level video images of fuel cell-product water vented from Orbiter near local dawn, recorded in an experiment planned and executed by WSSI in 1988. This work quantifies the processes by which the initially-coherent liquid stream partially vaporizes and quickly forms into a quasiconical cloud of ice/water droplets with two characteristic mean radii, which scatter solar photons as they slowly sublimate in the radiation field of low earth orbit. Preliminary results from this water-dump experiment have been reported in Ref 6 and at several space-community symposiums.

We also completed several lower-priority research tasks on contaminant radiations, whose results we communicated to WSSI in working memorandums. These included

--specifying measurements of the optical signal from earth-orbiting spacecraft debris illuminated by the sun or powerful laser beams;

--identifying the functions of a Military Man in Space in reconnaissance, characterization of optical backgrounds, docking and deploying subsatellites, and related on-orbit operations; and in particular

--planning the pointing/operational program of optical sensors to be carried on a space pallet located a few km from Shuttle Orbiter (the SPAS), based on computer-generated two-dimensional projections of the space vehicle and its surrounding radiating volumes (from thruster rocket exhaust, outgas, purposefully-released material,...) at its scheduled separation distance and aspect angles.

Previous related AFPL/GD-sponsored research by PhotoMetrics, Inc., on contaminant optical radiations in the spacecraft environment is reported in Ref 3. The topics considered were brightness distributions extracted from groundbased infrared images of a large thruster exhaust plume that developed in connection with re-entry of Shuttle Orbiter; the ultraviolet and infrared emissions expected to result from state-specific reactions of incident thermospheric

species catalyzed by exposed vehicle surfaces--in particular, the Lyman-Birge-Hopfield of bands N_2 that had initially been interpreted as midlatitude airglow (Ref 7); specification of the view geometry from onboard spacecraft that maximizes signal/noise ratios from these off-surface optical radiations; and the gas-phase reactions of thruster rocket exhaust species with the orbital atmosphere that we apply in this report's interpretation of the resulting UV-visible images and spectra.

TABLE OF CONTENTS

TABLE OF CONTENTS (concluded)

LIST OF FIGURES

LIST OF FIGURES (concluded)

LIST OF TABLES

SECTION 1

PREDICTED ABUNDANCES AND REACTIONS WITH THE ATMOSPHERE
OF PRCS ENGINE EXHAUST GASES

Overview, Purpose

This report presents initial results of analyses of images (Ref 4) and spectra (otherwise not yet formally reported) of the visible and near-ultraviolet emissions excited by collisions of the high kinetic energy gases exhausted from space shuttle's Primary Reaction Control System (PRCS) rocket engines with the oxygen and nitrogen species of the orbital atmosphere. The data were taken with long-focus intensified video cameras (Ref's 2, 6) and a specially designed imaging spectrograph at the Air Force Maui Optical Station (AMOS), principally with these aspect-controlling thrusters operated in a preplanned sequence of ram-wake-perpendicular to track firing directions as the spacecraft passed near the zenith at night. Table 1 is a listing of the principal shuttle missions and these optical sensors, with the directions of the symmetry axis of the thruster exhaust relative to the trajectory. Only a small fraction of this database has so far been addressed.

Video images taken with a narrow-field, low light level electronic camera precisely tracked on Orbiter (Ref 4) showed visible emission originating from a few km parallel and perpendicular to its flight path when the exhaust gas interaction reaches "steady state" about ½ s after engine turn-on (see later Fig's 16-17 and 23-29). The radiance distribution and total yield of visible photons were found to depend strongly on the angle between the centerline of the exhaust and the trajectory direction. (As was pointed out by GD/WSSI, the optical sterance--as well as the brightness pattern itself--can thus in principle determine this angle for surveillance-tracking applications.) Space-resolved emission spectra (acquired shortly before this report was prepared, and only partially reduced) indicated that the radiation producing these images comes from several molecular and atomic species, some of which were previously considered to be weakly excited; these spectra also showed a near-ultraviolet feature to which the groundbased cameras have little or no sensitivity. The primary focus of the work reported here is interpretation of these optical emissions, toward validating Geophysics Directorate's computer model of the transport and chemical reactions of control rocket exhaust and outgas-contaminant species near low earth orbiting spacecraft (SOCRATES, Ref's 4, 5).

In this first Section, we briefly review the information available about the composition of the high translational-energy PRCS combustion products as an input to re-statement of their reactions with the ambient atmosphere that could result in population of radiative upper states.

1

Table 1.   Groundbased Optical Data on PRCS Exhaust Interactions

Range to AMOS (km)	Elev. (°)	Orbit	Day	UT	Burn Sequence	Exhaust Direction	AATS Finder Camera	GEODSS Camera
				STS-29, Launched 15 March 1989				
860	22	65	76	15:34:38.24 to 15:34:38.36	Unsched	*	3° FOV Section 3	
				STS-33, Launched 23 November 1989				
<638	>26	21	328	07:09:15-39	unsched	W?	Yes	
531	34	21	328	07:09:46-49	A	R	Section's 3, 5	
515	36	21	328	07:09:54-59	A	W	Available	
508	37	21	328	07:10:02-06	A	U	Available	Yes
506	37	21	328	07:10:10-14	A	D	Saturation	
662	31	22	328	08:47:36-40	B	R	w/bright star	
651	32	22	328	08:47:45-49	B	W	Available	
644	33	22	328	08:47:53-56	B	U	Saturation	
646	33	22	328	08:48:01-04	B	D	Saturation	Yes
649	33	22	328	08:48:11	unsched	?	Available	
424	49	37	329	07:51:24-28	C	R	Available	
416	51	37	329	07:51:32-36	C	W	Available	Yes
418	51	37	329	07:51:40-44	C	D	Saturation	
427	49	37	329	07:51:48-52	C	U	Saturation	
	47	37	329	07:52:05-06	unsched	?	Available	
				STS-41, Launched 06 October 1990				
			Arizona Imager/Spectrograph, spectral data 3200-9000Å					
350	67- -50	--	280	13:20:33 13:21:04		RWUD		
				STS-38, Launched 17 November 1990				
		Arizona Imager/Spectrograph, spectral data centered near 3360 and 6300Å						
			321	07:24:12-36				

† R = Ram, W = Wake, U = Up perpendicular, D = Down perpendicular
* Engines F3U, R3D, L3D; refer to the text

Much of this background and predictive material appears in our report predating the AMOS measurements (Ref 3, Section 6); we summarize it here in the interest of internal consistency of this report of the initial data analysis.

Exhaust and Target Species

The 395 kgf-thrust (~10 megawatt) bipropellant engines burn monomethyl hydrazine fuel (MMH; $H_3CHN_2H_2$) with N_2O_4 oxidizer, exhausting 1420 g/s (3.5×10^{25} molecules/s) of combustion-product gas with calculated kinetic temperature 3000K and mean directed velocity 3.5 km/s relative to Shuttle Orbiter in a quasicone of half-flux angle about 25°. Figure 1 shows the positions and (approximately) the flow symmetry axes of the 38 individual bipropellant PRCS thrusters relative to the three orthogonal axes of this spacecraft, with their identifying numbers (the nomenclature is self-explanatory). Orbiter in fact only rarely operates in the "airplane" flight mode suggested in this diagram, that is, with its X direction (in NASA notation) oriented parallel to its trajectory and bay toward the zenith; wing-to-ram with nose-to-nadir, for example, leads to a more stable spacecraft aspect. During the engine firings its velocity was closely 7.8 km/s, and its altitude near 300 km; these burn times varied between ~0.2 and 5 s, 3.0 s being typical.

The mole fractions of neutral species in the rocket exhaust gas, as calculated from a computer model (CONTAM III, Ref's 8 - 10) that makes empirical corrections to the thermodynamic-equilibrium concentrations at the combustion temperature, is

H_2O	N_2	H_2	CO	CO_2	H	Other gases
0.33	0.31	0.16	0.13	0.04	0.02	*see below.*

The model from which these relative abundances of the major chemical constituents is calculated does not take into account further reactions that may be taking place beyond the high-temperature volume, or variations with angle from the symmetry axis of the exhaust. Furthermore, these figures have not been directly experimentally validated. The primary tests of the geometry and composition of the flow field were done in a large evacuable laboratory chamber using liquid-fuel engines of a closely similar design but only ~1/400 as much thrust as individual PRCS units (Ref's 8, 11), some major findings of which are as follows. (The results of these experiments were interpreted with the aid of CONTAM III.)

--NO is also present in the exhaust gas, possibly in high concentrations. This observation is in accordance with mass spectrometric measurements (Ref 12) of large fluxes of nitric oxide reaching Orbiter's payload bay (distant from the principal exhaust-interaction volumes) when the PRCS is operated. The angular distribution of NO appears to be broader
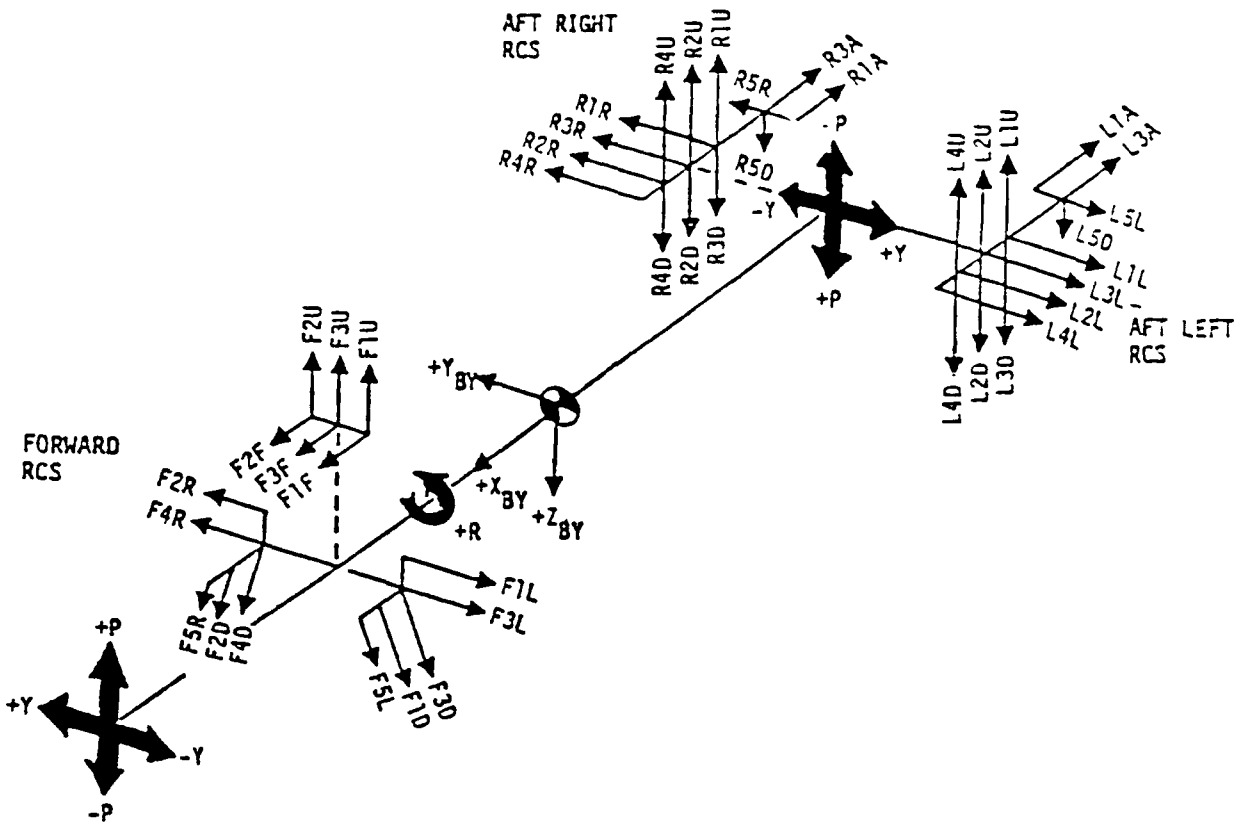
Figure 1.   Shuttle Orbiter PRCS thruster locations and approximate exhaust directions.

than those of the other principal combustion-product species (Ref's 8, 11), and its abundance varies during an engine firing.

--About 1% of the mass exhausted is unburned fuel and oxidizer, most probably primarily in 50-150 μm diameter droplets of MMH-nitrates. These particles are reported have about the same directed velocity as the gaseous products, with the larger ones tending to be closer to the symmetry axis. (In the hard vacuum of near-space, such high vapor pressure liquid droplets would rapidly evaporate.) This finding--which of course refers to the much smaller-scale bipropellant thruster rather than actual PRCS engines--is in at least qualitative agreement with the prediction of CONTAM III. The fraction of unreacted material increases during ˉ10 ms of engine startup and shutdown, that is, under transient operating conditions.

--Other fragments of incomplete combustion are also present in the exhaust, at low concentrations. These were indicated by largely-qualitative (and for that matter not particularly species-specific) mass spectrometry of exhaust gases frozen on a witness plate, which showed N_2H_2 (or NO), CH_2 (or N_2), CN_2H, and NO_2.

4

The nominal nighttime densities of the atmosphere's reacting and elastically scattering species at the altitude of the experiments are 4×10^8 O; 1×10^8 N$_2$; less than 10^7 O$_2$, NO, N$_2$(v > 0), N(^{4}S + ^{2}D), and H; and (roughly) 2×10^5 O$^+$ per cm^3. The kinetic energy in the center-of-mass system of the colliding pair, assuming free-molecule flow (so that the velocities of the spacecraft and exhaust simply add vectorially) and neglecting the ~1/10 eV rms translational energy of thermospheric gases, varies between more than 10 eV for ram-directed CO$_2$ on N$_2$ and 1/10 eV for wake-directed H$_2$ on O; particulars are in Ref 3. In practice, the gas densities in the actual flow field within ~1 km of the thruster exhaust nozzle are so high that strictly free-molecular transport does not obtain, and the complex interaction of the two particle streams can result in even higher (or lower) available reaction energy; this effect may in particular affect the yields from perpendicular-to-track engine firings, which produce sterances as high as one-half those toward ram (Ref 4) despite the substantially lower c.m. energy under free-molecule flow conditions.

Exhaust Reactions

We distinguish four general types of primary reactions between the combustion-product and atmospheric gases that would result in ultraviolet and visible radiations.

1) Neutral atom transfer, in which the rest-frame energy available to the colliding pair serves to overcome a potential barrier to formation of a new species in an excited electronic (or high-lying vibrational) state. A primary example (Ref 3) is

$$H_2O(\tilde{X}\ ^1A_1) + O(^3P) + 4.78 \text{ eV K.E.} \rightarrow OH(X\ ^2\Pi) + OH(A\ ^2\Sigma^+, v = 0).$$
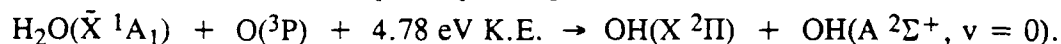
(OH(A) is the upper state of permitted molecular bands near 3000Å.)

2) Non-adiabatic collisions, otherwise known as T $\rightarrow$ E processes (without atom rearrangement), for which the cross-sections are generally considerably lower. Examples are

$$N_2 \text{ or } H_2O + O(^3P) \rightarrow O(^1D) + N_2 \text{ or } H_2O.$$
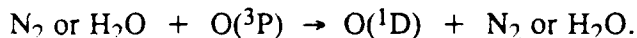
(O(^{1}D) is the upper state of the electric dipole-forbidden red doublet at 6300-6364Å.)

3) Processes involving breakdown of unburned or fragmented thruster fuel, which may be exothermic (or have low potential barriers) and thus proceed at rates less sensitive to the available translational energy. An example might be

$$\text{Monomethyl hydrazine} + O \rightarrow NH(A\ ^3\Pi) + \text{Products}.$$

(NH(A $\rightarrow$ X) transitions are prominent in the emission spectra; refer to Section 4.)

4) Excitative charge transfer with the (principal) ambient ionospheric species, which again may have low threshold. Examples are

$$H_2O(\tilde{X}) + O^+ (^4S) \rightarrow H_2O^+(\tilde{X}) + O(^1D) \qquad \text{or}$$

$$\rightarrow H_2O^+ (\nu_1, \nu_2, \nu_3, \text{ or combinations}) + O(^3P).$$
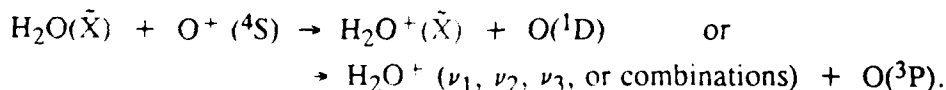
The latter reaction (Ref 13) would lead to only infrared photons, and since we are considering solely UV-visible emission data the comparably-vexed issue of vibrational excitation in charge-exchange (and non-adiabatic) collisions is not addressed here.

The newly-formed species may react further with the atmosphere 5) or with other exhaust molecules 6a), and furthermore fuel fragments may undergo excitation transfer from long-lived excited species present in the exhaust 6b). Examples would be

5) $H_2O^+ + e \rightarrow OH^{*,\dagger} + H$ (see in particular Ref's 14 and 15) and

6a) $O(^1D) + H_2O$ or $H_2 \rightarrow OH + OH$ or H   (as further discussed in Section 4) and

6b) $NH(X)$ or $CN(X) + N_2(A) \rightarrow NH(A)$ or $CN(B) + N_2(X)$.

Atom-transferring reactions 1) have been generally considered to be the principal source of visible radiations in the first few seconds after bipropellant thruster firings. However virtually no laboratory data are available on the state-specific cross-sections for those reactions of perceived primary interest, and existing theoretical guidance is not considered reliable. We derived in Ref 3 a set of the "most probable" such interchange processes by applying the restrictions on species abundance and molecular dynamics illustrated in Fig. 2. These physical arguments explicitly postponed consideration of exhaust interaction-reaction categories 2), 3), and 4) above, and do not address secondary processes of types 5) and 6).

With the further caveats and assumptions detailed in the analysis of Ref 3 (including that the potential energy of the excited state can be simply added to the threshold for production of the species in its ground state when extrapolating cross-sections from their typically ¼-eV laboratory-furnace values to the several eV available from collisions of ram exhaust), the reactions expected to result in the highest visible radiances are (Ref 4)

--$H_2O + O$ producing electronically- and vibrationally-excited OH radicals and

--CO_2 and $NO + O$ producing the upper (A) state of the Herzberg I bands of O_2 (and also the B state, leading to vacuum-ultraviolet O_2 Schumann-Runge bands).

The formalism of Fig. 2 also predicts some emission in

--CN red (A → X) bands,   and

--the yellow-green-infrared pseudocontinuum from NO_2 ($^2B_1$, $^2B_2$).

Similarly, the cross-sections for electronically non-adiabatic (otherwise endothermic, of type 2)) processes involving the exhaust and target atmospheric species are unknown. Much of the available guidance comes from extrapolations to much lower energies of data from neutral-neutral collisions that produce ions--which are relatively easily detected in the laboratory--rather than internally-excited atoms or molecules; from bombardments that result in excitation of H atoms (refer to the discussion in Ref 3); and from collisional de-excitation rates, whose inversion--that is, application of the thermodynamic principle of microscopic reversibility--

6
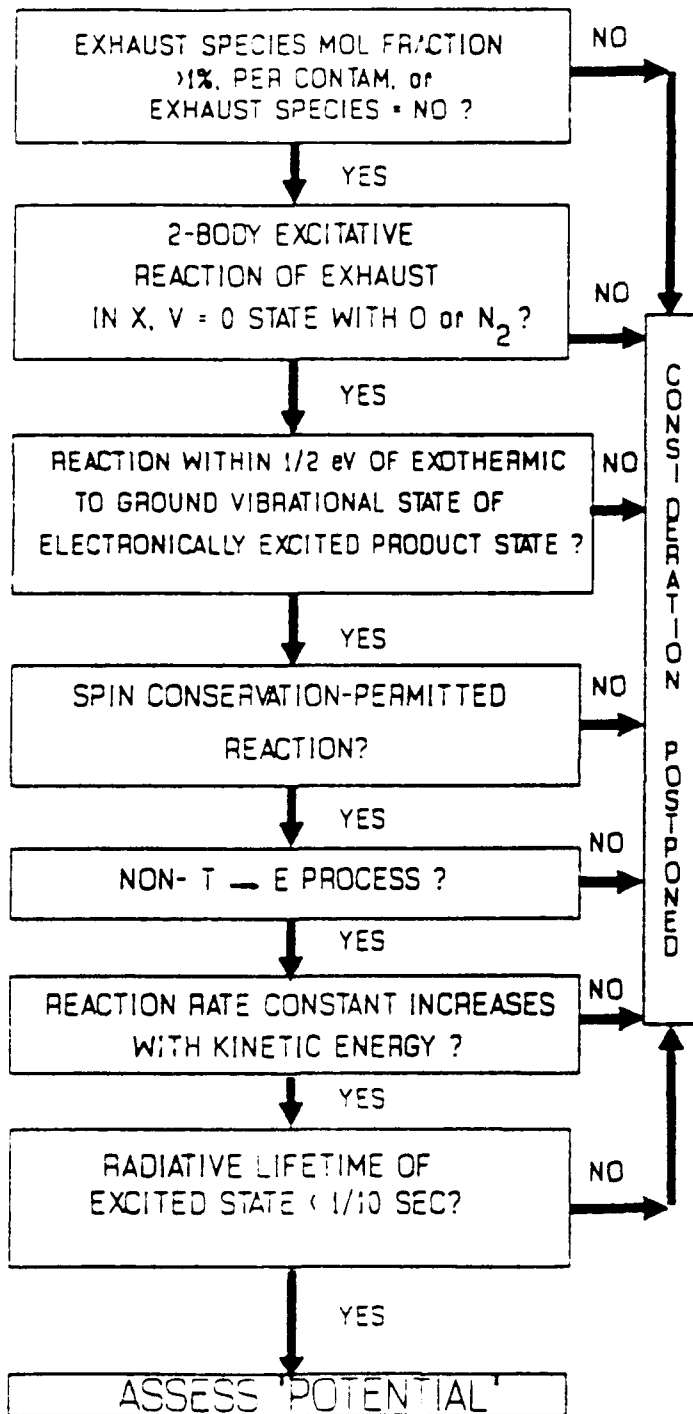
EXHAUST SPECIES MOL FRACTION >1%, PER CONTAM, or EXHAUST SPECIES = NO ? — **NO** → Principally model prediction./ Unburned fuel, ions, droplets could be present.

YES ↓

2-BODY EXCITATIVE REACTION OF EXHAUST IN X, V = 0 STATE WITH O or N_2 ? — **NO** → Highest concentration ambient target species./ Reactions with O_2, ions, $N_2(v)$, O^1D and N^2D could play a part. Internal excitations of 3000K exhaust gas could contribute.

YES ↓

REACTION WITHIN 1/2 eV OF EXOTHERMIC TO GROUND VIBRATIONAL STATE OF ELECTRONICALLY EXCITED PRODUCT STATE ? — **NO** → Rovibrational bands (principally IR) not considered./ Tail of velocity distribution could contribute.

YES ↓

SPIN CONSERVATION-PERMITTED REACTION? — **NO** → Cross sections for reactions violating spin conservation are lower.

YES ↓

NON- T → E PROCESS ? — **NO** → Cross sections for T → E processes are lower.

YES ↓

REACTION RATE CONSTANT INCREASES WITH KINETIC ENERGY ? — **NO** → $O + NO \rightarrow NO_2^x$, for example, is exothermic with a rate constant that decreases with increasing relative kinetic energy.

YES ↓

RADIATIVE LIFETIME OF EXCITED STATE < 1/10 SEC? — **NO** → Otherwise glow brightness reduced by delay of emission./ Energy transfer collisions could contribute.

YES ↓

ASSESS "POTENTIAL"

(Right-hand column: CONSIDERATION POSTPONED)

Figure 2.   Atom-transfer reactions considered in Ref 3. Some further excitative processes discussed in the text are underlined.

produces generally-reliable $T \rightarrow E$ excitation rates only in the rare cases in which the distribution of electronic, vibrational, rotational, and translational energy of all the product species has been measured. (For example, quenching of $O(^1D)$ by N_2 leads to an incompletely-understood distribution of kinetic energy and vibrational excitation of the N_2 molecules; in consequence although the lumped-parameter rate coefficient at room temperature, and even the "average" number of N_2 vibrons excited per collision, are known, the contribution of c.m. kinetic energy to the cross-section for the inverse reaction is in question.) Interpretation of the experiments leads to cross-section estimates as low as 10^{-5} and possibly as high as 10^{-3} those for elastic scattering, in which process the translational energy of the exhaust molecule may be reduced below thresholds for inelastic scattering that result in population of electronic (or high-lying vibrational) states. Nonetheless the large relative abundance of target oxygen atoms coupled with the 6 - 8 eV translational energy available in the initial collision of the principal exhaust species N_2, H_2O, CO_2, and CO with O (^3P) in ram-directed PRCS firings--and the still above-threshold energy after subsequent elastic collisions--may lead to measurable radiation from O atoms in the ground configuration (despite the fact that these "reactions" are further unfavored because they do not conserve spin angular momentum).

Recent laboratory experiments (Ref 16) have shown that in the <u>charge-exchange reaction</u> 3) of O^+ with D_2O most of the few-eV rest-frame translational energy is converted to internal excitation of the product states (as is speculated, and applied, in Ref 13). This finding suggests that $O(^1D)$--1.97 eV above the ground state of O--and even $O(^1S)$--4.18 eV--, the sources of the red (6300-6364Å) and green (5577Å) "forbidden" transitions of atomic oxygen familiar from airglow and aurora, would be populated by the exhaust gases from near-ram thruster firings. The $O^+ \rightarrow H_2O^+$ charge-exchange cross-section at the direct-ram c.m. kinetic energy of 5.74 eV is 2×10^{-15} cm^2 (Ref 17), which is comparable with the cross-sections for elastic neutral-particle scattering and at least an order of magnitude greater than any of the excitative atom-exchange cross-sections that we estimated in Ref 3. Nonetheless, the low concentration of the charged target species-- $< 10^{-3}$ that of neutral O--must be taken into account in considering the yields in the oxygen emission lines that could result from the reactions between the H_2O in the exhaust and the O^+ of the ionosphere.

Incompletely-combusted <u>MMH fuel and its fragments</u> 4) would be expected to react rapidly with the highly-active ambient O atoms (see for example Ref 18). The resulting radiance distributions would furthermore show a different dependence on the direction of the thruster exhaust than those from the otherwise-endothermic processes 1) - 3), as the cross-sections for chemical reactions that have zero potential barrier tend to decrease with increasing relative velocity of the participants (and furthermore the cross sections for those with barriers

8

substantially less than the available kinetic energy would be less sensitive to the vector sum of velocities). Despite the existence of some information from both laboratory investigations and releases of hydrazine and amine compounds into the thermosphere, uncertainties in both the abundances of unreacted (with N_2O_4) fuel products under the real operation conditions of PRCS thrusters and the chemiluminous-reaction rates of these species lead to extremely large uncertainty in predictions of the spectral and spatial intensity distributions. Indeed, even when we are able to identify spectroscopically a radiating species--such as NH(A), as shown in Section 4--the database from chemical kinetics laboratory and rocket-stand experiments is insufficient for reliable assignment of the excitation mechanism; and furthermore, the information available about fuel-product reactions provides only limited guidance in interpreting complex, typically low signal-to-noise emission spectra.

The radiant intensities resulting from secondary processes 5) would be expected to be weak although potentially persistent, while those from 6) could in principle be strong. Excitation accompanying electron dissociative recombination of oxygen atom-containing molecules is well known to result in longlived emission of the forbidden red lines of O from the F-region ionosphere when it is contaminated by rocket-exhaust molecules (Ref's 14, 15 for example); in addition, we have observed slowly-decaying $O(^1S \rightarrow {}^1D)$ green line and OH vibrational fundamental (~ 2.8 μm) radiations from the interaction volume of rocket engine combustion-product H_2O and H_2 (Ref 15), both of which molecules react rapidly with the O^+ of the ionosphere. $O(^1D)$, whose radiative lifetime is 196 s, reacts with almost all the combustion-product gases to produce new chemical species, some of them in excited states (see Table 11). The idea appears to be well established (Ref 18) that collisional transfer of electronic excitation from longlived N_2 $(A^3\Sigma^+)$ molecules to ground-state species is the origin of the OH (A $\rightarrow$ X), NH (A $\rightarrow$ X), and some other molecular bands seen in amine-fueled laboratory flames; however, no theoretical or experimental evidence exists for appreciable concentrations of N_2 (A) precursor molecules (~ 6 eV above the ground electronic state, 2 s radiative lifetime) in the $\sim \frac{1}{4}$ eV kinetic temperature PRCS thruster exhaust gas.

SECTION 2

OPTICAL SENSORS

Introduction

The cameras and spectrograph were operated from the Air Force's Maui Optical Station (AMOS) atop Mt. Haleakala, HI (21° N, 204° E, 3000 m altitude). The angular fields, tracking mode, and other characteristics of the cameras are summarized in Table 2, and particulars of the optical site, data handling, and related experiment support issues are given in Ref 19. As the sun was below Shuttle Orbiter's horizon during the measurement periods the groundbased sensors are responding to emitted rather than scattered photons.

The video data, received in analog form, were accessed and reduced using PhotoMetrics' Datacube/MaxVision hardware-software (briefly described in Ref 2). This image processing system digitizes the photocurrents in frames or 1/60-s uninterlaced video fields (on an eight-bit, 0 to 255 linear scale), coadds-averages to improve signal-to-noise ratios, subtracts baseline/background, sums photocurrents over operator-selectable areas, compiles line profiles in arbitrary directions, and otherwise helps extract useful information-- for example, maximum radiance and total sterances--from the scene brightness distributions.

Imaging Spectrograph

This instrument, which had been designed-constructed-calibrated by the Lunar and Planetary Laboratory of the University of Arizona, was operated on a side mount of the 1.6 m AMOS-MOTIF tracking telescope. A small relay (field matching) lens beyond the principal focus of an 8 inch diameter f/5 aspheric (paraboloidal) Newtonian telescope images a strip of sky onto the slit of the spectrograph, whose f/1.2 concave holographic reflection grating disperses the image onto a 30 mm-square intensified-CCD focal plane. Monochromatic images of the spectrograph entrance slit cover 3 pixels x 192 pixels longitudinally on this detector array, and the "visible" spectrum extends over 384 pixels in the transverse direction. A backward projection of the slit's 1/60 x 1/16 (or 1/12)- degree elements onto a typical exhaust-interaction volume is in Fig. 3.

Spectral resolution (nominally 70-80Å) is as usual in part controlled by this number of picture elements subtended by the entrance slit, while spatial resolution in the "imaging" direction can be readily traded off against radiometric signal by coadding output photocurrents (in the software, under microprocessor control). (Two-dimensional spectral images can in principle be compiled at the expense of time resolution, by scanning the slit across the scene.)

Table 2. Characteristics of the AMOS Video Cameras*

	AATS		GEODSS
	Narrow Field	Wide Field	
Tracking	On the moving spacecraft		On the fixed star field
Field of View, Diagonal	0.5°	3.0°	6.0°
Star Motion, FoVs/frame	1/8	1/175	None
Observed Star Streak, FoVs	1/2	1/30	-1/100
Focal Plane Vignetting	Large (factor -2 over FoV)		Very small
Projection of Luminosity on FoV	Overfills	Small	Small
Self-consistency of Calibration against Known Stars	*Poor* 3 stars, M_v 6.8 to 9.1	*Fair* 12 stars, M_v 7.1 to 9.3	*Good* 20 stars, M_v 6.4 to 9.2

*Particulars of the imaging spectrograph, which like the AATS cameras is tracked on the spacecraft, are given in the text.
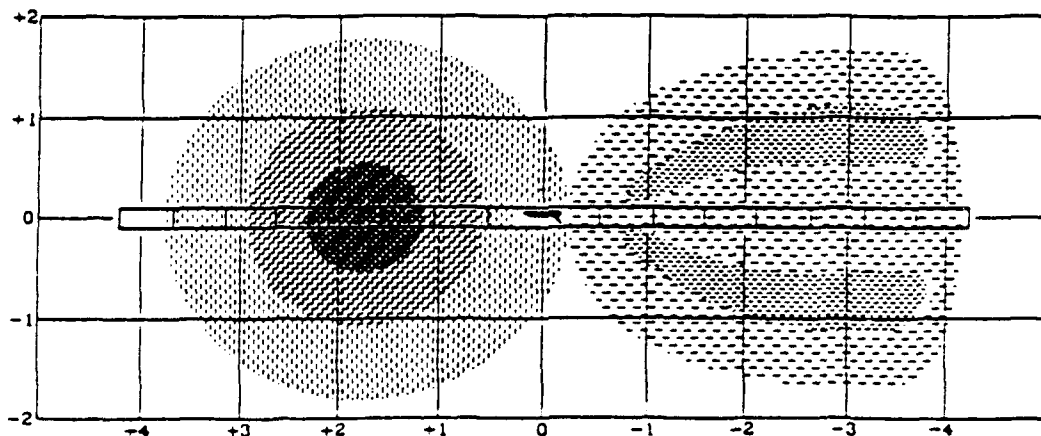
Figure 3. Projection of the field of view of the GD/Arizona imaging spectrograph on the radiating volumes in the ram and wake. The individual spectrograph channels extend over 0.50 km in the STS-41 data shown in Figure 4. At the time of the ram burn Orbiter was at 67.5° elevation and 70° azimuth and 314 km range.

The spectral response provided by the Lunar and Planetary Laboratory is included in Fig. 4. Electronic spectrographs of the same general design have been built by the Laboratory over the last seventeen years, primarily for airglow-aurora research; procedures are in place for checking and maintaining radiometric and wavelength calibration, using standard light sources.

Figure 4 reproduces typical raw spectrums from this Geophysics Directorate/Arizona instrument during a ram-directed engine firing, with nominal pointing as in Fig. 3. These count rates in each wavelength bin are then converted to spectral radiances (such as are shown in later Fig. 52) by applying the radiometric calibration-transfer factor of Fig. 4 and (if required) correcting for atmosphere transmissions such as are shown in Fig. 5. The imaging spectrograph differs in this regard from the AMOS low light level cameras, whose photometric response--which is varied to accommodate a wide range of mean scene brightnesses--we calibrated in the field against the irradiances from known stars.

MOS - MOTIF AATS Camera

The AMOS Acquisition Telescope Systems normally serve as finder cameras for the 1.2 and 1.6 m-diameter main AMOS telescopes. As is shown in Fig. 6, two separate, parallel-viewing optical systems with f/3-4 aperture ratio provide 3°-diagonal and 0.5°-diagonal (0.4° horizontally x 0.3°) image fields. A 6 inch-diameter catadioptic lens images the 3° field of view, and a 22 inch (56 cm) Richey-Chretien telescope images the 0.5° field; a flip mirror selects the light bundle relayed onto the 40 mm-diameter Intensified Silicon intensifier Target focal plane (Ref 2). (The 0.1° angular field achievable with a demagnifying lens (Fig. 6) was found to be too small to be effective in the experiments to characterize the exhaust interaction luminosity reported here.) Figure 5 shows the (S-20R) spectral response of this video display-compatible photodetector array, and the LOWTRAN transmission of the clear maritime subtropical atmosphere in paths to AMOS from Shuttle Orbiter at three zenith angles.

As the electronic gain of the AATS video camera may change over the engine firing sequence, we calibrated it against known stars in its image field by a procedure that is described in detail below.

GEODSS Camera

Ground-Based Electro-Optical Deep Space Surveillance cameras are routinely operated for USAF to identify and otherwise characterize sunlit earth-orbiting objects. The main (40-inch diameter) and auxiliary (15-inch clear aperture) camera units were on sidereally-driven mounts during the PRCS firing experiments, so that the star field backgrounds remain
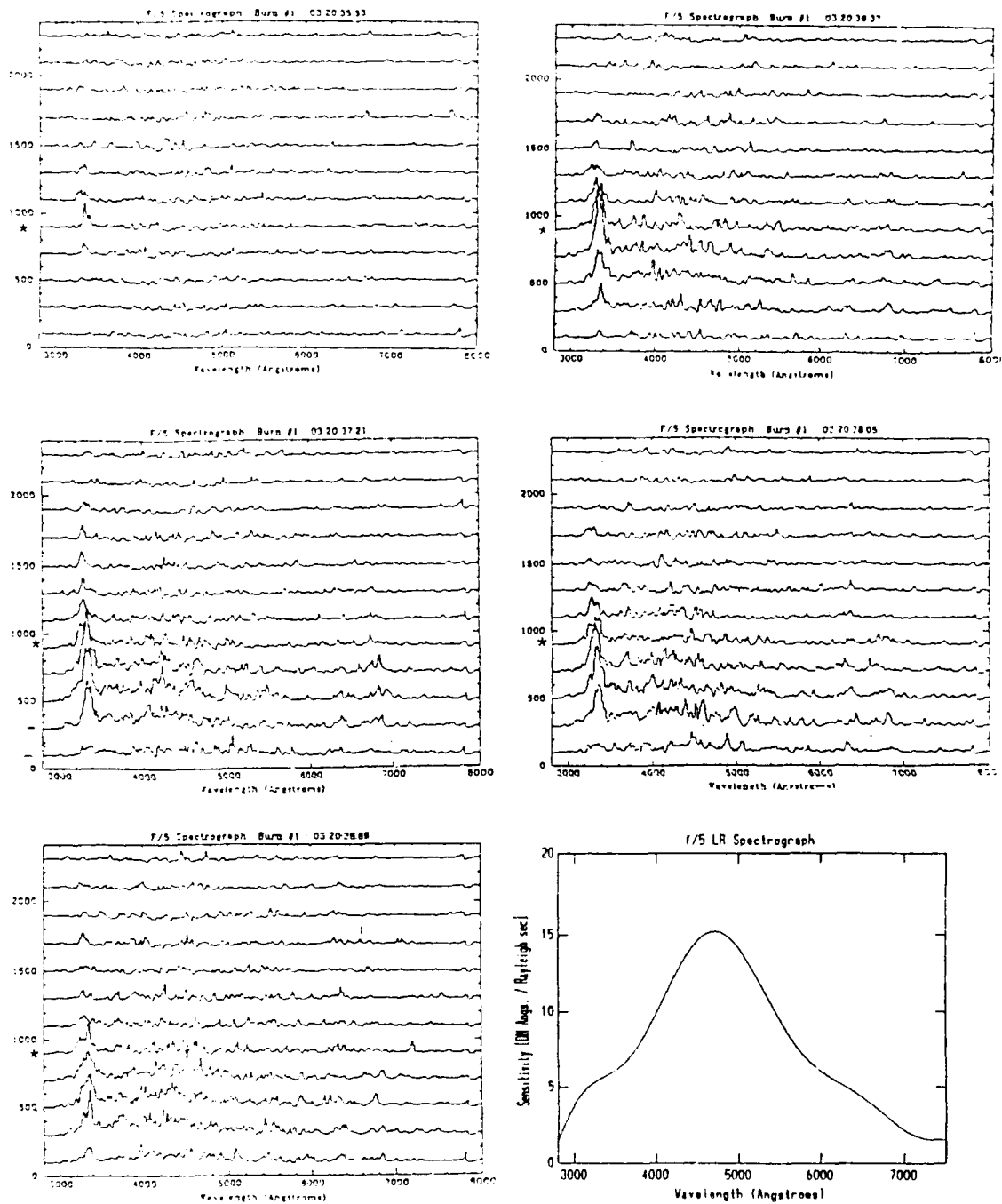
Figure 4.   Count-rate spectra from an STS-41 ram-directed engine firing, and instrument spectral response as determined by the Lunar and Planetary Laboratory (lower right). The times refer to the start of each 0.8-s exposure. Turn-on was at 03:20:36.25, turn-off at 03:20:39.25. The nominal position of Shuttle Orbiter in the spectral-images is indicated by *, and the ram direction is downward. DN on the ordinate refers to number of counts in the sample.

13
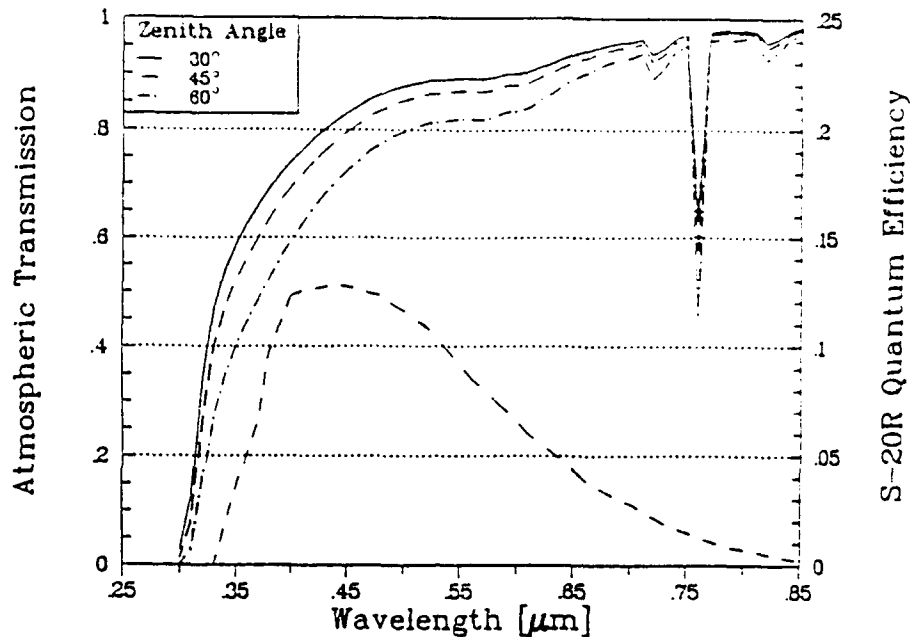
Figure 5. Atmospheric transmission for slant paths to space from AMOS (elevation 3 km) for three zenith angles. The lower dashed curve is the spectral quantum efficiency of the AATS photocathode (from manufacturer's data).

of its diode-array detector and the transmission of the intervening atmosphere are sensibly the same as those of the AATS camera shown in Fig. 5.

The radiometric response of the GEODSS auxiliary camera was determined by the same procedure as that for the AATS camera, making use of the array of 24 known stars in the constellation Cetus shown in Fig. 7 and identified from the SKYMAP listing (Ref 20) in Table 3. Very high uniformity of the dark current of this sensor across its field of view is evident in the exposure of Fig. 7 (as well as in Fig.   ); that is, in contrast to AATS GEODSS exhibits little spatial variability of baseline.   Figure 8 plots the photocurrents-above-background integrated over the image area against the irradiances from each star summed over the full width to half maximum of the (S-20R) camera wavelength response and the (LOWTRAN-calculated) transmission of the 60° zenith angle atmosphere above AMOS. These summations over the spectral sensitivity were performed by first computing a color temperature from the tabulated Blue, Ultraviolet, and Visual magnitudes, or alternatively by using the stellar class as also tabulated (see for example Ref. 21); details are presented in the description immediately below of the AATS calibration. At 6000K star temperature an error as large as ±1000K has only a small effect on the effective calibrating irradiance.

14
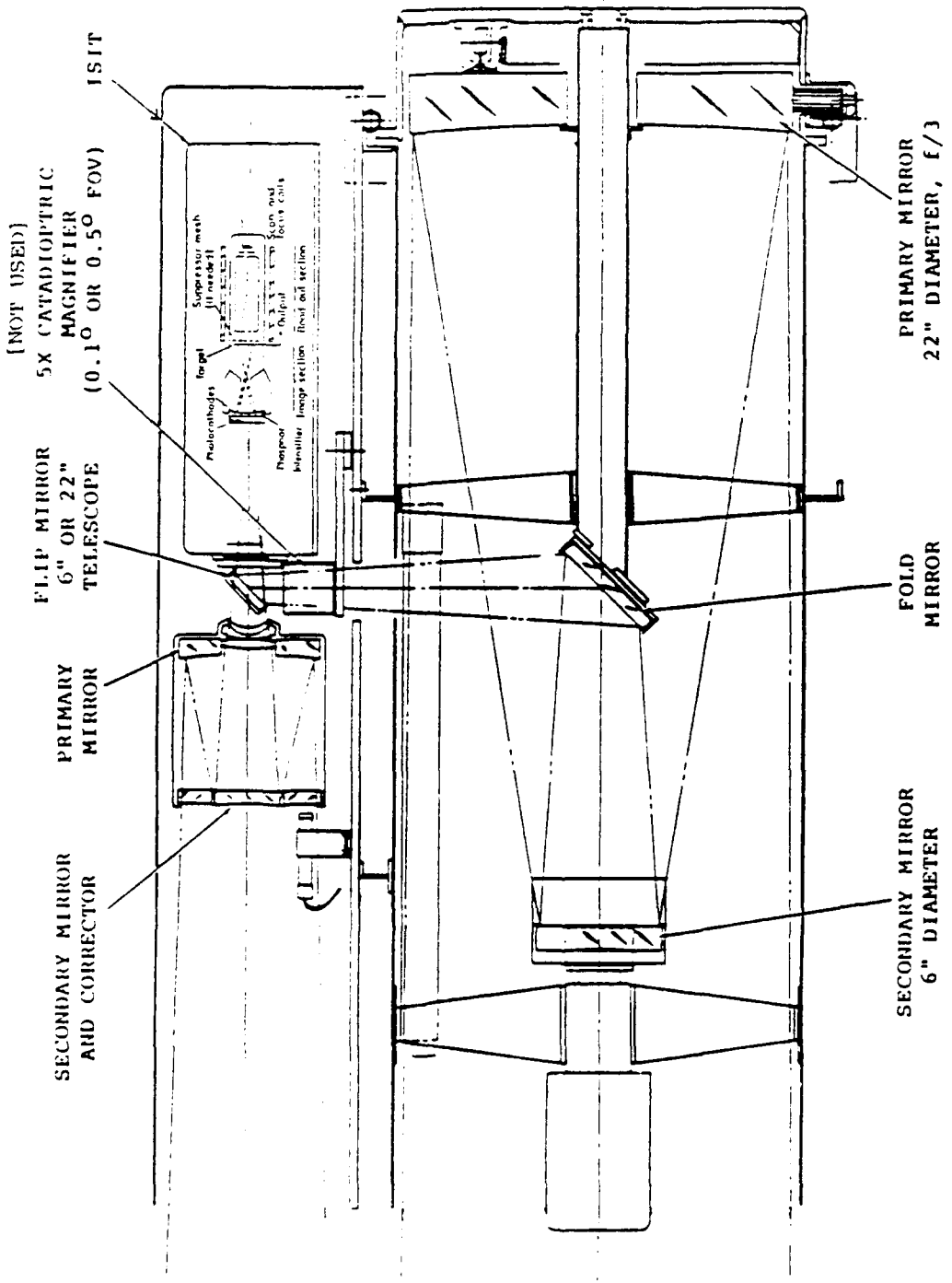
Figure 6. Optical system of the AATS-MOTIF finder telescope. The upper telescope produces the 3° image field. The schematic diagram of the second-generation ISIT photodetector is adapted from manufacturer's data.

15

KEY 8	
PU	Col
0-15	
16-31	
32-47	
48-63	
64-79	
80-95	
96-111	
112-127	
128-143	
144-159	
160-175	
176-191	
192-207	
208-223	
224-239	
240-255	
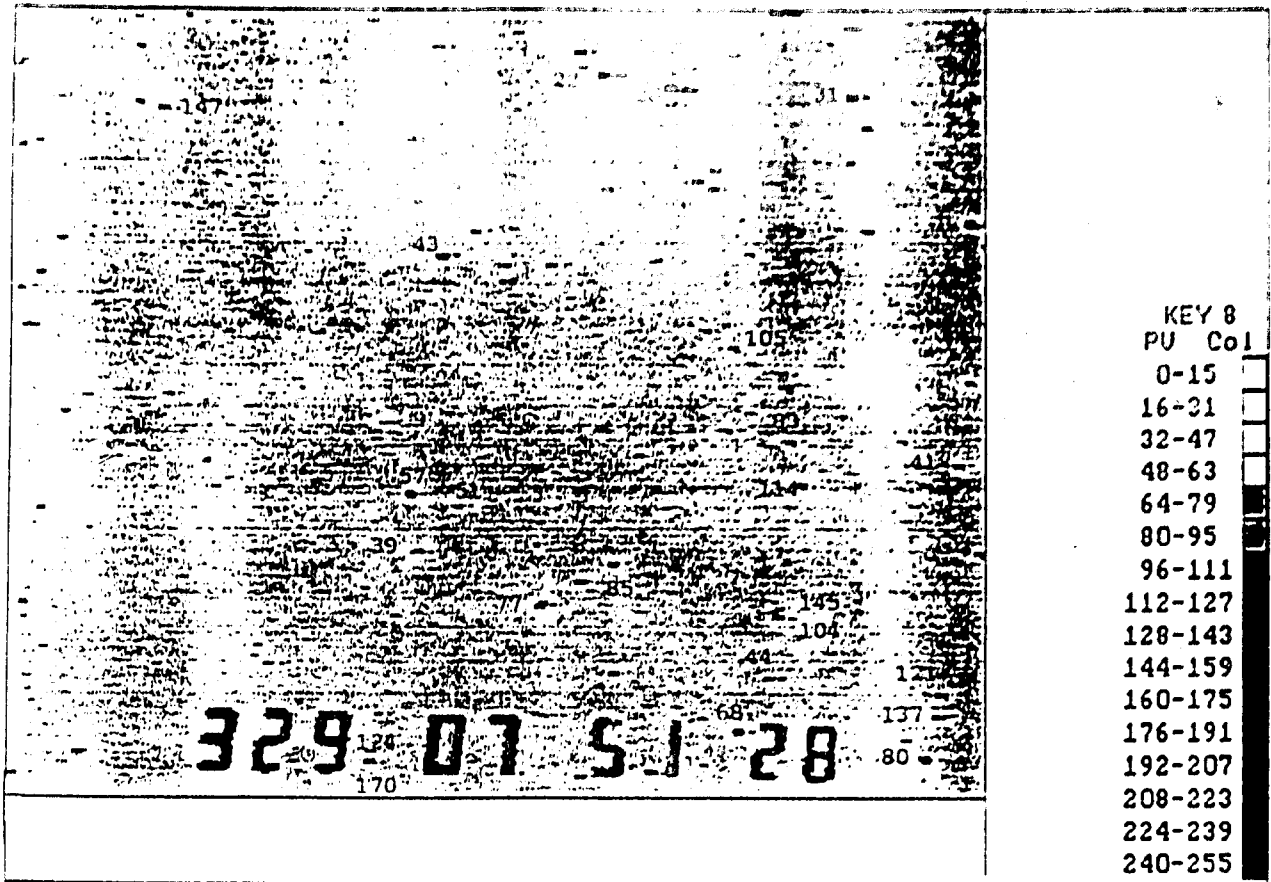
Figure 7.   Stars identified in SKYMAP in the field view of the GEODSS auxiliary camera just before the STS-33 wake burn, average of 128 frames (refer to Table 3).

We applied the response characteristic of Fig. 8 in deriving the sterance of exhaust-interaction luminosity listed in Table 6. Its internal consistency indicates that the radiometric results from GEODSS are considerably more reliable than those from the AATS camera (whose narrow field of view, furthermore, becomes overfilled by the emitting air volumes at about ~½ s after thruster turnon; refer to Fig's. 23-26).

Calibration of the AATS Video Camera: General

The nonuniformity of "dark" current across the image plane of the AMOS-MOTIF camera suggests that the photocurrent output per unit irradiance input is also varying across the field of view of this sensor, which would require a scene angle-dependent correction to its radiometric measurements. We document here our efforts in establishing absolute calibration of AATS against known stars. (The cost of radiometrically calibrating the large-aperture,

16

Table 3. Identification of Stars for Radiometric Calibration of the GEODSS Camera*.

NO.	SKYMAP	X	Y	ALF	DEC	B MAG	U MAG	V MAG	CLASS	T	B - V	U - B
5	220109	3.393	-0.622	5.6993	-12.33753	7.35	7.29	6.39	420 G2 V	6500	0.56	.24
20	280001	1.768	-0.342	6.795	-11.78573	9.356	10.979	7.466	540 M4 III	3100	1.59	1.923
22	290029	1.505	0.022	7.2521	-11.72493	8.77	9.905	7.63	520 K2 III	4100	1.14	1.135
31	240117	2.519	-0.104	6.166	-11.33798	8.43	8.442	8.06	320 F2 V	8400	0.37	0.012
39	320105	0.531	-1.952	8.149	-13.51309	8.256	8.162	8.226	195 89.5	16000	0.33	-0.094
41	230031	3.012	-1.635	5.768	-13.29473	8.746	8.765	8.266	350 F5 V	7600	0.-8	0.019
43	320013	0.733	-0.704	7.9983	-12.42188	8.35	8.37	8.27	380 F8 V	7300	0.53	0.02
44	260103	2.135	-2.530	6.6192	-14.15634	8.326	8.343	8.286	380 F8 V	7300	0.54	0.022
51	310159	0.774	-1.767	7.9604	-13.43608	10.318	11.578	8.578	550 K5 III	3700	1.--	1.66
57	320118	0.556	-1.712	8.1744	-13.38444	9.498	-9.999	8.648	450 G5 III	5000	0.35	-9.999
68	270027	1.986	-2.759	6.7647	-14.37493	9.703	11.038	8.763	520 K2 III	4100	1.14	1.135
77	300090	1.129	-2.194	7.6102	-13.84169	9.704	10.26	8.354	450 G5 III	5000	0.35	0.556
82	220021	3.265	-1.951	5.5164	-13.59267	9.364	9.383	8.384	350 F5 V	7600	0.-8	0.019
83	260024	2.273	-1.533	6.4915	-13.20455	9.364	9.383	8.384	350 F5 V	7600	0.-8	0.019
85	290041	1.464	-2.333	7.2819	-13.58664	9.364	9.383	8.384	350 F5 V	7600	0.-8	0.019
104	260071	2.195	-2.269	6.5628	-13.90646	10.5	12.16	9.06	570 K7 III	3600	1.--	1.66
114	250131	2.318	-1.720	6.4465	-13.38218	9.57	9.589	9.09	350 F5 V	7600	0.-8	0.019
121	230085	2.395	-2.599	5.8725	-14.21407	9.78	10.18	9.13	400 G0 III	6000	0.55	0.4
124	330098	0.327	-2.340	8.3972	-14.46011	9.61	-9.999	9.13	350 F5 V	7600	0.-8	-9.999
129	220114	3.094	-2.001	5.6836	-13.54207	10.356	11.491	9.216	520 K2 III	4100	1.14	1.135
137	230103	2.876	-2.690	5.3899	-14.30081	9.39	10.29	9.24	400 G0 III	6000	0.55	0.4
145	260087	2.168	-2.249	6.3897	-13.388	10.719	12.379	9.279	550 K5 III	3700	1.--	1.66
147	360139	-0.468	-0.042	9.1775	-11.79065	9.936	10.337	9.286	400 G0 III	6000	0.55	0.401
176	330094	0.334	-2.795	8.3902	-14.41665	10.74	11.75	9.96	0		0.98	0.81

* The number in the first column is assigned to identify the star whose SKYMAP listing is in the second column; X and Y represent its angular position in the field of view in our notation; ALF and DEC are right ascension and declination; B, U, and V mag are the standard magnitude classifications, and the two succeeding columns are the stellar classification, primarily from SKYMAP; and T_c is the effective radiating temperature.

automatically gain-controlled camera using standard light sources or photodiodes was judged to be beyond experiment budget.)

The baseline digitized photocurrent with the camera operated in its 0.5°-field mode, averaged over 90 successive video frames, is plotted in contour form in Fig. 9a, and its histograms of occurrence before and after this averaged background was subtracted are in Fig. 9b. (As is shown in Ref 2, this baseline is due to leakage currents rather than the sky background from airglow and astronomical sources.) The dark current distribution in 3°-field mode (used to image an STS-29 exhaust interaction) appears similar, with again a maximum toward the upper left of the frame. Figure 10 is a quantitative comparison of the two baselines in diagonal scans from upper left to lower right (the spikes in the wider-field trace are real signal from stars in the field of view), which shows them to be sensibly the same--at least in this cut across the video frame. Two separate optical systems image the sky onto the photocathode (refer to Fig. 6), and the photocurrent distribution is not symmetric about their
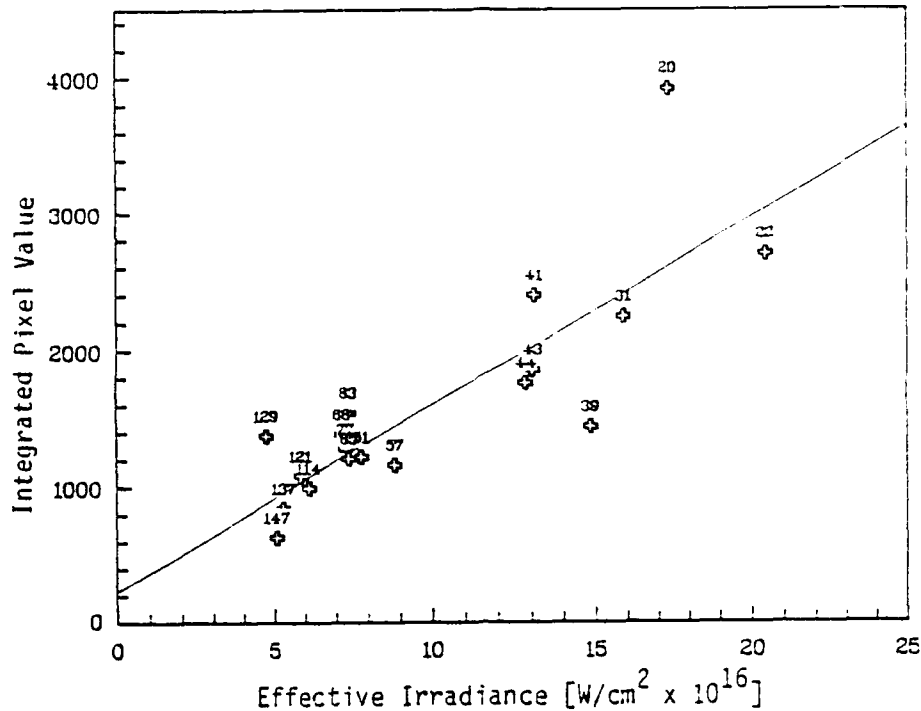
Figure 8.   Stellar irradiance weighted with relative spectral response of the GEODSS photocathode plus intervening atmosphere, for 18 of the 24 stars in Table 3. Those stars that are omitted have either saturated or too-weak or spatially-overlapping signals. The line through the points is a standard least-squares best fit with all points given equal statistical weight. The data represent an average over 90 video frames, with the local scene baseline photocurrents in 20 x 30 pixels subtracted from the photocurrents produced by each star in 10 x 20 pixels.

optic axes--and furthermore this baseline is any case not due to a spatially-variable response to the scene; in consequence we may conclude that what may be termed the "vignetting" of the ISIT video receiver tube itself is responsible for the variability over the AATS-MOTIF camera's field(s) of view.

Calibration of the AATS Video Camera: STS-29

We identified from star charts 11 stars with visual magnitude (V in Table 4) less than 9.3 in the 3°-field video frames recorded immediately before, during, and immediately after-- i.e., at the same electronic gain as--the STS-29 engine firing (historically, the first in the experiment series). The SKYMAP listing included B(lue)-magnitude for 7 of these stars, to 6 of which it also assigned a spectral class. The photometric data on these irradiance-calibration sources are in Table 4, and their average and extreme values of digitized photocurrents integrated over "image" area (henceforth occasionally identified as PV) are listed in Table 5.

18
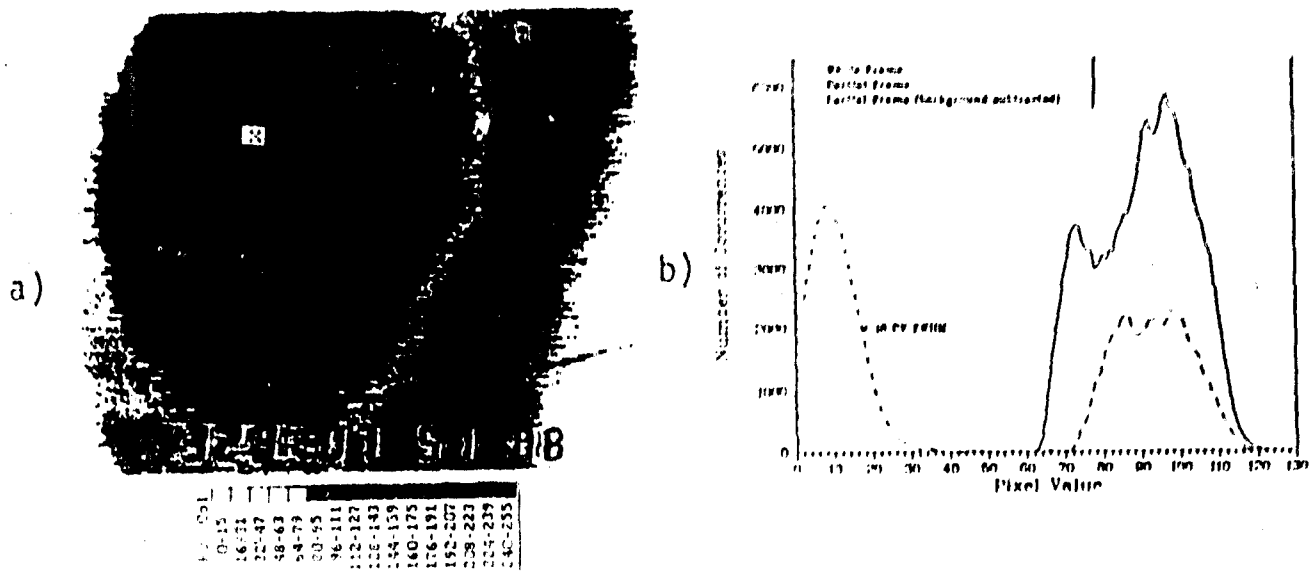
Figure 9. a) Baseline ("dark") photocurrents of the AATS 0.5°-field camera, averaged over 90 video frames. This current varies over at least a factor 2 at this particular (high) automatic gain setting, as is shown by the histogram in b). The left-hand distribution in b) represents the difference between the average and one randomly-selected frame, plus 10 digitized photocurrent units. The faint streak at lower right is an unidentified (magnitude > 9) star. The position of the center of the fields in Figure 12 is indicated by the white X.
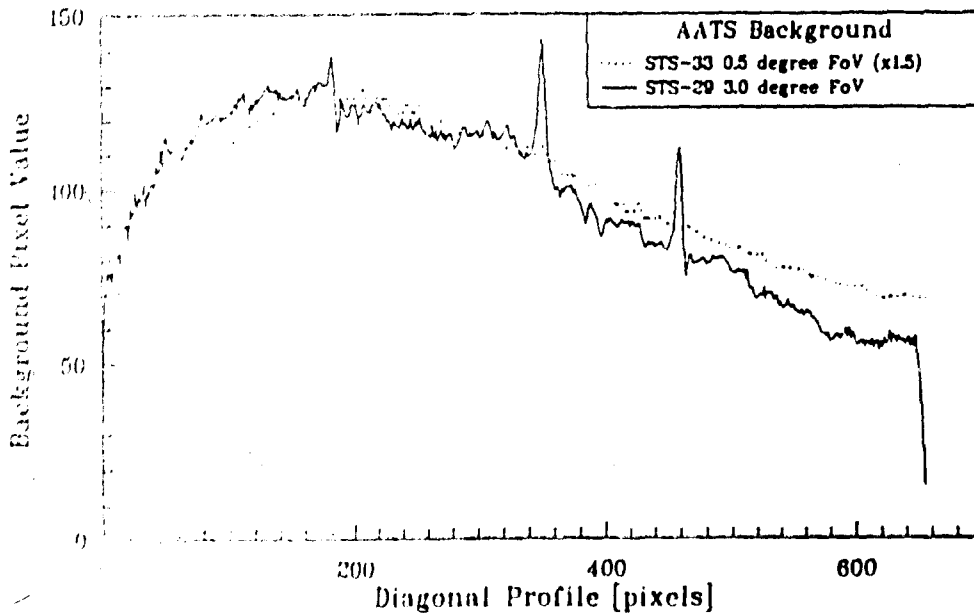
Figure 10. Baseline (background, or "dark") photocurrent of the AATS-MOTIF camera in diagonal scans from upper left to lower right, normalized at pixel 180. The data for the 0.5" field are from Fig. 9, and those for the 3°-field mode from a single video frame (in which the spikes are due to stars).

19

Table 4.   Stellar Irradiance for the STS-29 Measurements

| Star | Position in field | | | Magnitude | | Blackbody | Stellar |
No.	x pxl	y pxl	B	U	V	T_c	Class
27	70	159	7.12	-9.99*	7.12	15400	F2 IV
29	116	125	8.45	-9.99	7.27	4400	A0 V
65	248	232	8.57	-9.99	8.2	8300	K0 IV
66	65	331	9.05	-9.99	8.2	5000	G5 IV
149	130	138	9.704	-9.99	8.85	5000	G5 IV
168	28	428	9.357	-9.99	8.99	9000	F0 V
175	125	268	9.844	-9.99	9.0	5400	K0 - est'd
122	09	323	-9.99	-9.99	8.7	6000	assigned
143	60	254	-9.99	-9.99	8.8	6000	assigned
205	324	312	-9.99	-9.99	9.1	6000	assigned
250	390	142	-9.99	-9.99	9.3	6000	assigned

*Identifies missing data in the SKYMAP listing.

Table 5.   Statistics Summary for STS-29 Stars

Star No.	Frames Averaged	Average Integral of PV	SD of PV*	Minimum PV	Maximum PV
65	60	6593	1099	4186	9439
27	26	7279	1075	5727	9847
29	43	4940	1177	2561	7980
66	25	4680	826	2892	6680
149	49	1695	700	0	3252
168	10	3035	546	2081	3967
175	46	1012	629	0	2602
122	4	2251	174	2107	2495
143	23	3045	771	1299	4159
205	60	2091	587	512	3471
250	6C	2469	839	476	4617

*Standard deviation of the pixel photocurrent values.

No star with visual magnitude less than 10 passed through the projection of the PRCS exhaust gas interaction volume.

We summed the photocurrents in a rectangular "box" of 18 x 24 (horizontally) picture elements centered on each of these identified and geometrically-isolated stars, and determined the local baseline by similarly integrating a 31 x 43-pixel region encompassing this smaller image area. This local background (in the absence of other, interfering stars) is then the

20

difference between the two photocurrent integrals divided by the ratio of areas. This method gave a near-zero net irradiance when applied to regions of image in which no stars were detectable (the apparent threshold visual magnitude was 10).

As the AATS telescope is tracking on Shuttle Orbiter the astronomical scene moves rapidly across its field of view, so that only 3 of the 11 stars applied remained in this field during the full 62 video frames considered. The number of frames averaged for each star, and the frame-to-frame variability in spatially-integrated photocurrents, are indicated in Table 5 and Fig. 11. These calibrating data can be described as generally very noisy; plots of PV's against time (such as Fig. 11), or against one another in individual frames (not explicitly shown), or even against radial distance from the region of highest baseline current (Fig. 12) show largely-inconsistent trends. This last display of the data, in particular, fails to resolve a change in current output above dark baseline with the level of this baseline. Such a behavior would be exhibited if the background image patterns (such as are illustrated in Fig. 9) are produced by a systematic change in electron multiplier gain or initial photoelectron collection efficiency across the image plane, which is expected on physical grounds and would result in the aforementioned deleterious spatially-variable response of the sensor system rather than merely in the in principle-subtractable "bullseye" pattern of dark-current density. (A reduction and analysis of the photocurrents produced by brighter stars as they move through the camera field might quantify any such response variation.)

Another factor that may be degrading radiometric fidelity is the undershoot of photocurrent in the scan direction characteristic of electronically intensified video receivers, which is shown in Fig. 13d. (The effect is also obvious in Ref 2's AATS images of the sunlit Shuttle Orbiter body.) This undershoot--actually an underdamped ringing, as when the signal is particularly large it is followed by a smaller overshoot--is presumably due to some charge-depletion effect in the photoemissive material; if so, the main smeared-image peaks would be distorted also. The presence of sub-baseline photocurrents reduces the apparent total from stars; on the other hand, if this net loss of output current is proportional to the irradiance from each such point source (see Fig. 13d), which is a reasonable first approximation, it would not substantially affect the relative total area-integrated stellar signals. That is, a "linear" undershoot (and distortion of the main star peak) would not alter the sterance calibration per se. Nonetheless the additional error introduced by this "adjacency effect" in radiometry of extended sources such as the exhaust interaction volume cannot be readily assessed, and could be as high as 20-25%.

We took the absolute spectral irradiances outside the atmosphere of V and B zero-magnitude stars to be 3.7 and 6.6 x 10^{-12} w/cm^2 μm at 5500Å and 4400Å respectively (see Ref 21), and approximated the spectral distribution of each of the calibrating stars listed in

21
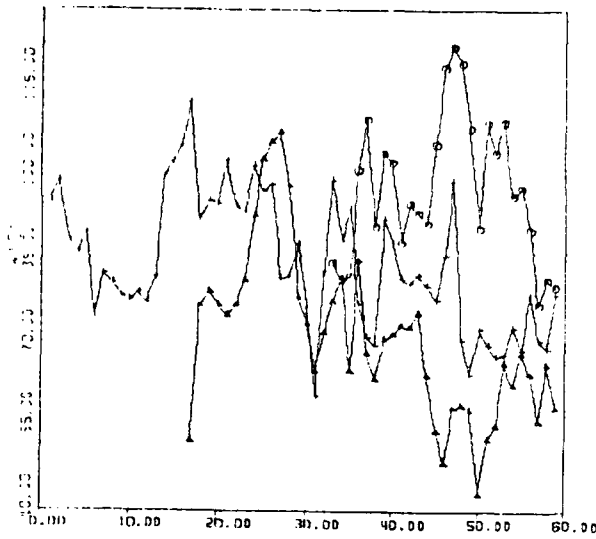
Figure 11. Individual-frame area integrals of the digitized photocurrents from 9 of the 11 calibrating stars identified in Table 4. (Note that the ordinate scale does not start at zero.) The abscissa represents sequential video frames. The (poor) correlation of the summed photocurrents indicates the precision of individual such measurements.
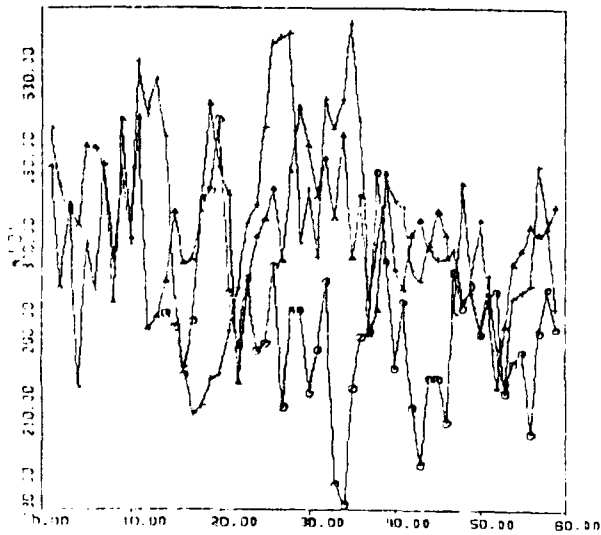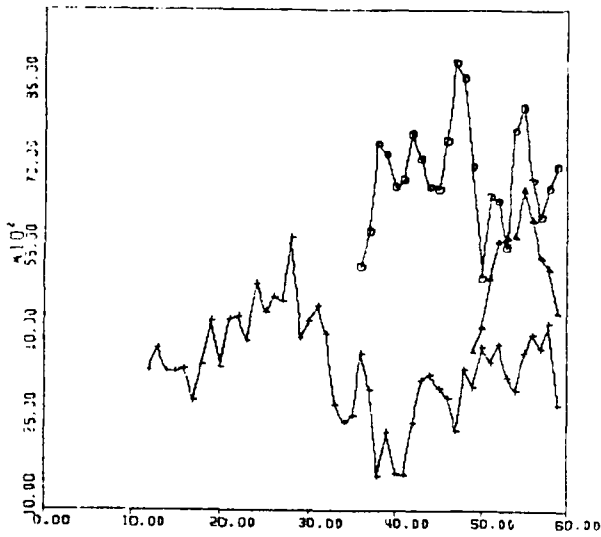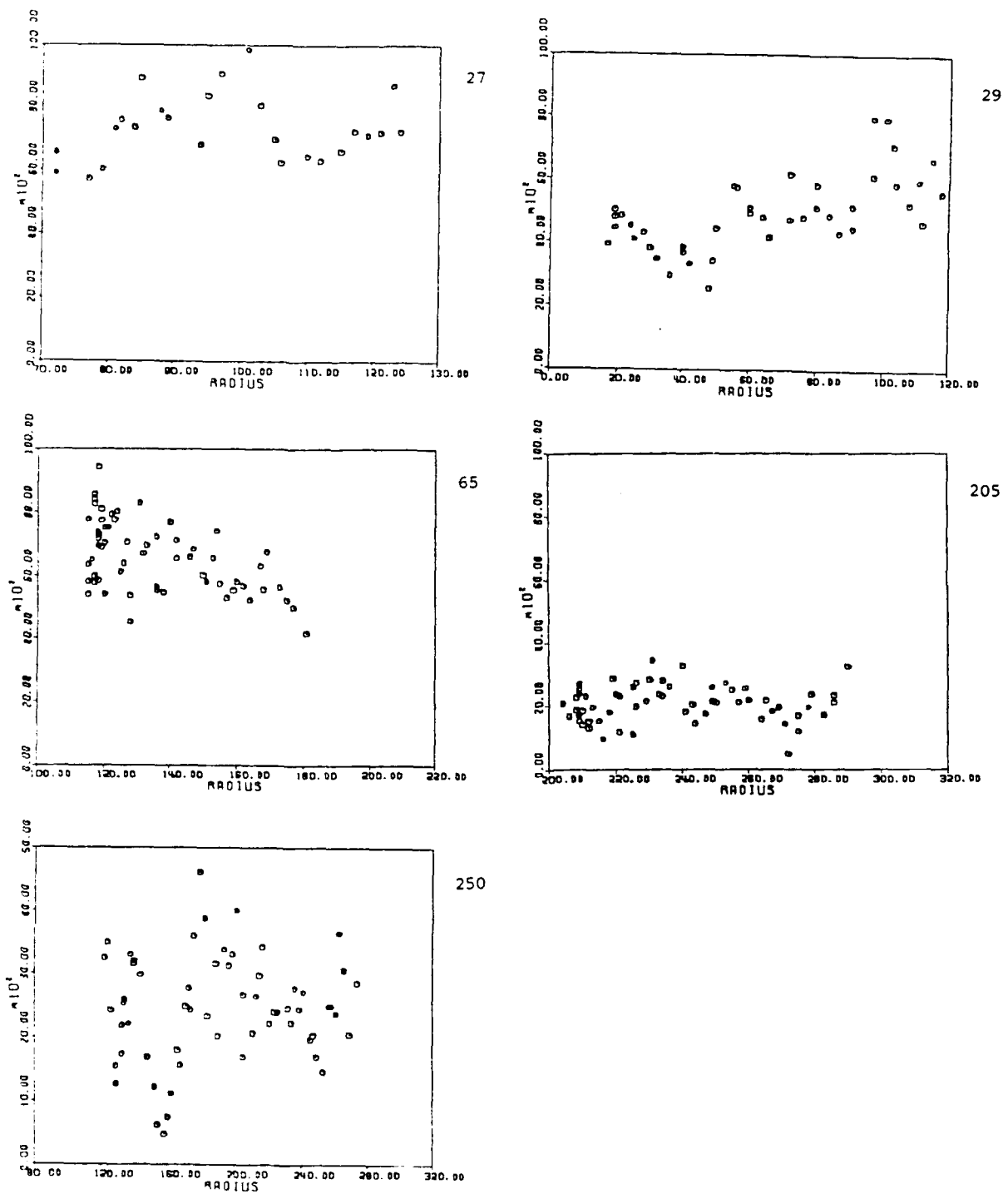
Figure 12. Individual area integrals of the digitized photocurrents from 5 of the 11 stars in Table 4, as a function of image-plane distance in pixels ("RADIUS" on the abscissa) from the point of highest dark photocurrent in Fig. 9a.

23

Table 4 as a blackbody normalized to its V(isual) magnitude at 5500Å. The color temperature T_χ for each stellar class (or, in one case, the B - V and U - B magnitude difference) was taken from standard astrophysical references for seven of the identified stars; we assigned T_χ = 6000K to the four calibrating stars for which this information was not available (as noted, an error in T_χ as high as 1000K makes little difference in the calculated in-band irradiance). We then summed in 100-Å intervals the product of

(spectral irradiance, in units of power flux per unit area) ·

(nominal S-20R spectral response, in units current output per watt input [Fig. 6]) ·

(atmosphere transmission [as in Fig. 5])

to derive the absolute stellar irradiances applied in Fig. 14. (The transmission parameters adopted for the LOWTRAN calculation were 1962 U. S. Standard Atmosphere with no aerosols, and sight path at 19° elevation angle to space from 3 km altitude [as for the STS-29 data].)

The radiometric calibration of the GEODSS camera briefly outlined above and whose results are summarized in Fig. 8 was performed following the same procedure. The photocurrents in boxes of 12 (vertically) by 18 picture elements isolated each of the stars inside 20 by 30-pixel boxes, the photocurrents from which were similarly summed to determine star irradiances plus instrument baseline. As alluded to previously, a comparison of the calibration data in Fig. 14 with those of Fig. 8 (in which the abscissa refers to relative rather than nominal absolute wavelength response of the camera's photocathode) indicates that the radiometry results from the AATS camera are likely to be substantially less reliable than those from GEODSS. We ascribe most of the internal inconsistency of the AATS calibration to the erratic baseline--and hence suspected variable electronic gain--over its image field; some of the lack of direct proportionality may be due to saturation of the spread-images of seventh-magnitude stars 27 and 29. (These PV's become less weighted when the calibration line is forced to go through the origin.)

Calibration of the AATS Video Camera: STS-33

This later experiment made use of the 0.5°-field AATS-MOTIF telescope, which when tracked on Orbiter produces streaked star images such as are shown in Fig. 13b. The paucity of stars in the small field of view, along with residual error in the el/az of the camera's optic axis and--in particular--its azimuthal orientation (i.e., the rotation of the astronomical scene) led to uncertainty in identifying stars using AATS images alone. (The relative positions of several astronomical objects are usually needed to identify stars with magnitudes > ~8.) We
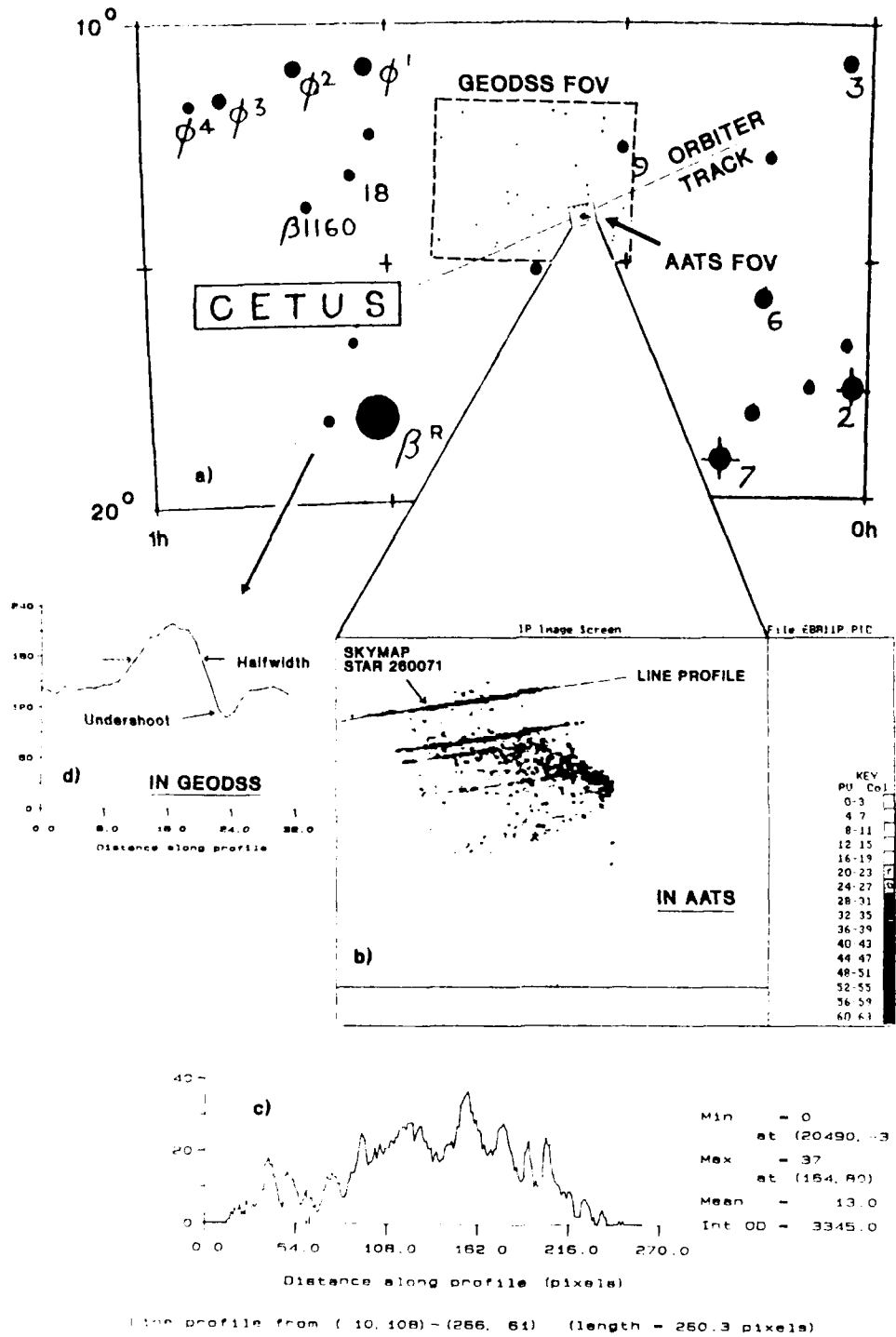
Figure 13. a) GEODSS and AATS-MOTIF 0.5° fields of view in the constellation Cetus at the time of the STS-33 engine firings. b) Wake firing seen by the AATS camera, with stars appearing to move toward the left. c) Line profile along the symmetry axis of SKYMAP Star 260071 (Number 104 in Table 3 and Fig. 8). d) Illustration of typical photocurrent undershoot in the intensified-video system.

25
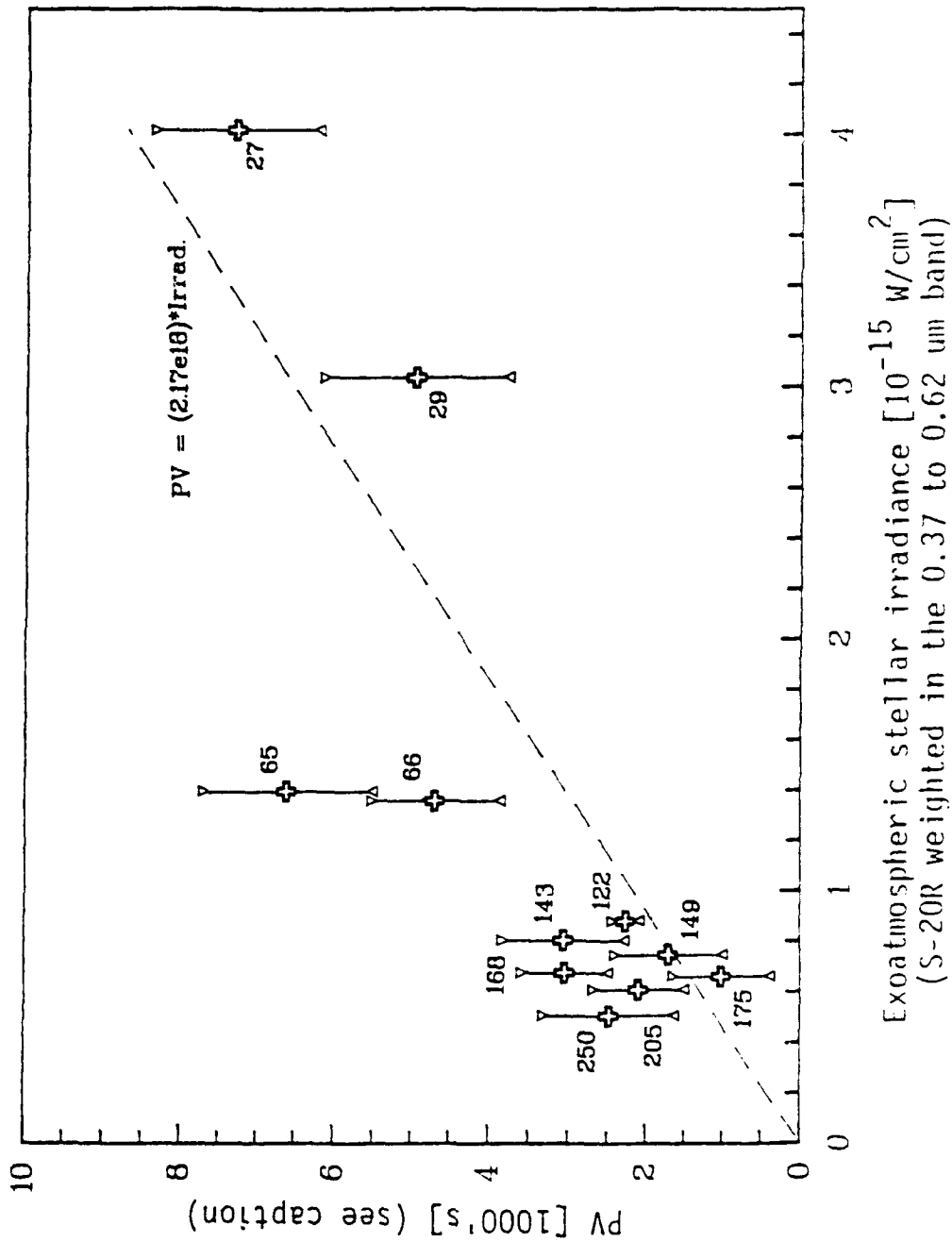
Figure 14. Radiometric calibration of the AMOS-MOTIF 3°-field AATS camera for the STS-29 thrusters burn. The ordinate is the averaged digitized photocurrent above background, and the abscissa the transmitted irradiance within the sensor passband both derived as described in the text. The error bars on the ordinate are 1σ from the original video images (see Table 5 and Fig. 11). The dashed line is the weighted least-squares best-fit to the data forced to go through the origin.

therefore located the rapidly-translating narrow field approximately within the wider essentially-fixed field of the GEODSS camera (refer to Fig. 13a), whose larger-area objective lens furthermore produced many more star "images" above threshold.

Figure 13d is a plot of the (noisy) individual photocurrents along the symmetry axis of SKYMAP star 260071 identified by this procedure, and Fig. 15 is a similar plot of the photocurrents from brighter star 200022 (which is just out of the field in Fig. 7). The length
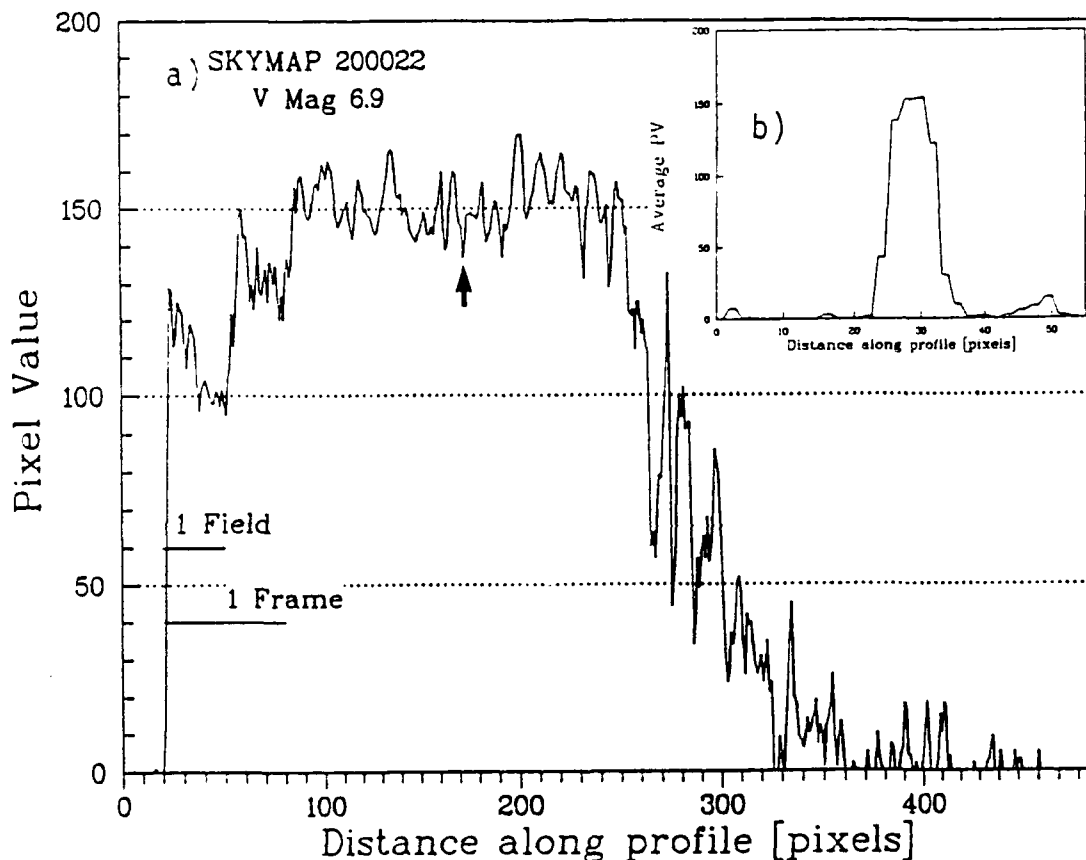
Figure 15. Photocurrent trace along the symmetry axis of the image of SKYMAP star 200022 in an AMOS-MOTIF 0.5°-field frame tracked on Shuttle Orbiter. A perpendicular trace b) across the streak at the point indicated by the arrow is shown at upper right.

of the apparent image of the fast-moving (~50 pixels/AATS frame) stars can be seen to be 3 to 4 times greater than the calculated projected length of their irradiance streaks in 1/30-s field-interlaced frames. We interpret this anomalous behavior as due to persistence of the phosphor(s) in the electronic image intensifier of the AATS finder telescope (diagrammed at upper sight of Fig. 6). We used the complete spatial distribution of photocurrent in

27

determining the area integrals PV analogous to that for slower-moving irradiance standards (i.e., stars in the 3°-field AATS, which move only about 10 pixels per frame--comparable with the image spread from the camera optics and focal plane detector array). Our adoption of this procedure is based on the argument that, in first approximation at least, the time-integrated output photocurrent from moving light sources should be the same as that from essentially-"stationary" radiating sources--such as the tracked spacecraft body and the exhaust-interaction volumes. (As Fig's. 13 and 15 indicate, the area under the photocurrent curve from the length of star track that would correspond to a single video frame is roughly 1/3 the total apparent area.)

VIDEO IMAGES OF THE PRCS EXHAUST INTERACTION VOLUMES

Introduction

We review here the visible radiance distributions that resulted from reactions with the atmosphere of thruster combustion-product gases direcɪ ⁴ toward ram, perpendicular to the orbital track, and the vehicle's wake, as measured by the AMOS cameras described in the previous Section. Our focus is on the unique experiments performed in connection with shuttle mission STS-33, for which Geophysics Directorate specified sequences of 3 s PRCS engines-on separated by 5 s engines-off, including two individual perpendicular firings separated by 180° in roughly up and down directions. The single burn of three engines on STS-29, imaged with the AATS-MOTIF camera in 3°-field mode, served in large part as a training set for analysis of the much more extensive, higher spatial resolution STS-33 image data.

STS-29, Orbit 65 -- General

At the time of the firing at 15:34:38 UT on 17 March 1989 Shuttle Orbiter was at 333 km altitude and at 860 m range, 19° elevation, and 282° azimuth from AMOS. The sun was about 3° below the eastern horizon as seen from the vehicle's altitude, and the angle between its 33° N of E trajectory direction and the vector from the camera station was 50°.

The PRCS engines operated (identified in Fig. 1) and their timing were

UT	F3U	L3D and R3D
15:34:38.201	off	not stated
15:34:38.241	not stated	on
15:34:38.281	on	on
15:34:38.321	on	on
15:34:38.361	on	not stated
15:34:38.401	not stated	off
15:34:38.441	off	off

"Not stated" refers to gaps in the listing provided by NASA of on-off status. It appears, then, that the burn times of the thruster engines lay between 80 and 200 ms, with a start-stop lag of 40 ms--about one video frame--between the first-listed and the two other thrusters.

A linear interpolation in the NASA tabulation of the orientation of Orbiter (sampling

was each 30 s) gave the angles

Pitch   325° (nose 35° below the local horizontal)

Roll   182° (bay directed toward the lower hemisphere)

Yaw   -0° (nose almost directly to ram, long (X) axis in the vertical plane
         through the trajectory).

The NASA listing accompanying Fig. 1 shows that the two rear "D" engines fire at 102° pitch
angles to Orbiter's forward (X) direction--that is 12° beyond normal to its long axis--, and in
opposition at ± 20° from its vertical in the Y direction. In consequence the exhaust gases
from the two rear engines were actually directed upward 67° in pitch (back) from the ram
direction, while the axis of the combustion products from the directly Z-direction-pointed
forward unit F3U is 35° rearward of the vehicle's nadir. That is, the near-simultaneous firing
of three PRCS engines is not clearly defined as ram or wake or perpendicular as in the
controlled STS-33 experiment; the firing is if anything "perpendicular", with symmetric (Y)
components both toward and away from AMOS.

The first 10 video fields (to provide enhanced time resolution) followed by 46 video
frames of the interaction volume in its projection to AMOS, with the 90-frame-average pre-
burn local baseline subtracted, are shown in isophote form in Fig. 16. The first 31 frames
(62 interlaced fields) are repeated with a different spacing and coding of contours in Fig. 17.
These images are reversed in both the up-down and left-right directions; thus ram is closely
horizontally to the left. (As mentioned above, no correction for camera vignetting has been
applied, nor has any attempt to correct the video undershoots been made.)

Note that all the thruster engines turn off after about 8 frames (< ¼ s), at which time a
second pulse or wave of radiation can be seen in Fig. 17 to extend down and to the left (that
is, near the exhaust direction of the two "D" thrusters); we return to this important
phenomenon momentarily. Since the AATS camera is tracked on the hard body, such
photographs would show "drag" if the directed velocity of the radiating gas differs from the
orbital velocity. The spatial resolution at the 3°-field image scale and 860-km slant range is
sufficient to resolve gross structure in the exhaust-interaction volumes, which in view of the
compound engines firing would be expected to extend both above and below the track of
Shuttle Orbiter; in practice luminosity in the backward hemisphere is below camera threshold.

As the geometry of this glow is irregular and unsymmetric it does not lend itself to
characterization by simple numerical descriptors. In view of the availability of higher-
resolution spatial data from the STS-33 experiment (analyzed later in this Section), we have
made no effort to define "dimensions", other than to measure the outward velocities of the two
distinct luminous areas. These are shown in Fig. 20 and discussed in the next subsection. It
should be stressed that the observable in these video data is column rates of emission of

30
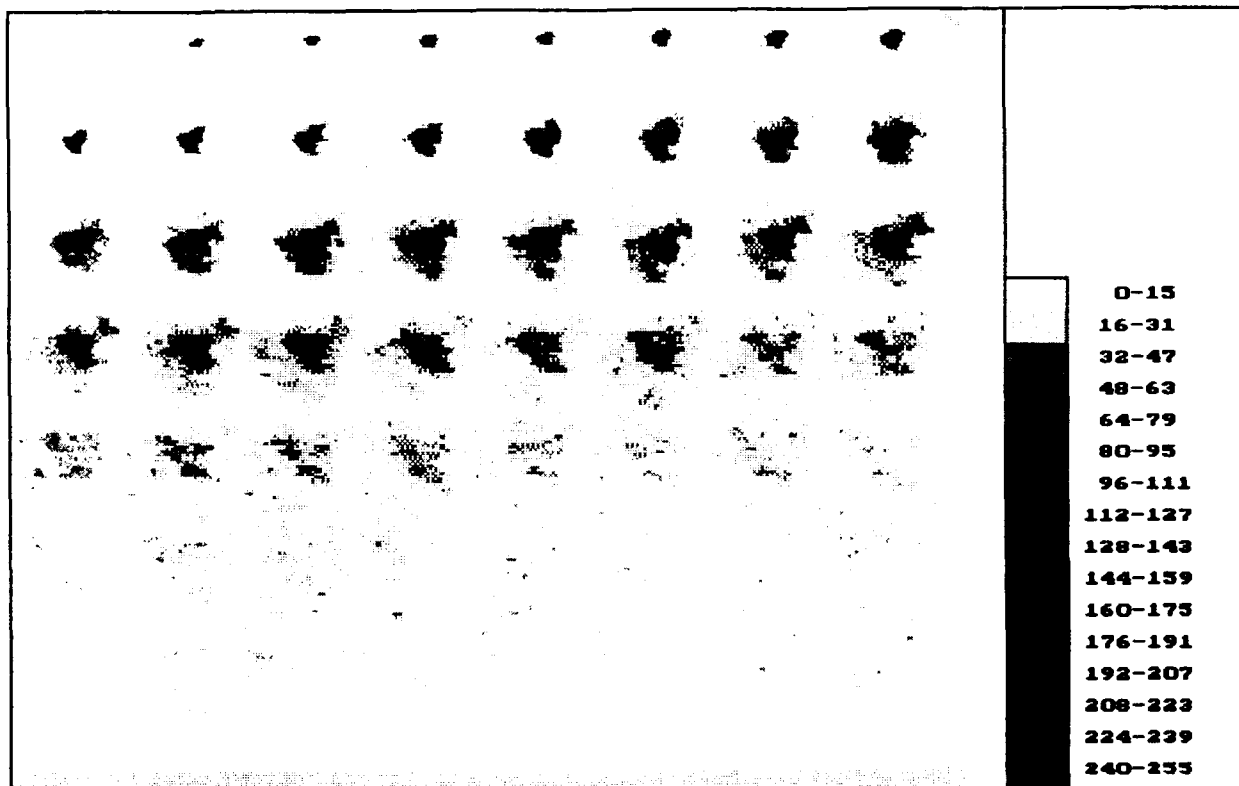
Figure 16. Radiance distribution in the 60 x 60-pixel image area occupied by the STS-29 engine firings. The average local photocurrent baseline in the proceeding 128 video frames has been subtracted. Image scale is 4½ km horizontally normal to the direction of view. The first 10 images are 1/60-s fields, and the remaining are 1/30-s frames. (See also Figure 17.)

photons in the S-20R spectral interval (Fig. 5), rather than column-concentrations of exhaust species--or for that matter, of any particular reaction product.

The radiometry that we performed on the image processing system-produced montage of Fig. 16 is summarized in Fig's. 18-20. Figure 18, a series of horizontal traces through the apparently-brightest regions of these video frames averaged over 5 adjoining scan lines, illustrates quantitatively the growth and location relative to Orbiter of the two emitting volumes in a direction about parallel to the orbital path. As is expected from the two-dimensional patterns, this 1-D scan resolves two maxima in several frames after the thruster engines turn off and the second pulse develops (and soon becomes dominant). Figure 19 plots the maximum values of these radiances in the projection to AMOS, extracted automatically from the traces of Fig. 18 (that is, without manual smoothing/averaging), and the total sterances of the interaction volumes. The absolute surface radiances assigned in Fig's. 18 and
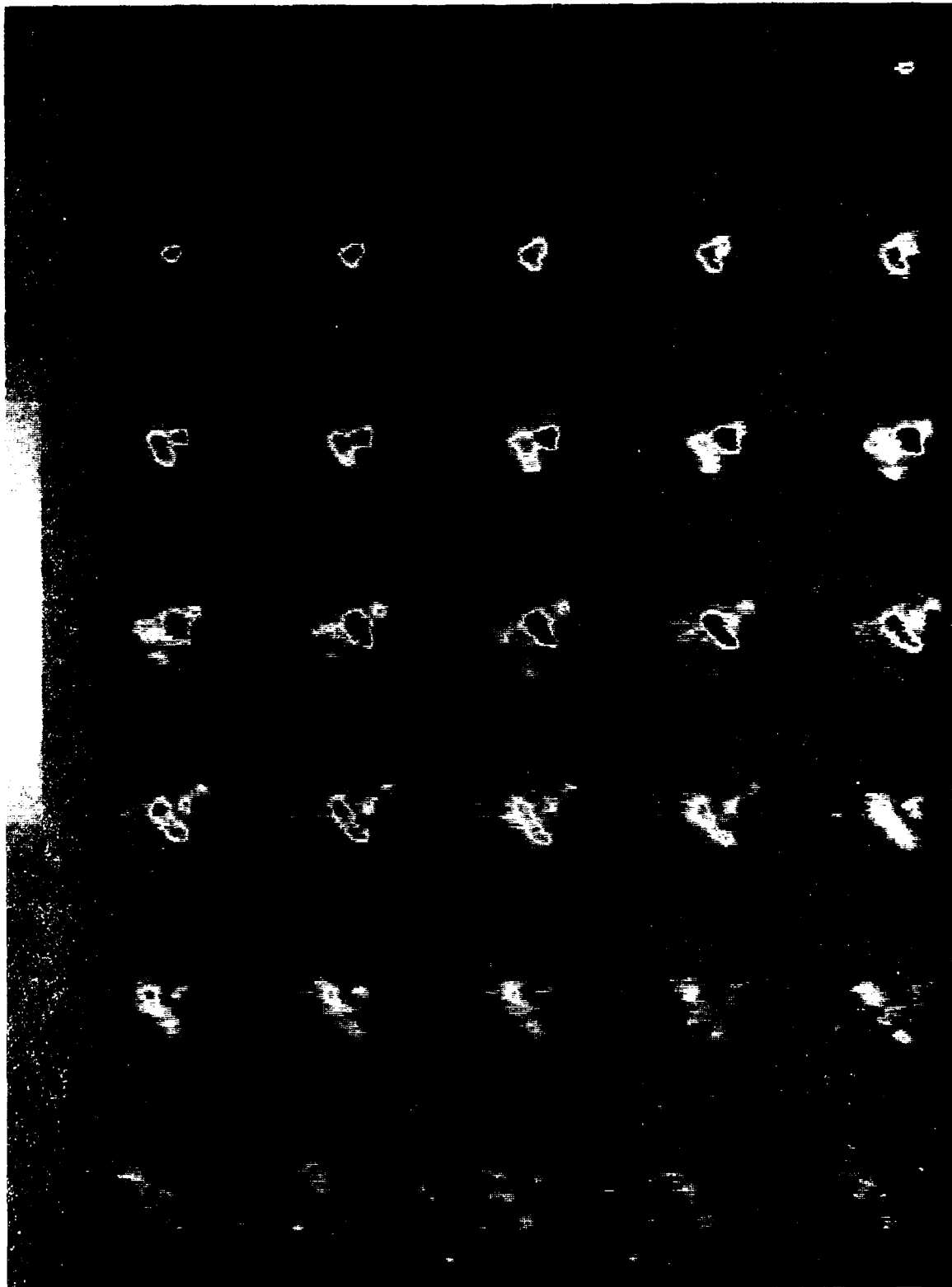
Figure 17. Radiance distributions of the STS-29 engine firings (frames), with a contour interval designed to show the afterpulse that develops ~¼ s into the event (Ref 22). (See also Figure 16.)
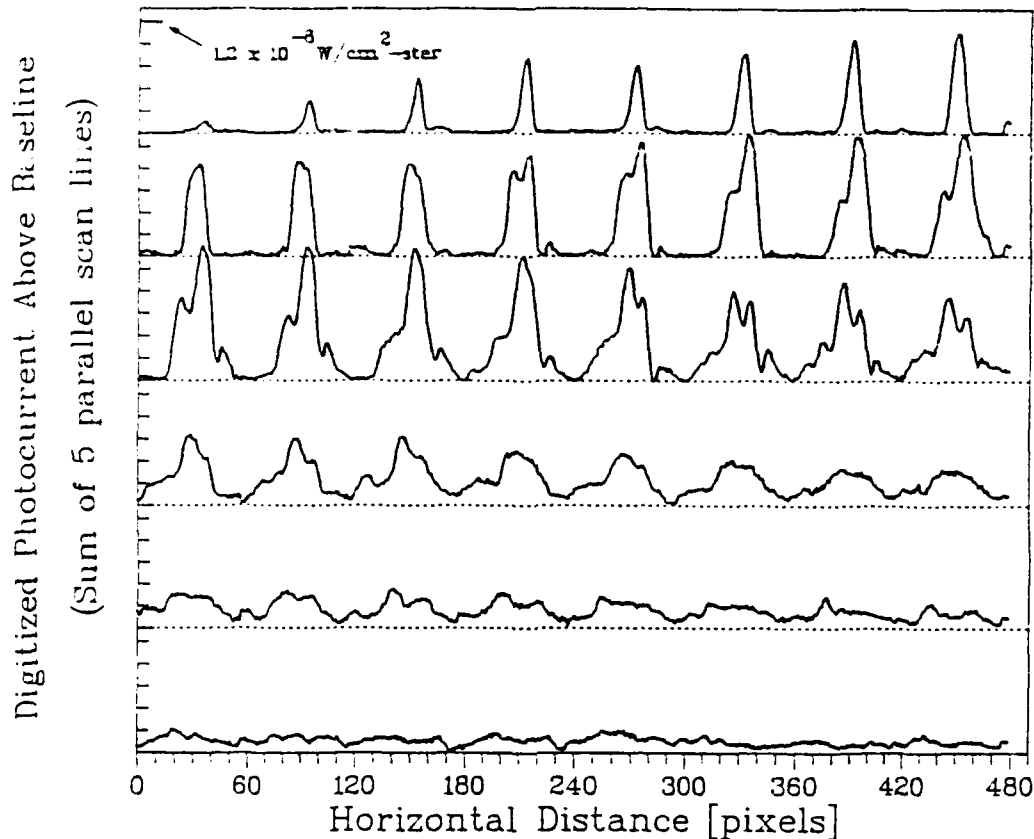
Figure 18.   Photocurrents in horizontal scans through the area of maximum brightness in Figure 17. The numerical values are the sum of digitized output currents from pixels along 5 parallel lines (375 m at Orbiter's range). The calibrating value shown, derived by the procedure described in the text, refers to radiance outside the atmosphere within the full S-20R spectral sensitivity range in the projection of the optically-thin glow to AMOS.

19 are an estimate derived from the total irradiances applied in determining the sterances in Fig. 16 using the apparent "halfwidths" of the radiance patterns; it is thus also referenced to the stellar irradiances along the best-fit line through the origin in Fig. 14.

As in all such standardizations against spectrally-continuous light sources, a relatively flat wavelength distribution over the 3000 to 9000Å response of the video camera is implicitly assumed. A spectral distribution such as in Fig. 56 with -40% less photons would produce the same signal. (The data as presented are corrected for atmospheric transmission, that is, the radiances and sterances stated in Fig's. 18 and 19 and later in this section would be those projected to an observer outside the atmosphere at the same depression and azimuth angles from the luminous volume as AMOS.) In view of the potential errors 1) in the absolute irradiance calibration (refer to Fig. 14), 2) in converting to radiances by estimating the effective solid angle from which the irradiance signal arises, and 3) introduced by differences

33
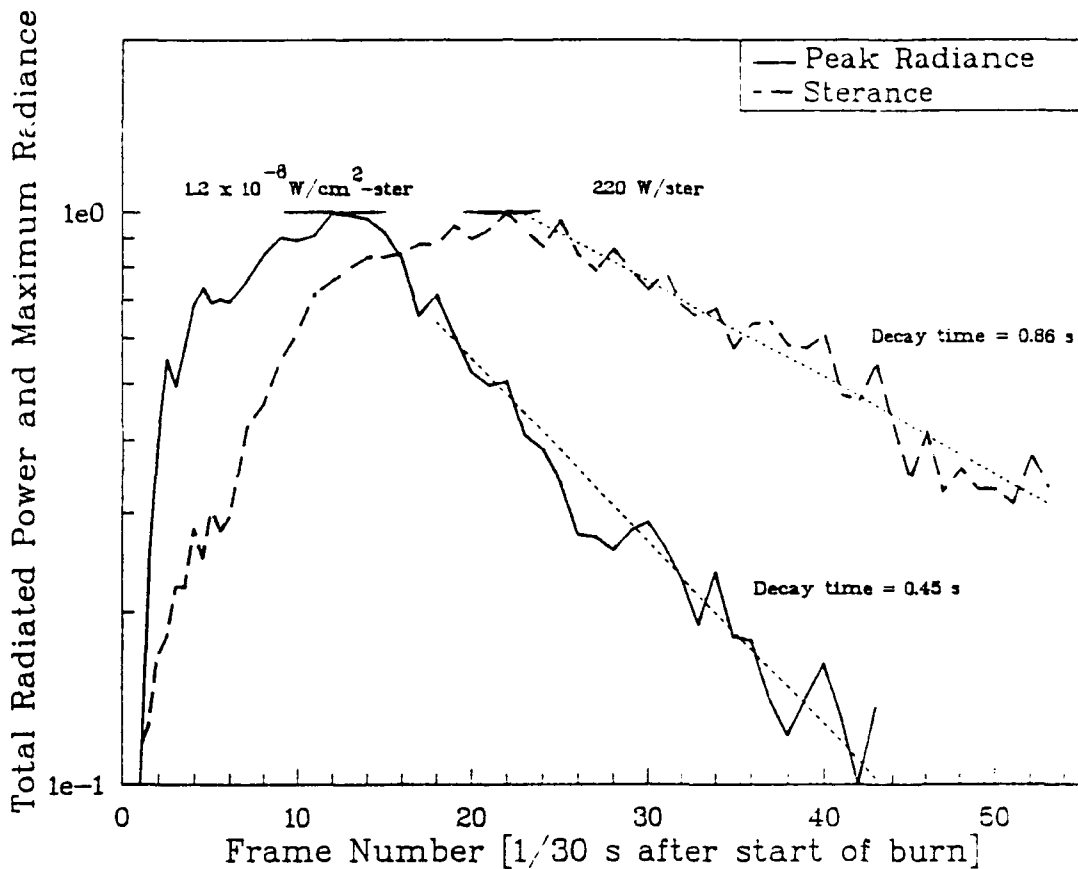
Figure 19.   Maximum radiance in the projection to AMOS and total sterance of the STS-29 exhaust-interaction luminosity outside the atmosphere.

between the (blackbody) emission spectrum of stars and the exhaust-interaction volumes (refer to Section 4), the systematic error in absolute scene radiances could be as much as ± a factor 3. This uncertainty will be reduced when the spectra of the luminosity during the firings proper and associated with the afterpulse are better understood; the two are expected to differ, as the light-producing reaction processes would not necessarily be the same. (Since the STS-29 radiating region occupies only a small fraction of the AATS image field, further error due to focal plane vignetting would be small.)

The sterances in Fig. 19 are the calibrated total exoatmospheric irradiances over the camera's full spectral-sensitivity--a quantity proportional to its photocurrents summed over image area (PV)--multiplied by (860 km range from STS-29 to AMOS)^2. Both this quantity and the surface radiance distributions in Fig's. 16-18 provide a reference for the column intensities of those infrared emissions that would be excited by the same reaction processes that

produce this visible signal, when these processes become identified. (The primary example is $H_2O + O \rightarrow OH^+$, to whose $\Delta v \geq 4$ transitions the AMOS-AATS camera is sensitive (see later Fig. 54) and whose much stronger $\Delta v \leq 3$ rovibrational bands lie in the short-wavelength infrared.)

The visible emission pattern remains above camera threshold almost 10 times longer than the maximum duration of the STS-29 PRCS engine firings. A "break" near ¼ s in the total sterance and maximum radiance in Fig. 20 can be readily identified with a decrease from the period when the thruster engines are operating followed by an increase due to the second outward-going light pulse described immediately below. While the logarithmic rates of rise of sterance during the initial phases of both pulses appear to be sensibly the same, the maximum photon yield rate from the afterpulse is more than twice that during the engine firing. Both the peak radiance and the sterance--from the after pulse-- later decay exponentially, the latter with
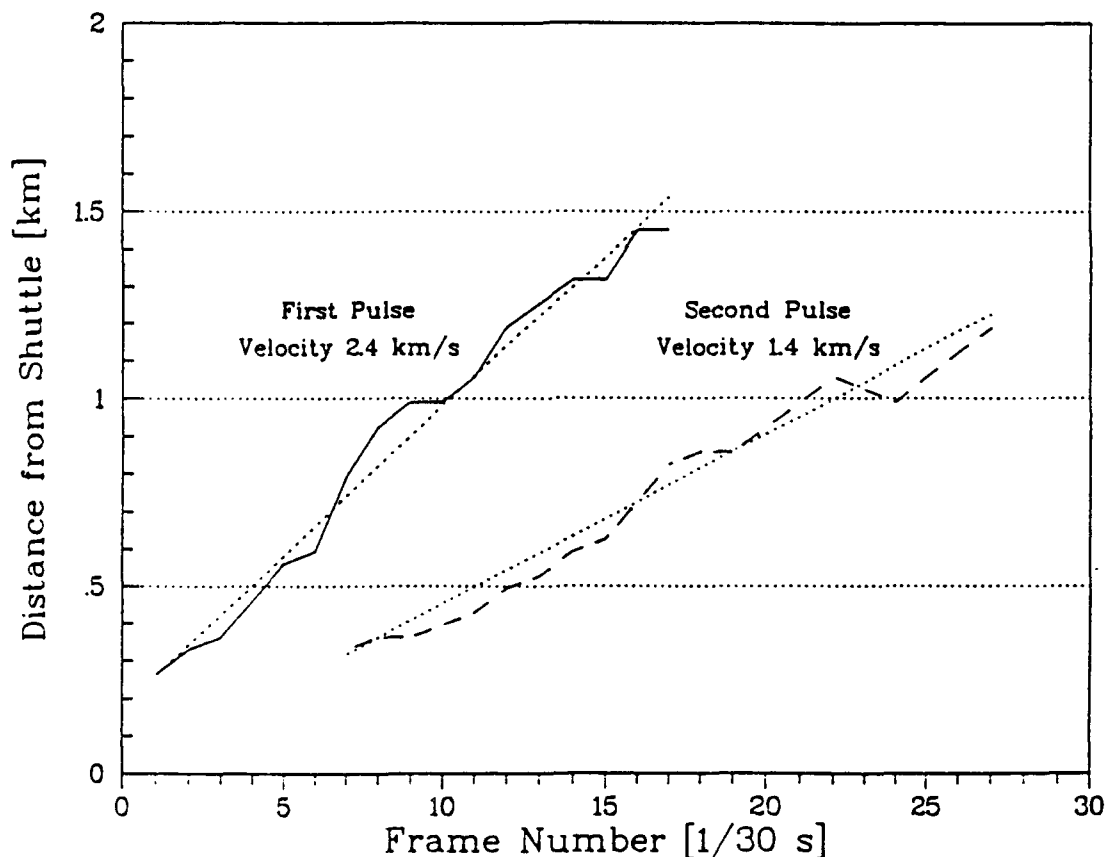
Figure 20. Distance from Shuttle Orbiter to the point of maximum radiance in the direction of the PRCS exhaust axis, in the two pulses in Figure 17. While the leading edges of the two bright patches extend further, their location is subject to larger experimental error. (The correction for non-perpendicularity to the exhaust direction is less than the measurement error.)

35

a longer time constant (almost 1 s) because the projected emitting area above threshold is increasing.

STS-29, Orbit 65 -- Second Pulse

The montage of frames in Fig. 17 shows (somewhat better than Fig. 16's presentation of the same video data) a wave of enhanced surface brightness whose crest moves in the direction of the exhaust from the two "D" thrusters, starting at or very near engine turnoff (Ref 22). The velocity of advance of its maximum brightness in the exhaust direction (Fig. 20), 1.4 km/s, is a little more than half that of the initial radiation front. (Difficulty in identifying the vehicle body introduces a small uncertainty in this measurement; as the exhaust direction of the "resultant" exhaust axis vector of these two symmetrically-firing engines is within 4 degrees of perpendicular to the line of sight from AMOS, no correction for a non-normal aspect is applied.) These velocities are somewhat less than those of the brightness fronts, whose accuracy of measurement is lower; as we will see later, the luminosity from a STS-33 ram firing initially moves out at about 4 km/s. The shallow minimum in brightness toward the symmetry center of this second glow is consistent with the operation of two individual thruster engines--the "D" units, whose exhaust axes are separated by 40°. No similar afterpulse from single engine F3U is above the threshold of sensitivity of the intensified AATS camera, despite the fact that its exhaust is directed only 35° into the wake hemisphere while the other two engines fire at 67° from the ram direction.

This second, more slowly expanding pulse is the source of most of the total optical yield after the PRCS engine firings end (see Fig's. 17-19). It may be provisionally associated with chemiluminescence from reaction of incompletely-burned rocket fuel (or intact MMH molecules) ejected in connection with shutdown of the thrusters (Ref 22)--and thus having less velocity than the combustion-product gases that adjust the aspect angles of Shuttle Orbiter. The eventual exponential decay of sterance in Fig. 19 would then represent the unimolecular reaction rate of this species with--most probably--the atmosphere's atomic oxygen. The rate coefficient derived from the 1 s time constant and the ambient [O] is -3 x 10^{-9} cm^3/s, which indicates an about geometric cross-section for the chemiluminescent reaction.

The energy yield in this second light pulse is of the order of 100 joules, which would result from emission of one visible photon in each of 3 x 10^{20} reactions. This figure may be compared with the rate of combustion of monomethyl hydrazine molecules when the PRCS thrusters operate, -10^{25}/s; thus unconsumed fuel ejected in a burst of duration less than 1/10 ms would produce the radiant intensities of the second pulse if each molecule reacted to produce one visible photon (or 1 ms duration for 1/1 conversion efficiency, and so forth). We note again that the reactions of bipropellant rocket fuel with the atmosphere (Type 3) in

36

Section 1) would in general result in a different emission spectrum from the processes involving the energetic molecules that are produced in the combustion of this fuel (Types 1) and 2)).

In summary, close observation of the emission pattern from the brief near-simultaneous firing of the three STS-29 PRCS engines shows two apparently different phenomena to be taking place. Initially luminosity of the general shape indicated in the early video fields/frames in Fig's. 16 and 17 expands toward the "D" exhaust direction, with the maximum surface radiances and total yield rates increasing as indicated in Fig. 19 and the apparent constant along-axis velocity derivable from Fig. 20. (Results from SOCRATES (Ref 5) indicate that the grow-in is an effect of the depletion of atomic oxygen concentrations in the near vicinity of the vehicle by inelastic and elastic collisions of the denser-than-ambient exhaust gas.) No similar wake-hemisphere glow (from the single thruster F3U) is above the sensor's threshold, indicating that the radiances in the retrograde direction are at least an order of magnitude lower--as is in fact observed in the STS-33 experiments reported below. About concurrent with shutdown a second pulse of enhanced radiance expands in the direction of the exhaust from the two near-parallel rocket engines, with markedly less velocity than the combustion-products gas; this radiation then quickly dominates the sterances. Its absolute *yield and later rate of decay* are consistent with reactions of a relatively small amount of incompletely-combusted fuel, presumably ejected (as a "transient" fuel-rich mixture) in connection with turnoff of the bipropellant rocket engines.

In this regard, the initial expanding luminous volume of the STS-29 engine burns is in a sense also consistent with being due to reactions of unburned fuel in a start-up transient, insofar as its early fractional rate of increase of sterance and its transverse extent are not substantially different from those of the afterpulse--although the 2.4 km/s velocity of its ring of maximum radiance is markedly higher. A comparison of emission spectra taken in the two periods would serve to check on this idea that the radiation from such short-lived thruster firings is due primarily to reactions of unburned fuel.

STS-33--General

The location of Shuttle Orbiter relative to AMOS in the first STS-33 experiment series (Table 1) is shown in Fig. 21. The line of sight is in all cases within about 30° of perpendicular to the spacecraft's trajectory, and the moon as well as the sun and moon are well below the horizon from the spacecraft's altitude during each overpass. Figure 22 illustrates Orbiter's aspect angles and el/az from the ground station at the start measurement of series A, which we have so far examined most closely. While the specific PRCS engines operated have

37

STS 33 VIEW GEOMETRY
START OF RAM BURN, ORBIT 21

FIELD OF VIEW
  3.5325 km (0.4°) HORIZONTAL
  2.6940 km (0.3°) VERTICAL

ALTITUDE = 315.7 km

RANGE = 529 km

LONGITUDE = 156.67°W

TRAJECTORY = 21.9°

ELEVATION = 34.2°

AZIMUTH = -5.8°

AMOS OPTICAL STATION
  156°15'W 20°43'N
  ELEVATION 3055 m
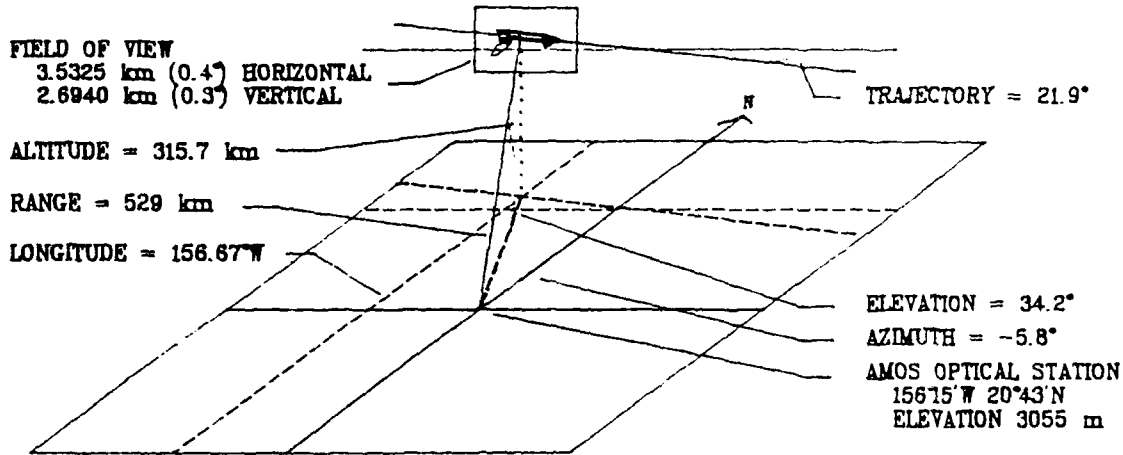
INERTIAL COORDINATES:

DECLINATION = 24.31°
RIGHT ASCENSION = 14.00°

EULER ANGLES (LVLH COORDINATES)

PITCH =   0.09°
YAW   = 359.79°
ROLL = 179.69°
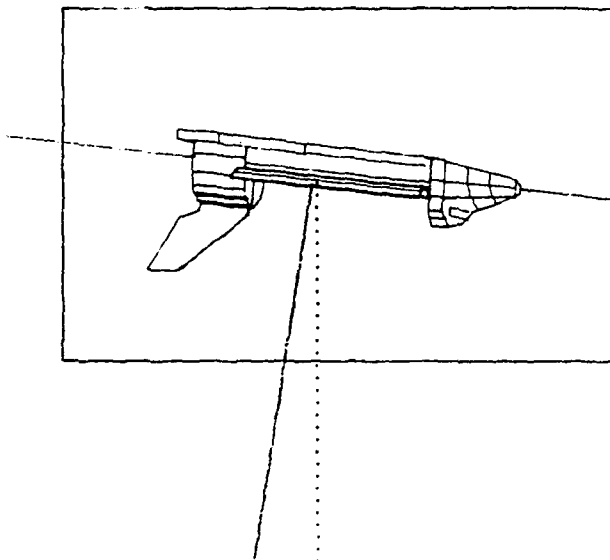
ANGLE BETWEEN SHUTTLE X AXIS
  AND POSITION VECTOR = 89.91°

ANGLE BETWEEN SHUTTLE Y AXIS
  AND VELOCITY VECTOR = 90.22°

Figure 21.   Location and orientation of Shuttle Orbiter at the start of Ram Burn A of the STS-33 experiment. Field of view refers to a plane perpendicular to the line of sight of the AATS tracking camera (not in the vertical trajectory plane). During the 27 s of the sequence of PRCS firings the range to AMOS decreases from 529 to 507 km, so that the plate scale increases by a total of -4% between Fig's. 23 and 25-26. Over this period the azimuth and elevation increase by -27° and 2°, and Orbiter's altitude increases by 4 km.
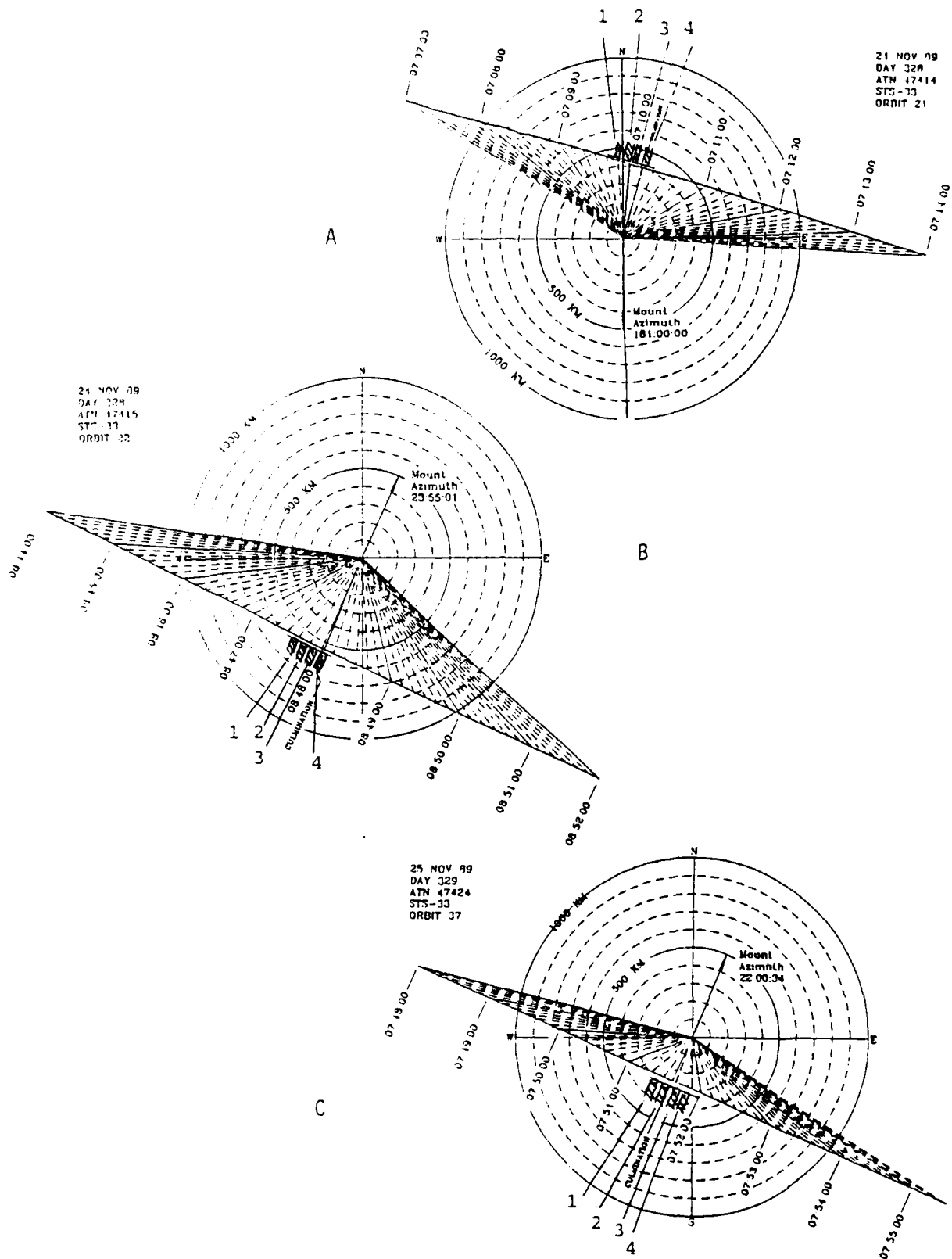
Figure 22.   Trajectory of STS-33 at the times of the ram (identified as 1), wake (2) and perpendicular-to-track (3 up, 4 down) PRCS engine firings. AMOS is at the center of the plots.

not been identified, their exhaust axes are known to be within a few degrees of the four directions relative to the trajectory that were specified in the experiment design.

Figures 23-26 show the development of the exhaust interaction region from these four PRCS firing directions, as recorded by the 0.5°-field AATS-MOTIF camera. All are from series A (elevation 34 to 67°) except the wake-directed burn from B (elevation 32°), which appears reversed from the others because in this orbit the spacecraft is passing south rather than north of the ground station. (Wake firing A extended over a 5 s period, discommensurate with the 3 s of the other three firings of the series.) Reference is made to the slight (10-15%) astigmatism of these video images, which is taken into account in our later quantification of these scenes.

Figures 27-29 are analogous single images from GEODSS of upward-, downward-, and wake-directed firings from experiment series A, B, and C respectively, after a more or less "equilibrium" radiation pattern (evident in Fig's. 23-26) is reached. (Orbiter moves too rapidly through the field of view of this "staring" camera to allow more than one engine burn per pass to be recorded; unfortunately no ram-directed firing was captured.)

We stress again that these brightness distributions represent column rates of visible chemiluminescence-producing reactions, rather than column concentrations of combustion-product (or other) species; and that the AATS camera is following the 7¾ km/s-velocity spacecraft--the origin of the 3½ km/s exhaust--, rather than the radiating gas volumes, whose velocities relative to the static atmosphere are not necessarily the same. The emission from the small area of these images that contains the spacecraft itself is treated in Section 5.

The exhaust interaction volumes can be seen eventually to extend beyond the 7 x 5¼-milliradian field of view of the AATS camera, except in the perpendicular downward-directed PRCS firing of Fig. 26 where severe overexposure of the image of the spacecraft area proper (presumably due to a thermally-radiating combustion volume or a spacecraft surface directly illuminated by this rocket volume being in the camera's line of sight) may be forcing down the video gain. This overfilling of its field imposes some limits on the utility of the radiometric data from this narrow-field sensor. The consistency of the AATS images with those from the wider-field GEODSS camera is illustrated by the comparison between isophote plots of the series B wake firing at 07:51:34.37 in Fig. 30a. This celestial scene-following sensor appears to show a longer, thinner luminous area, and does not resolve the lobed brightness structure that shows clearly in Fig. 24.

Applying the radiometric calibrations as discussed in Section 3 to the space-integrated output currents, we find that the sterance derived from the GEODSS camera data at 07:51:34.37 is about a factor 40 greater than that from the concurrent AATS video frames
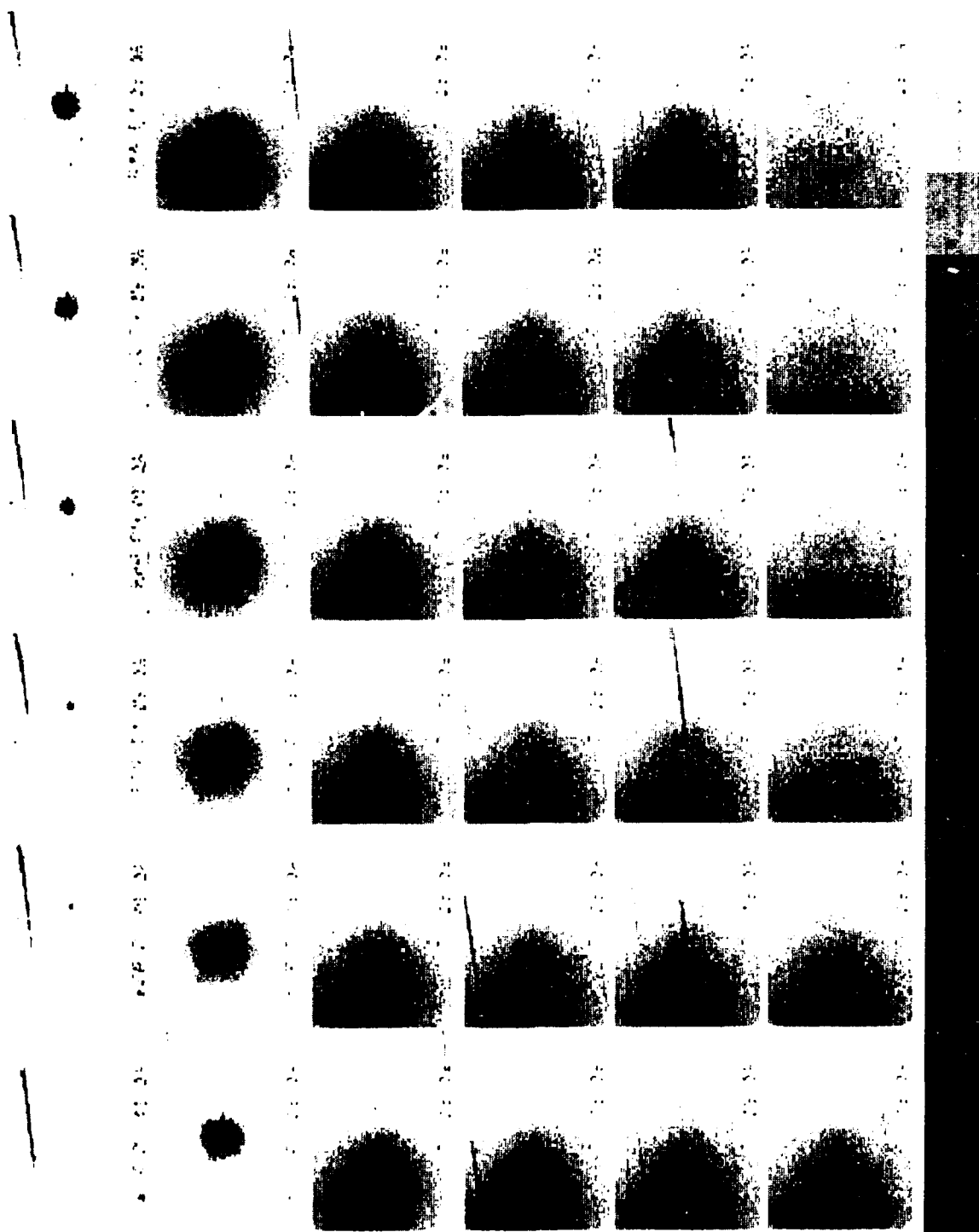
Figure 23. Montage of STS-33 Ram Burn A. The top row displays the first 6 video frames, and subsequent rows are consecutive averages of 4 frames. An 8 frame average background (pre-firing) was subtracted from these images. (See also Figure 45.)

41

Figure 24. Montage of STS-33 Wake Burn B. The timing of these images is the same as the format of Figure 23. To bring out detail we have multiplied the photocurrents over baseline by a factor 5.

42
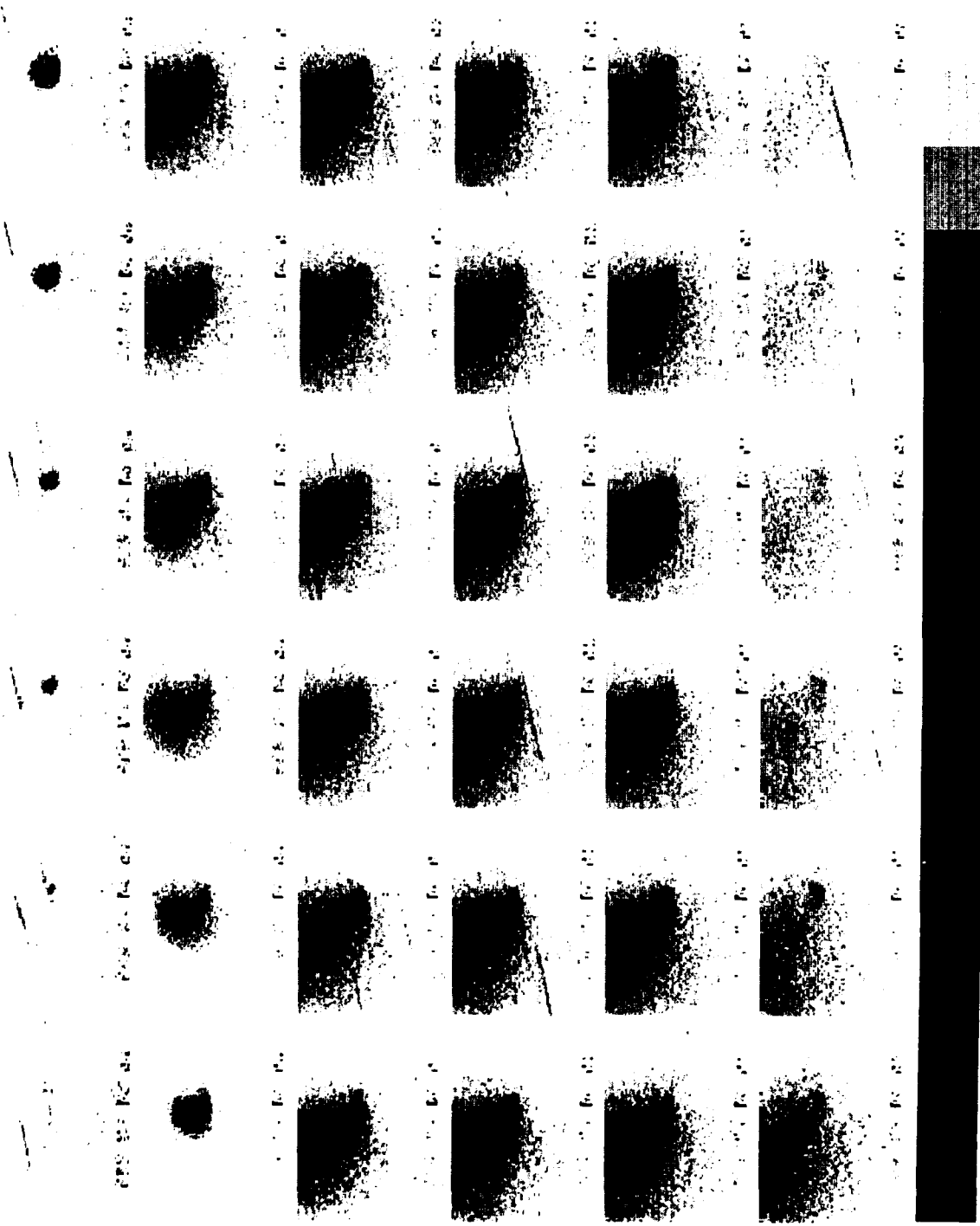
Figure 25. Montage of STS-33 Perpendicular (Upward) Burn A. The timing of these images is the same as the format of Figure 23. Photocurrents over baseline are multiplied by a factor 2.
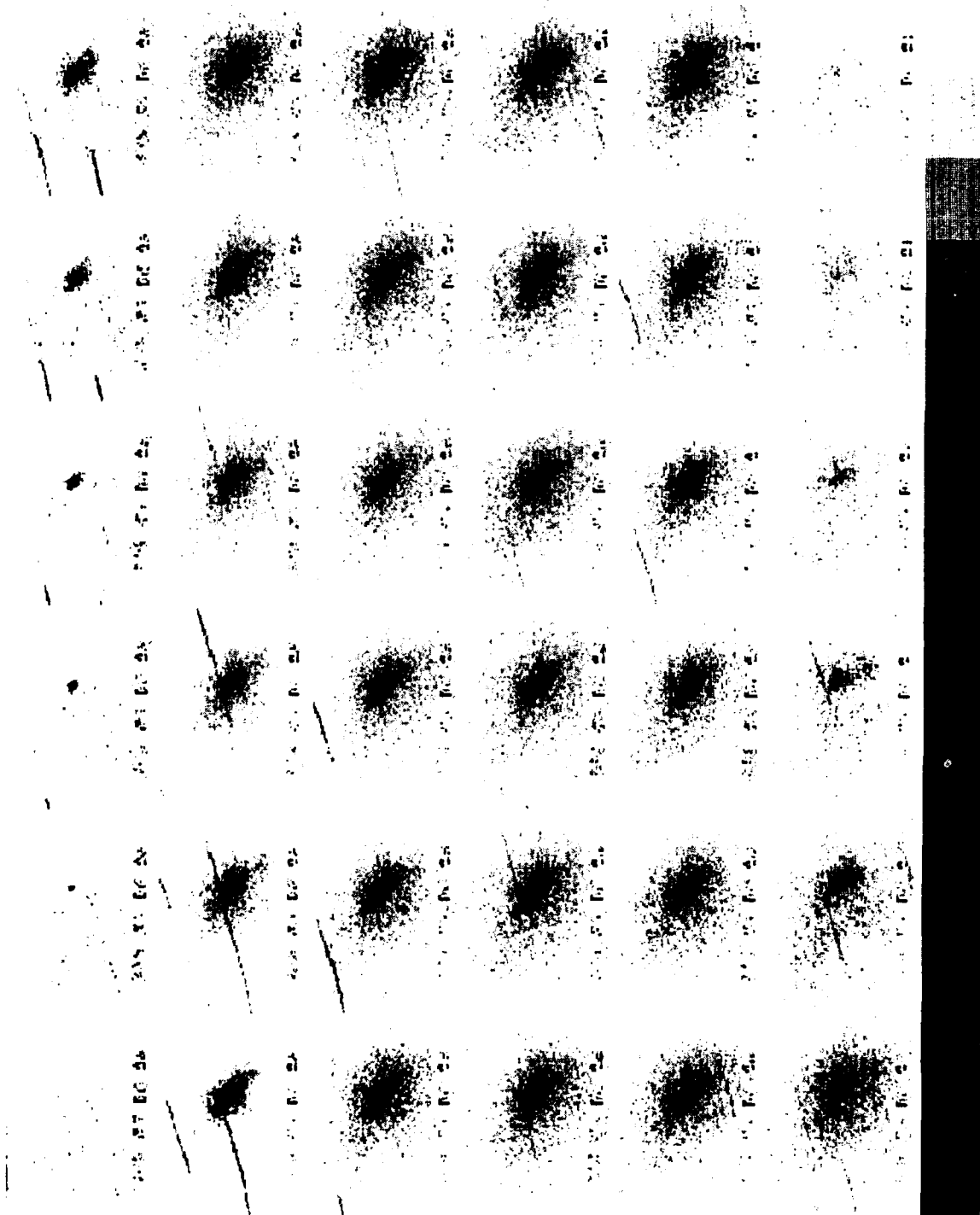
Figure 26. Montage of STS-33 Perpendicular (Downward) Burn A. The timing of these images is the same as the format of Figure 23. Photocurrents over baseline are multiplied by a factor 2.
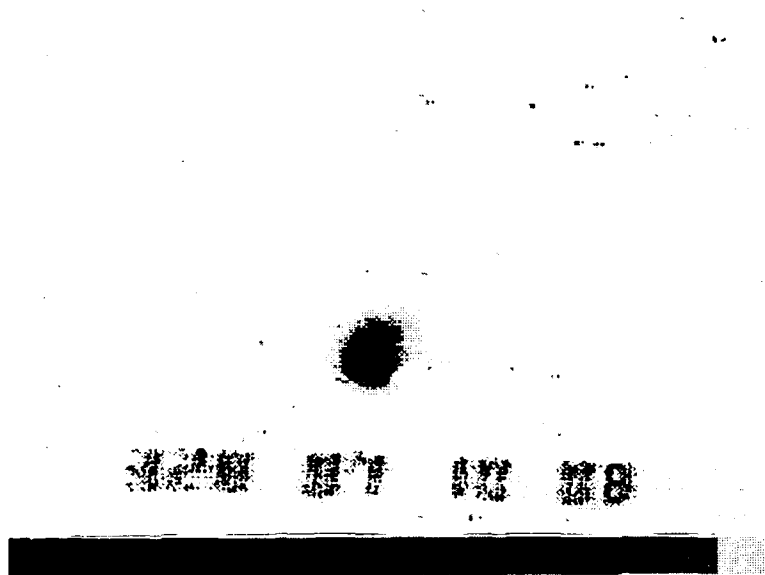
Figure 27.

GEODSS frame of Perpendicular (Downward) Burn A at 1.5 s into the burn. Severe saturation is evident in the central portion of the cloud, most probably due to thermal radiation from a PRCS engine.

Figure 28.

GEODSS frame of Perpendicular (Upward) Burn B at 1.5 s into the burn.
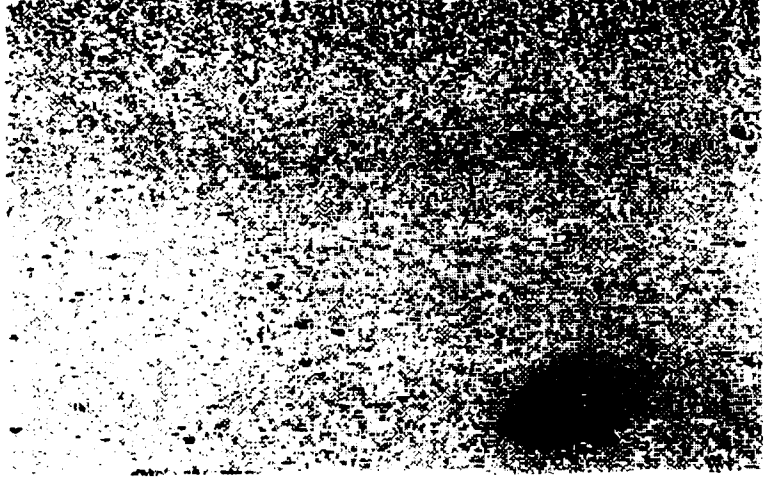
Figure 29.

GEODSS frame of Wake Burn C at 1.5 s into the burn. To improve contrast the photocurrents over baseline were multiplied by 5 relative to the above two figures.

(four of which were coadded to improve signal/noise in Fig. 30). A review of the isophote plots from the AATS video images (Fig's. 23-26) indicates that this discrepancy can not be fully ascribed to vignetting--decrease toward the edge of the field in irradiance at the focal plane per unit scene radiance--by this camera. Furthermore the "drag" of the image of objects moving at the orbital velocity in a single 1/30-s GEODSS video frame is only about 270 m, which is very small compared with the along-wake distance scale; hence the difference in spatial distributions of radiances apparent in Fig. 30 would not be an effect of camera tracking or the lack thereof. The observed differences in absolute total sterances and between the two image distributions most likely result primarily from the data processing, and are perhaps related to the subtraction of baseline photocurrent in the AATS images--and the ambiguities of absolute calibration of 0.5°-field, tracked AATS camera against the curiously-persistent images of stars (such as is shown in Fig. 15).

STS-33 -- Ram Burn A

As the kinetic energy available for chemiluminescent reactions between exhaust and atmospheric species is a maximum in ram-directed PRCS firings, the signal/noise ratios in the video images are (in consequence) high, and the scene radiances show symmetries that simplify their numerical description, we have initially concentrated on Ram Burn A. We reduced the image data summarized in Fig. 23 with a "Datacube" video processing system (Ref 2), using MaxVision MV1 software that PhotoMetrics had modified in related image data extraction-reduction-analysis programs. Figure 31 is a set of horizontal traces through the frames in Fig. 23, intercepting the spacecraft's image.

To provide baseline photocurrents, we digitized and then averaged eight consecutive video frames from the period immediately before the firing, in a sequence selected to exclude visible stars. To maintain all the baseline-subtracted values above zero, we then added a constant 10 digitization units to each pixel in the image. Figure 32 shows the resulting histogram of pixel values in three early frames; the halfwidth of the remaining spread in the areas where the exhaust luminosity does not image (determined by subtracting a randomly-selected frame from the mean) can be seen to be about 16 digitized photocurrent units, and its mean value is 10 units as expected. The histogram also shows, albeit with much lower resolution, the probability of occurrence of visible radiance in the exhaust interaction volume, which is a parameter in the assessment of surveillance scenarios. While this distribution at first appears to be flat, closer inspection indicates that it has a low-contrast maximum characteristic of a broad Gaussian, which (as can be readily shown) is the expected occurrence probability in 2-D Gaussian brightness distributions--on which more immediately below.

46

STAR 44

3X

a)

(Star)

b)
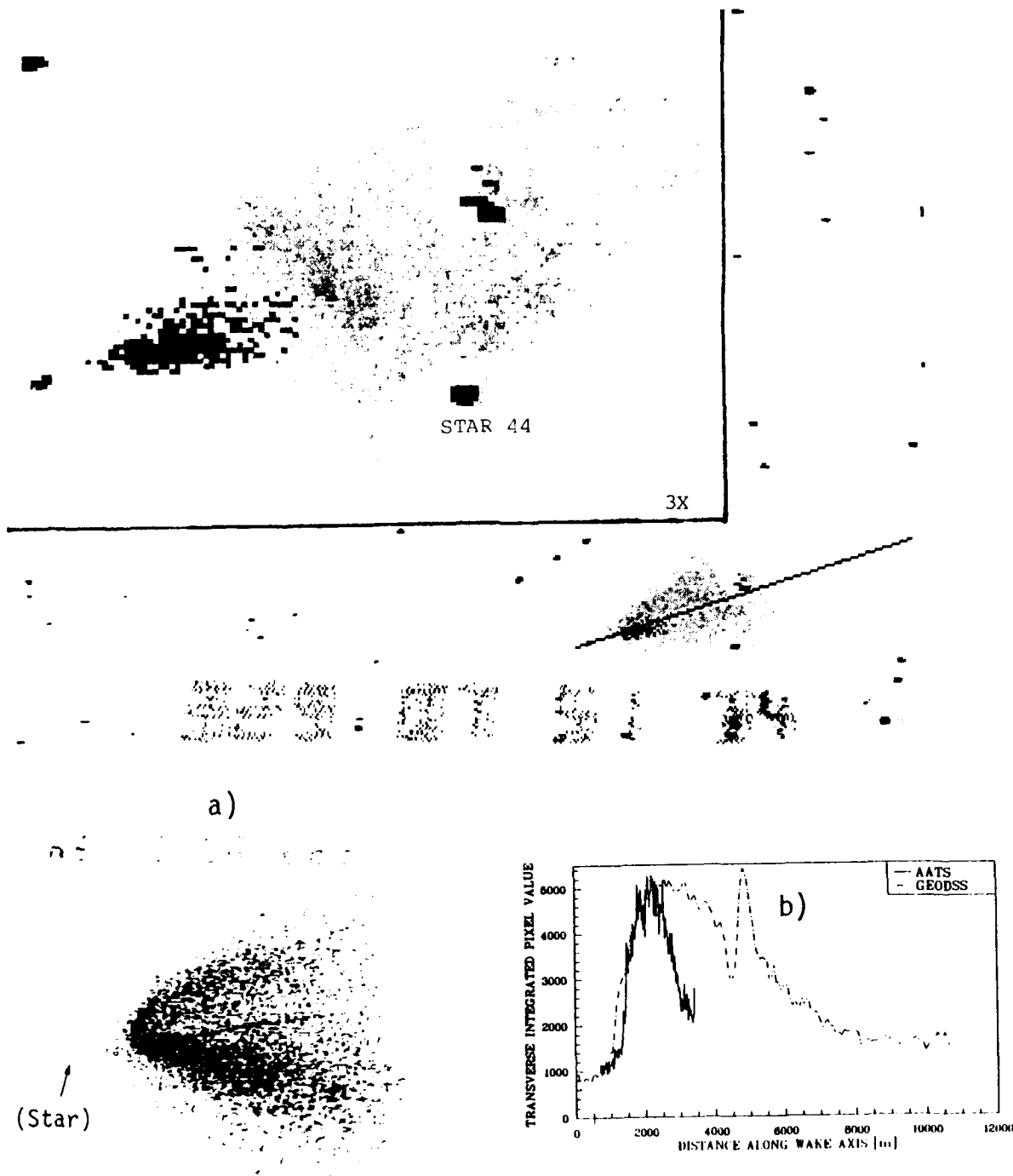
Figure 30.   a) Comparison of AMOS-AATS image (8 frame average) and GEODSS image (one frame) of Wake Burn C at 07:51:34.37, 1.50 s after turnon, at the same plate scales.   b) Normalized profiles of photocurrents summed along lines perpendicular to the "axis" of the luminosity (indicated by the line at lower right of the GEODSS image).   Both data presentations show substantially more radiation in the GEODSS camera image (refer to the text).

47
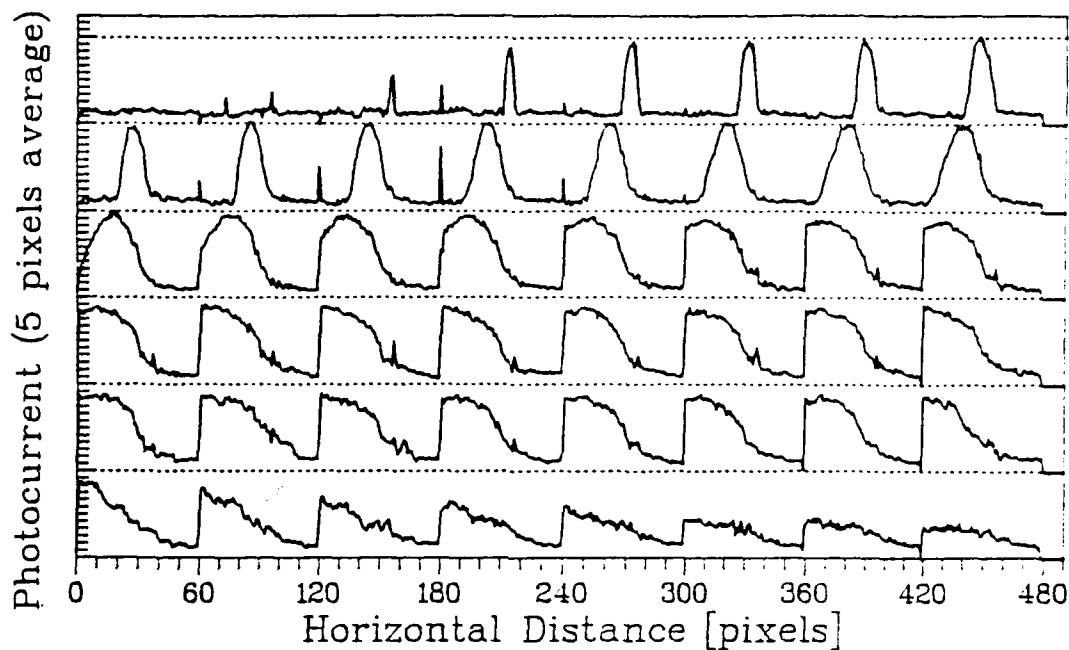
Figure 31.   Horizontal traces passing through the spacecraft image area. The first two rows of images display consecutive frames 1 through 16 of Ram Burn A (see Fig. 23). The four lower rows display every fourth frame in the time sequence. The leading edge of the radiating volume starts to go out of the AATS camera's field of view in Frame 15.
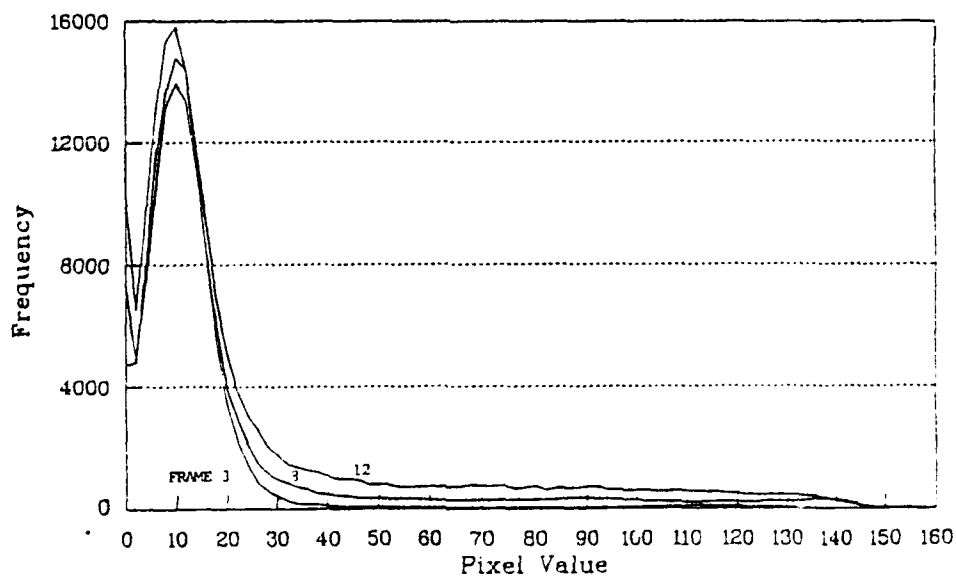
Figure 32.   Histograms of occurrence of digitized AATS photocurrents after the baseline correction described in the text, STS-33 Ram Burn A.

As the exhaust interaction luminosity does not have clearly demarcated edges, it is useful (indeed, necessary) to define its "photogrammetric" characteristics from its photometric properties for deriving growth rates and velocities. Within a very few frames after engine turnon the surface brightness distributions in the horizontal direction become closely Gaussian, as Fig's. 33 and 34 (and 45) indicate. The distributions in vertical scans (Fig. 35) are also essentially Gaussian. (The radiating volume appears physically separated from the space vehicle itself.) Figures 34a and b are horizontal traces and best-fit Gaussians for two further frames extending to -0.8 s, and Fig. 34c presents the fits for five frames out to 2.4 s. Figure 36 shows the Gaussian half widths and maximum pixel values (digitized photocurrent above baseline) for the first 2.4 s of the ram burn, along with a plot of the square of the width against time since the PRCS engines were turned on. This halfwidth W is the standard

Frame AR13BS
Gaussian fit: $Ae^{-(x^2/2W^2)} + B$
W = 57.3   A = 133.4   B = 4.95
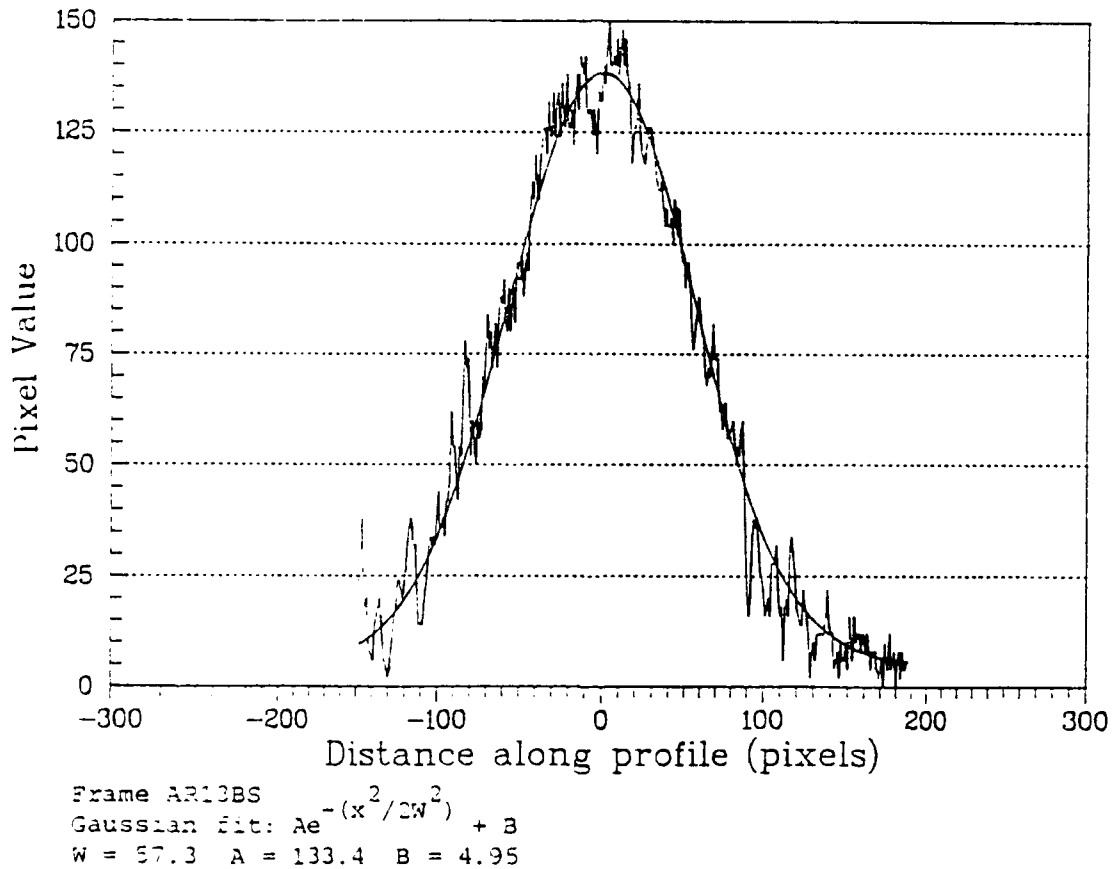
Figure 33.   Horizontal trace through Frame 13 of STS-33 Ram Burn A, with Gaussian fit to the photocurrents in the mathematical format stated.

49
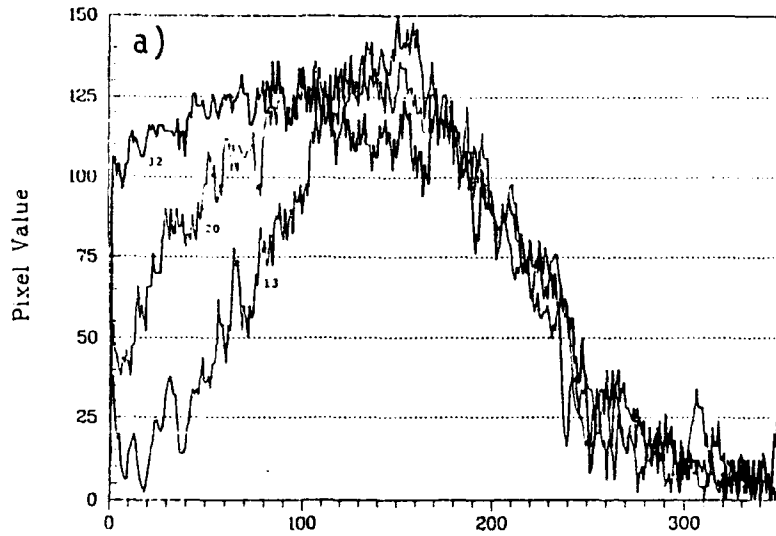
Figure 34.

a) Horizontal traces through Frames 13, 20, and 32 of STS-33 Ram Burn A. b) Gaussian fits to these three photocurrent traces. c) Gaussian fits to similar traces through Frames 12, 16, 28, 40, and 72. The parameters of Gaussian fits for Frames 13, 20, and 32 refer to the format in Fig. 33.
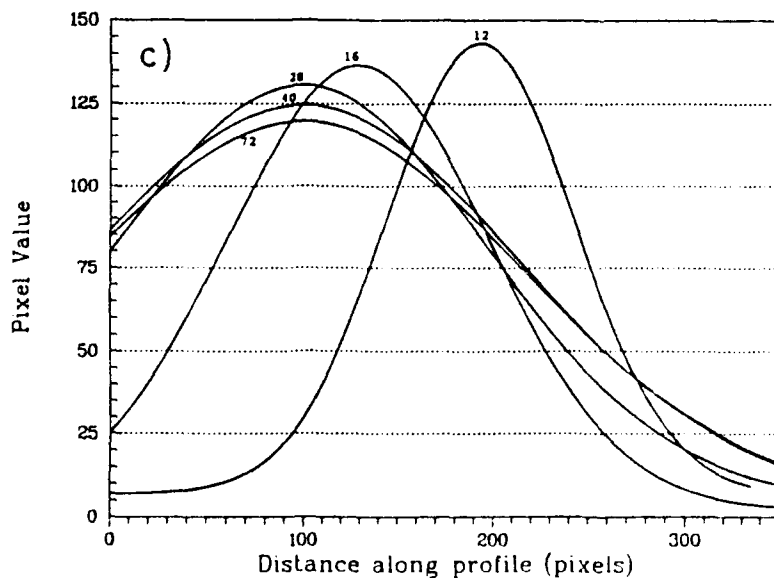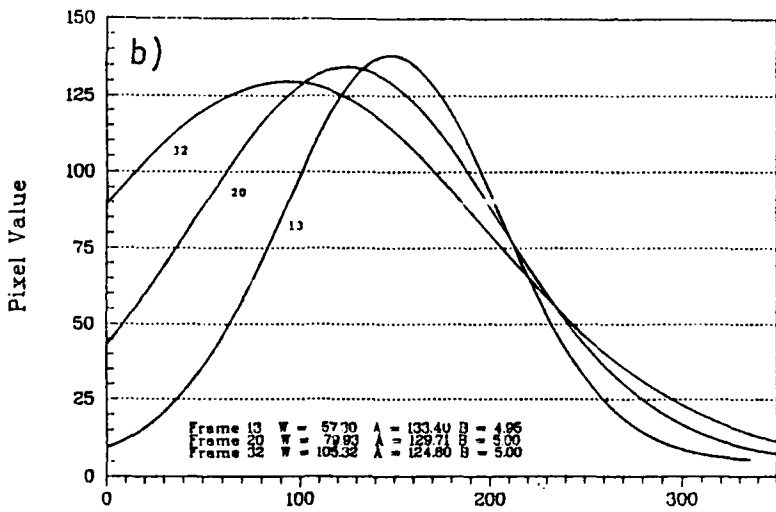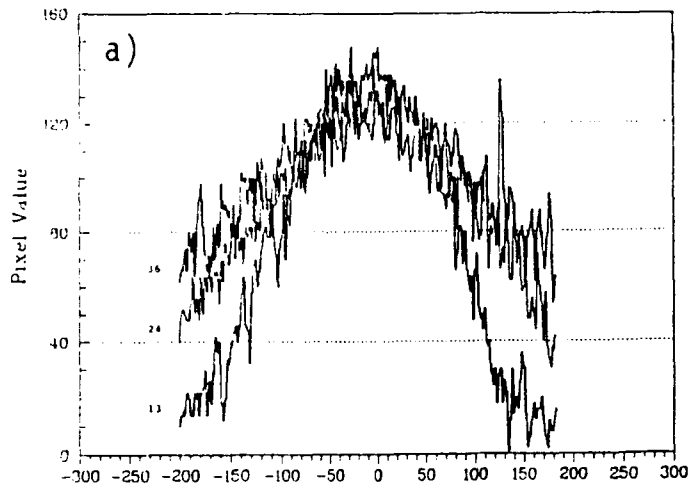
Figure 35.

a) Vertical traces through Frames 13, 24 and 36 of STS-33 Ram Burn A. b) Gaussian fits to these three photocurrent traces. c) Gaussian fits to traces through frames 12, 20, 28, 40 and 72.

51
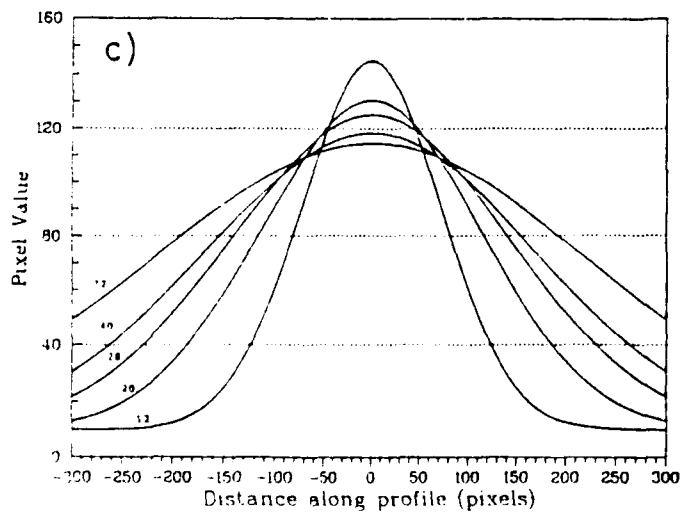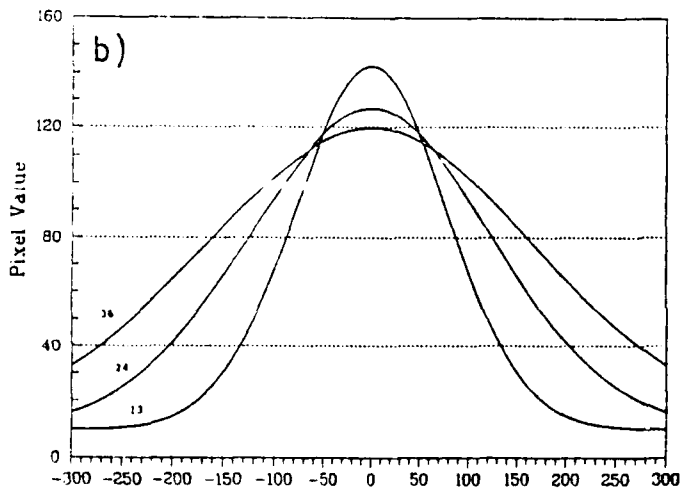
quantity defined in Fig. 33: the radiance is a factor e below its maximum at $\sqrt{2}$ W pixels from the center of symmetry of the luminous volume.

For these frames in which this volume quite obviously extends beyond the camera's field of view, we assumed that it maintains its near-circular symmetry and extrapolated those brightnesses within the field to reconstruct a complete image. This procedure was applied after Frame 15, and was stopped when the video brightnesses no longer showed a maximum (i.e., turnover) within the image field--at 2.4 s--, where we judged it would no longer be reliable. As the radiances made successively poorer fits to a Gaussian in the period before Frame 10 (1/3 s after turnon; see Fig's. 45 and 46), these very early data points in Fig. 36b are subject to relatively high error.

The maximum radiance of the exhaust-interaction volume, in its projection to AMOS, can be seen to increase up to about 1 s after its initial very steep rise, and then remain about constant. The Gaussian widths increase monotonically, and make a reasonably good linear fit to the square root of time (Fig. 36b). While this behavior resembles that of classical diffusion, the interpretation is complicated by the continuous replenishment of both the exhaust and atmospheric-target gases. (Recall that the video camera is tracking on the fast-moving spacecraft.) The slopes of the best-fit lines in Fig. 36b are

6.4×10^5 m^2/s in the horizontal direction   and

4.7×10^5 m^2/s in the vertical direction.

Taking into account our definition of W, these figures convert to "diffusion coefficients" of 1.2 and 0.9×10^6 m^2/s respectively. For comparison, the diffusion coefficient of O at the ambient atmospheric density and nominal temperature of 5×10^8/cm^3 and 1000K would be 3.7×10^6 m^2/s.

Figure 37 shows the horizontal distance from the "image" of Shuttle Orbiter to the leading and trailing edges of the radiating volume (taken as being ± 2W pixels from its center of symmetry, where in practice the radiances become indistinguishable from baseline) in the 2.4-s data period, and Fig. 38 plots the derived apparent velocities of these so-defined boundaries. The nearer "edge" at first moves away from the source of the high kinetic energy exhaust gases, and then as the reaction volume expands it moves back in the 7¾ km/s-velocity coordinate system. The derived initial velocity of the chemiluminous-reaction front, 4 km/s, appears to be somewhat higher than the 3½ km/s directed velocity of the rocket exhaust, a difference that is in the expected direction in view of the finite temperature of the flowing gas. (Compare also the outward velocities of the STS-29 brightness maximums--not fronts--in Fig. 20.) This velocity decreases to about 1000 m/s about 1 s into the burn. We stress again that these velocities refer to the moving coordinate system of Shuttle Orbiter, rather than to the stationary atmosphere; after -1 s, they can be interpreted as phase velocities.
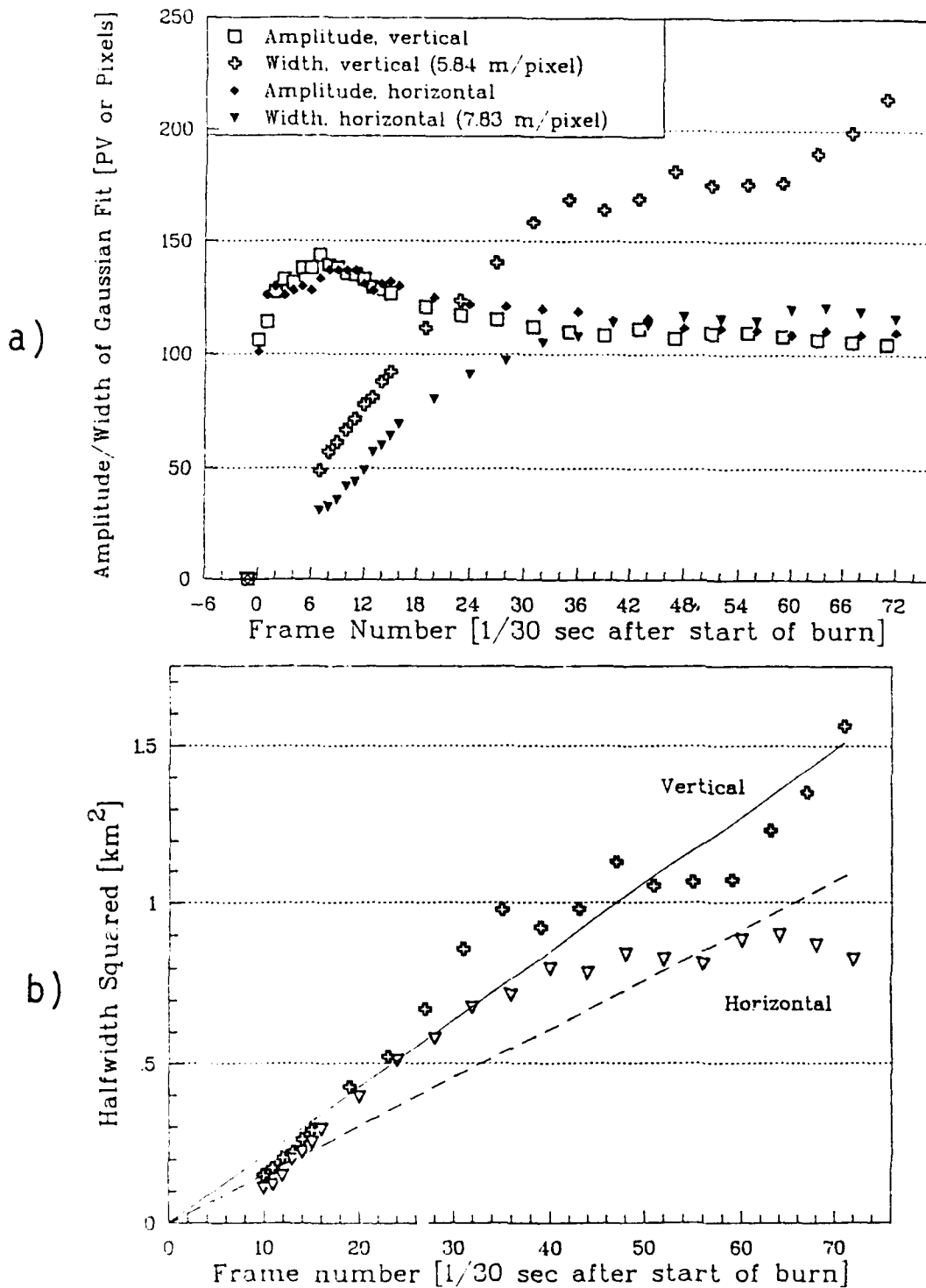
Figure 36.   a) Gaussian halfwidths (as defined in Figure 33 and the text) and maximum digitized photocurrent (labeled Amplitude) in vertical and horizontal scans through STS-33 Ram Burn A.   b) Dependence on time of the square of the "halfwidths" defined in Fig. 33.   The straight lines are least-squares linear fits with data points given equal statistical weight.

53
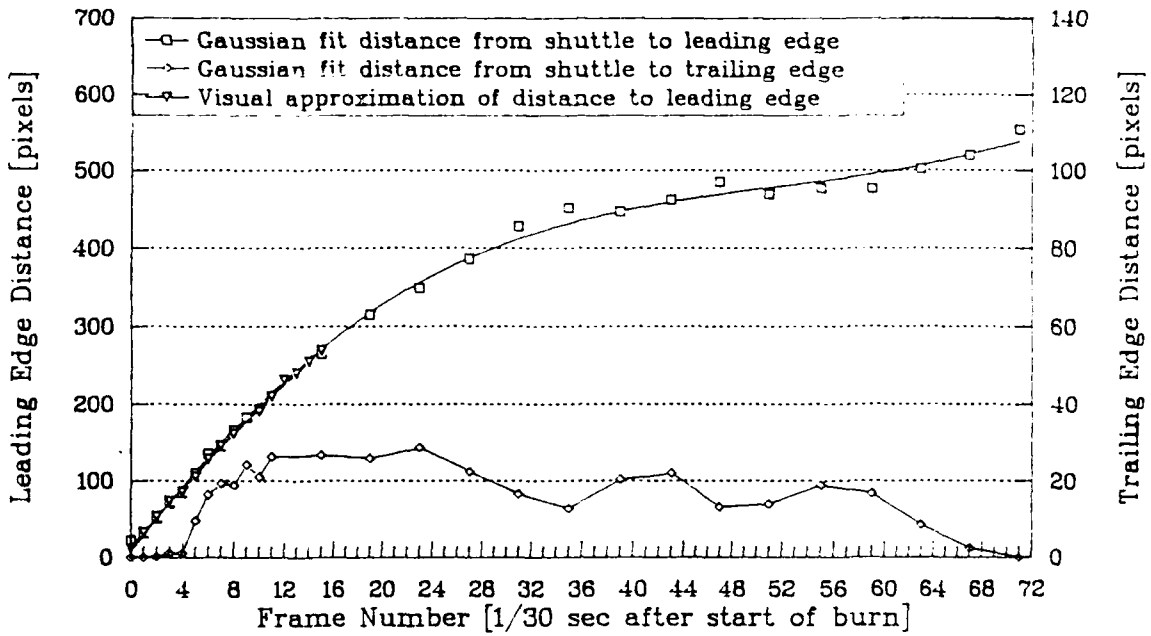
Figure 37. Horizontal distances from Shuttle Orbiter to the leading and trailing edges of the exhaust interaction volume of STS-33 Ram Burn A, defined as ± 2W from its center. 1 pixel = 7.3 m in object space.
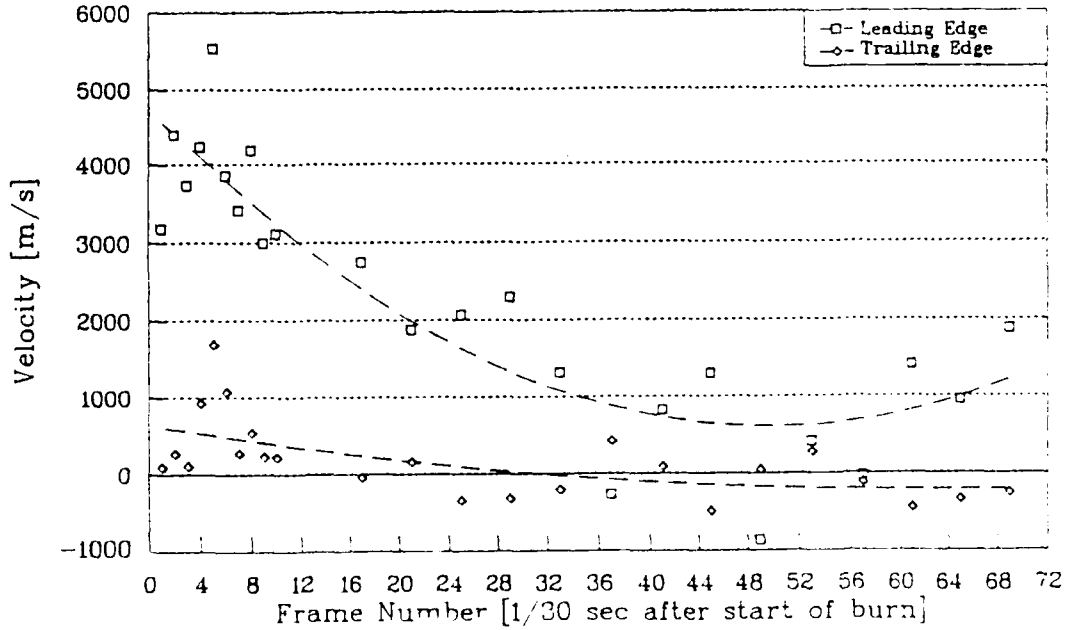
Figure 38. Horizontal velocities of the "edges" of the STS-33 Ram Burn A volume, derived from Figure 37.

54

Figure 39 shows the sum of the digitized photocurrents above baseline from the exhaust-interaction luminosity, in the initial 2.4-s engine burn period. The data from frames beyond 15, in which some of the volume lies outside the AATS camera's field of view, have been corrected applying its Gaussian "shape". A conversion of these visible-light yield rates into sterances and a comparison with results from other PRCS firings appears later in this Section.

Figure 40 is a similar plot of these summed photocurrents-above-baseline within about 15% of the AATS camera's field of view--the bounds are pixels x = 20, y = 149 (measured downward from the top of the frame); x = 322, y = 149; x = 20, y = 271; x = 322, y = 271--after the PRCS thrusters have turned off. We reduced each individual video frame in a search for waves or other structure in the decay; none is apparent. The relative irradiances decrease about exponentially with a time constant of 1.25 s, or about half again that of STS-29 (compare Fig. 19). As the radiances may not be decreasing uniformly over the scene (see Fig. 31), this signal--in contrast with that from STS-29--does not quantitatively represent the relative sterances from the exhaust interaction volume. Indeed, the original video display gives an impression of a "dark pulse" extending outward from the spacecraft when the thruster engines turn off, which we return to in the next but one subsection; this brightness minimum is evidenced in late frames of the montage of Fig. 23 by the concavity of the radiance contours toward Orbiter. The persisting luminosity can be interpreted as due to the continuing reaction of generally outward-moving exhaust gases and unburned fuel, as they encounter undepleted oxygen atom densities. The out-of-field air volumes would thus be decaying more slowly than those whose radiances we are able to measure--at least in the first few second after shutoff--, so that the characteristic time of decrease of the total sterance would be somewhat longer than would be derived from Fig. 40.

STS-33 -- Perpendicular Burn A

The generally upward-directed perpendicular-to-track firing shows the radiating volume sweeping backward, as would be expected from the delay in chemiluminescent reactions resulting from the finite transport time of the thruster exhaust gases. Since the luminosity starts to extend outside of the AATS field within ~¼ s (see Fig. 25), and has an unsymmetric shape that does not lend itself to extrapolation, the information about the exhaust interaction can be extracted from these data is less accurate than that from the ram burns. Furthermore, as the azimuth (roll) direction of the exhaust axis is not yet available, an absolute distance scale in the direction of firing cannot be assigned to the images; that is, although Orbiter is known to be in "upside-down aircraft" orientation mode (see Fig. 21), since several of its bottomside PRCS engines have substantial exhaust components in the Y or roll direction (see

55
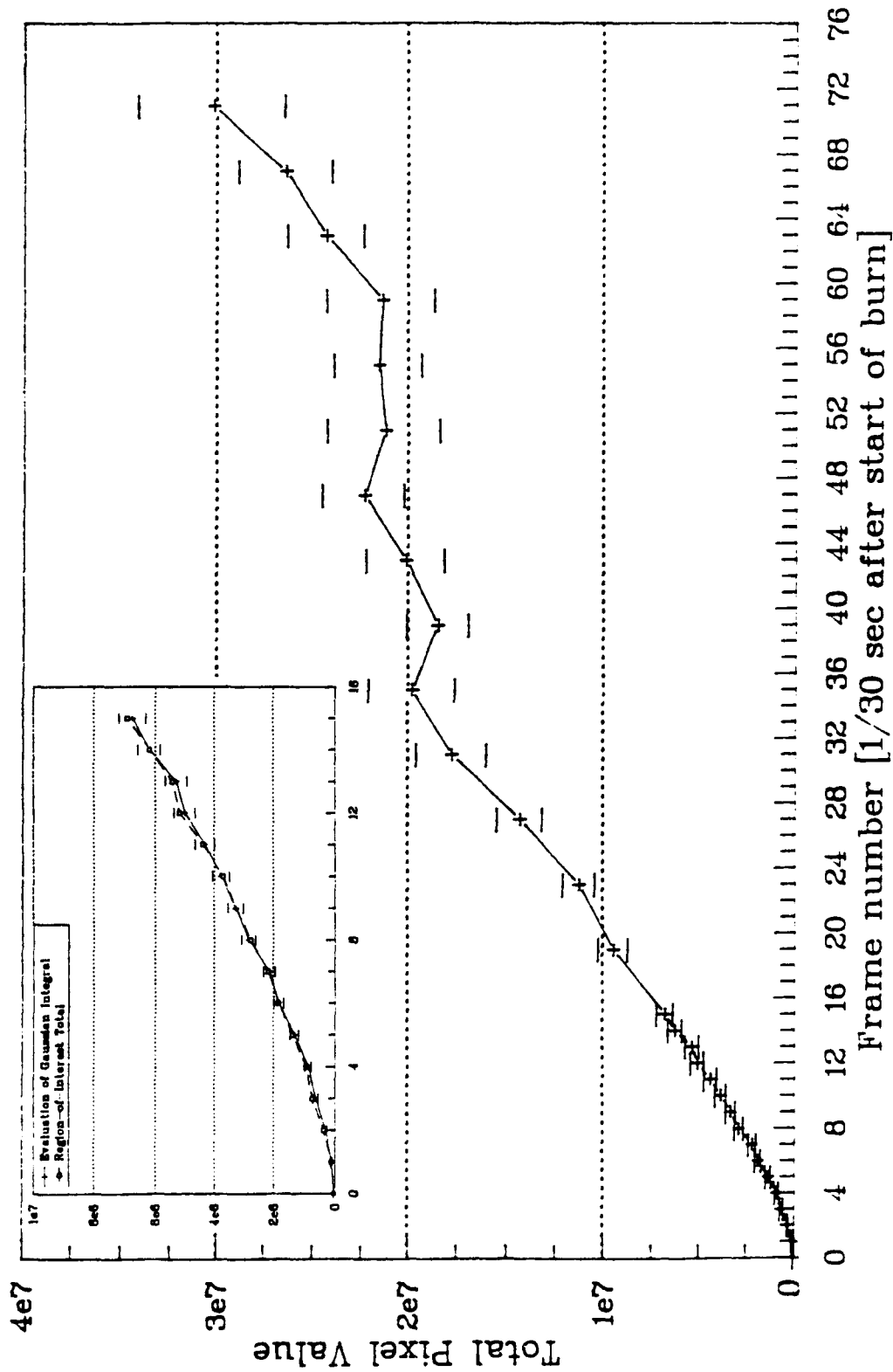
Figure 39. Sum of photocurrents from the exhaust interaction volume of STS-33 Ram Burn A. The squares show the actual spatial integrals corrected for the out-of-field component assuming an essentially spherically-symmetrical Gaussian, and the horizontal lines the values derived from the Gaussian widths in Fig. 37. (Figure 51 shows these data as sterances.)

56

DECAY OF EXHAUST CLOUD
AFTER ENGINE CUT-OFF

STS 33, RAM BURN A
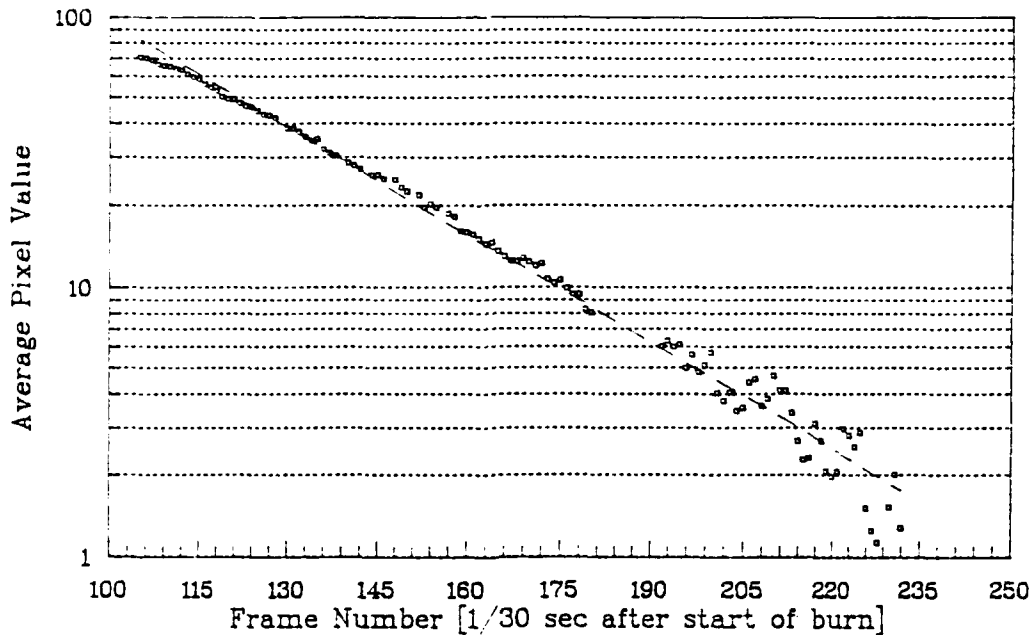
Figure 40. Relative sterances from a segment of the STS-33 Ram Burn A exhaust interaction volume after the PRCS engines shut off. The region of the video frames is x = 20 to 322, y = 149 to 271. The time constant of the exponential best-fit shown is 1.25 s.

Fig. 1) the angle between the exhaust and the line of sight from AMOS is yet to be determined.

Figure 41 shows the upward growth and maximum width of the luminosity, measured to the points at which the video signal disappears into the noise of the baseline current. The apparent mean upward velocity, uncorrected for foreshortening due to deviation of the exhaust axis from perpendicular to the line of sight is 2.7 km/s. This figure is somewhat less than the 3½ km/s directed exhaust velocity, presumably because of this foreshortening (or maybe because the exhaust axis departs from vertical. The maximum width of the detectable luminosity--not a particularly meaningful physical quantity--initially increases at 2.3 km/s.

Figure 42 shows vertical traces extending through the spacecraft in the initial 2/3 s, and Fig. 43 is a set of horizontal photocurrent profiles through the area of maximum width of the exhaust-interaction luminosity up to 1 s after engine turnon. The distance scales given in the caption are subject to the above-mentioned caveat about the projection of the exhaust axis into the plane perpendicular to the camera axis.
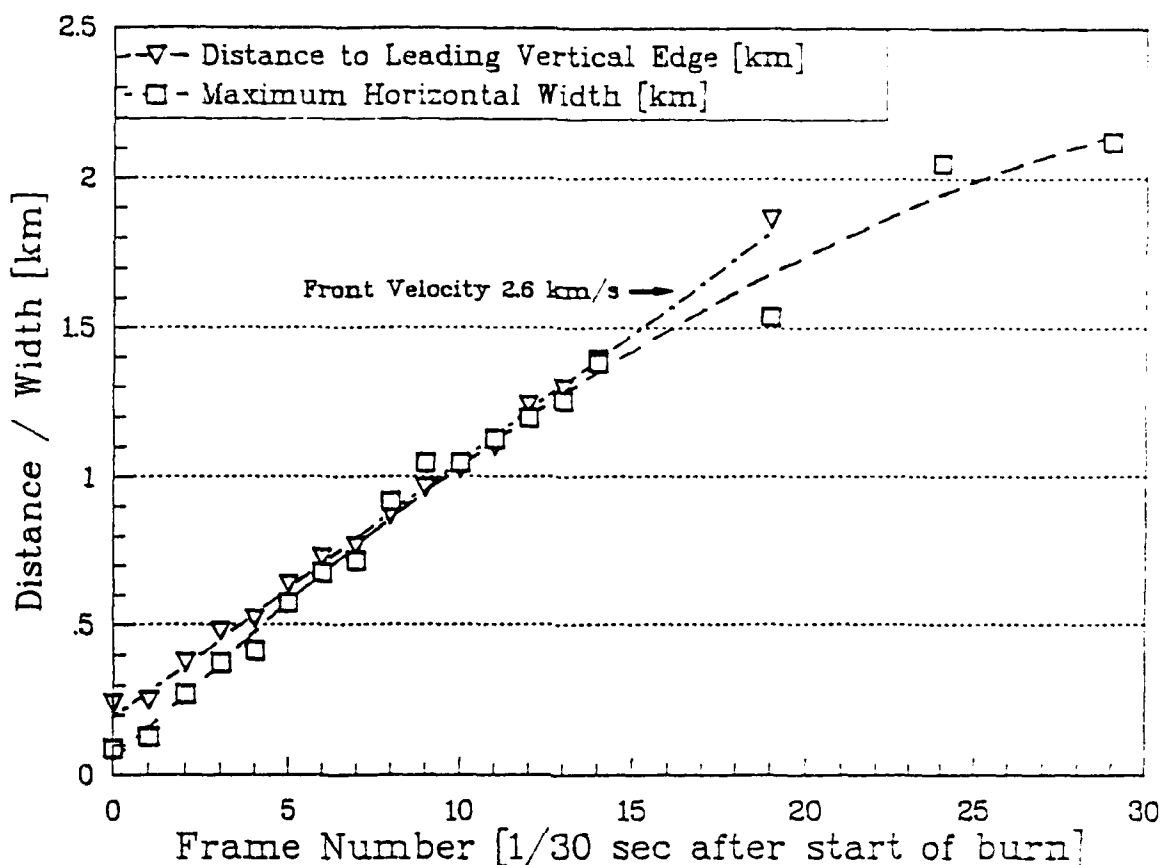
Figure 41.   Apparent maximum width of the perpendicular-to-track upward Burn A of STS-33 and distance from Orbiter to the upward leading edge. 1 pixel = 7.14 m horizontally, 5.32 m vertically.

Figure 44 shows the spatially-integrated photocurrents from the exhaust-interaction volume, out to about ½ s after turnon. We estimate from the montage of Fig. 25 that the maximum sterance from the perpendicular firing is twice that reached by this time. Its absolute value derived from the 0.5° AATS camera calibration in Section 3 would then be >90 watts/sr.

Early and Late Radiation

Figures 45 and 46 are enlargements of the initial ~1/3 and 1/5 s of images of STS-33 Ram Burns A and C. A finger of enhanced radiance extends from the clearly-defined spacecraft area into the large selfluminous volume, which in Fig. 45 can be seen to take on the quasi-Gaussian shape discussed above by Frame 10. (The early "Gaussian" widths in Fig. 36 were estimated from these data.) This radiating area appears bifurcated early in Burn A, with an angle of either 20° or 40° between the two maxima (the images are somewhat ambiguous

58

PROFILES OF EXHAUST CLOUD
Y DIRECTION
Perpendicular Burn (Away)
Orbit 21
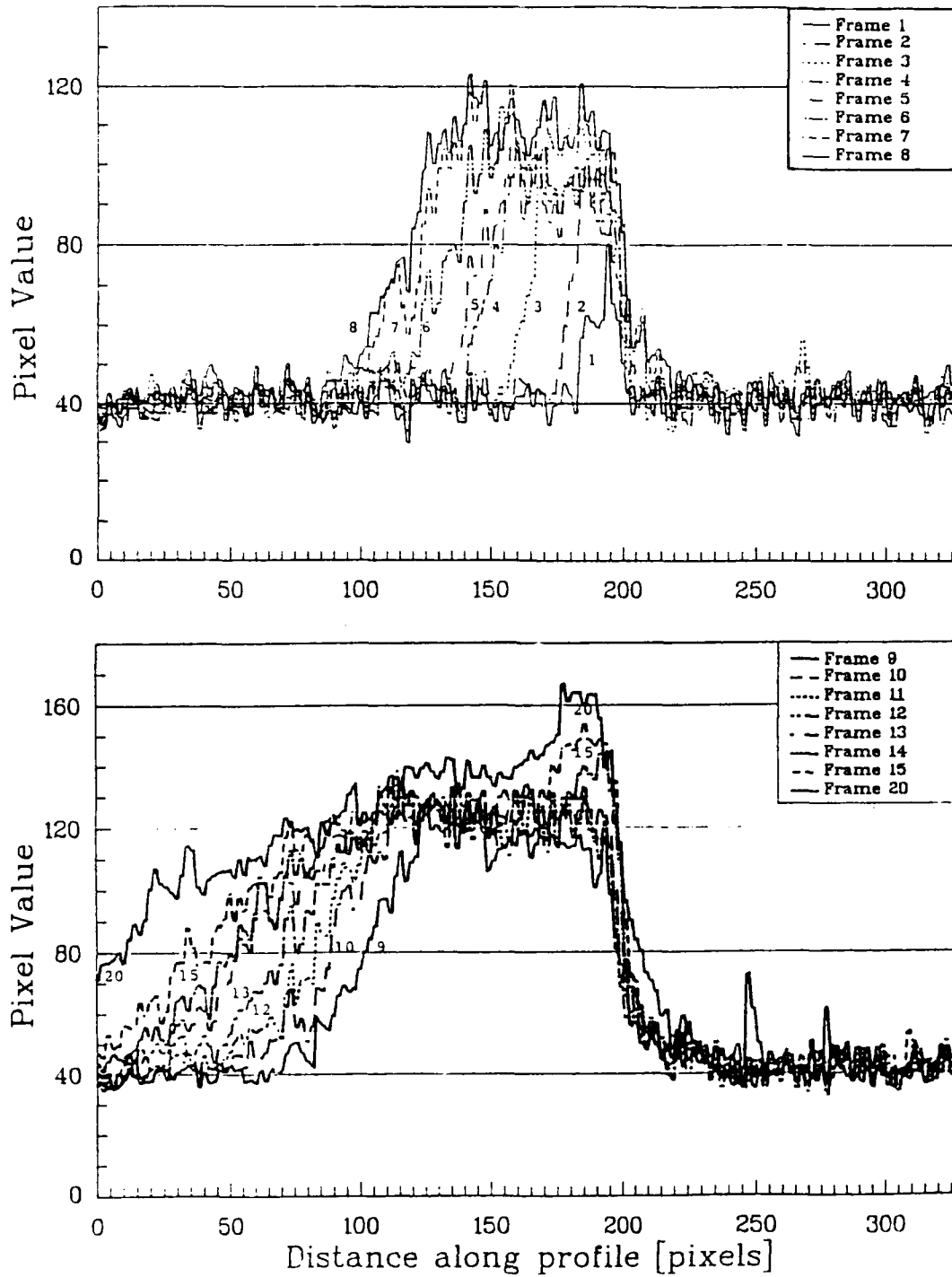
Figure 42.   Vertical profiles of STS-33 Perpendicular Upward Burn A through Shuttle
              Orbiter. 1 pixel = 5.32 m.

59

CROSS SECTION OF EXHAUST CLOUD
X DIRECTION, MAXIMUM WIDTH
Perpendicular Burn (Away)
STS 33, Orbit 21
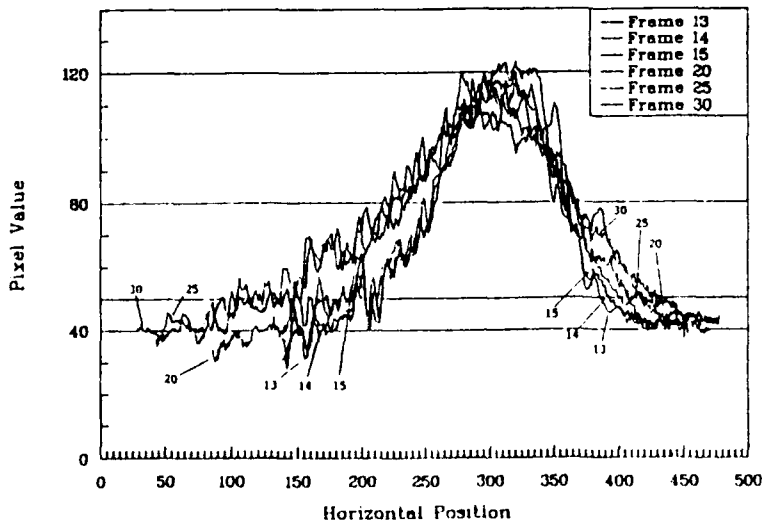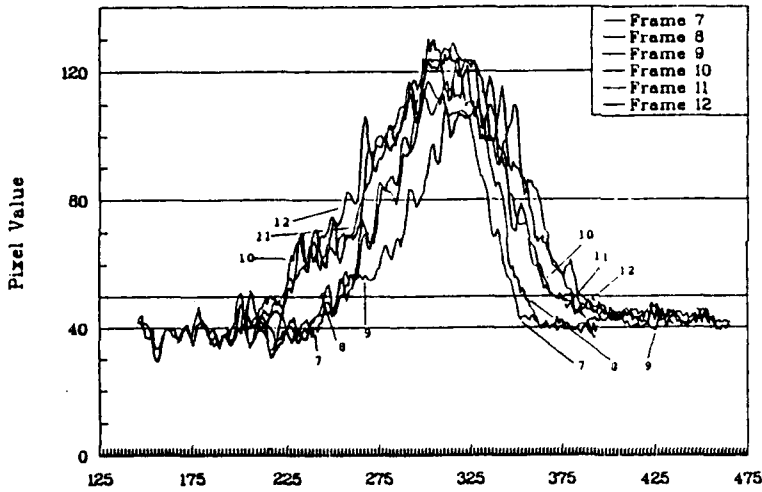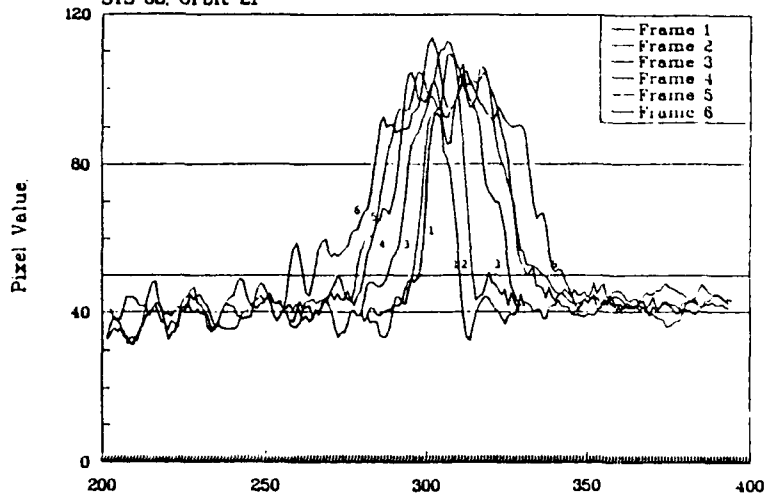
Figure 43.

Horizontal profiles through
the area of maximum width
of STS-33 Perpendicular
Upward Burn A. Note that
the pixel scales are different
in the three plots. 1 pixel =
7.14 m.

INTEGRATED PIXEL BRIGHTNESS
OF EXHAUST CLOUD
STS 33, PERPENDICULAR BURN (AWAY)
ORBIT 21
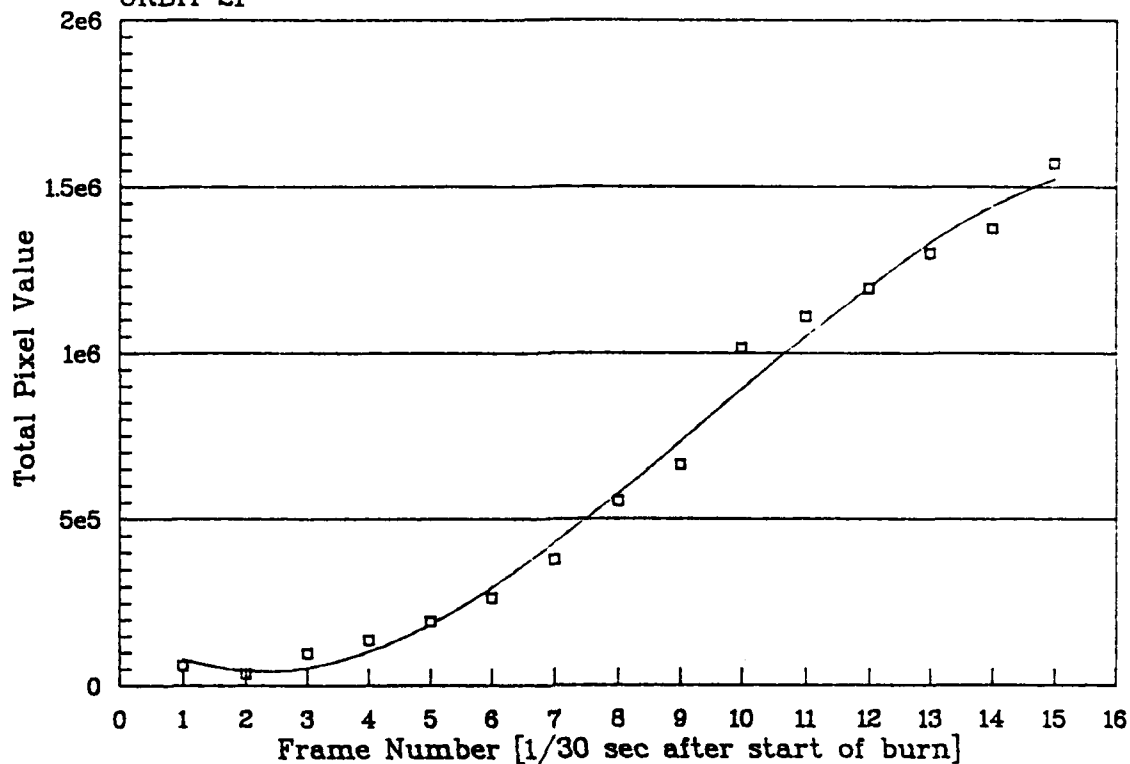
Figure 44.   Spatially-summed photocurrents above baseline from the exhaust interaction
volume of STS-33 Perpendicular Burn A. (See text for absolute calibration.)

on this point; recall that the axes of paired thrusters are typically separated by 40°); the lower such finger persists considerably longer than the other. Burn C in contrast appears to show a single maximum, with a regularly-repetitive structure having mean wavelength 70 m (corrected for the non-normal view projection) most apparent in video frame 6. (If the directed velocity of the exhaust gas responsible for this luminosity is taken as the nominal 3½ km/s, the period of this wave would be 20 ms.)

This component of the visible emission may be associated with the highly-reactive incompletely-combusted monomethyl hydrazine fuel of engine startup transients. MMH and its fragments have high cross-sections for excitative reaction with the depleted (by the gas flow) atmospheric oxygen atoms; the enhancement is not symmetric, as would be expected if the near-parallel thrusters do not have exactly the same performance characteristics; and the enhancement soon falls below threshold. Additionally, the wavelike structure may stem from a mechanical resonance in the PRCS thruster engine(s) operated in Ram Burn C.

PV Col | 0-7 | 8-15 | 16-23 | 24-31 | 32-39 | 40-47 | 48-55 | 56-63 | 64-71 | 72-79 | 80-87 | 88-95 | 96-103 | 104-111 | 112-119 | 120-127
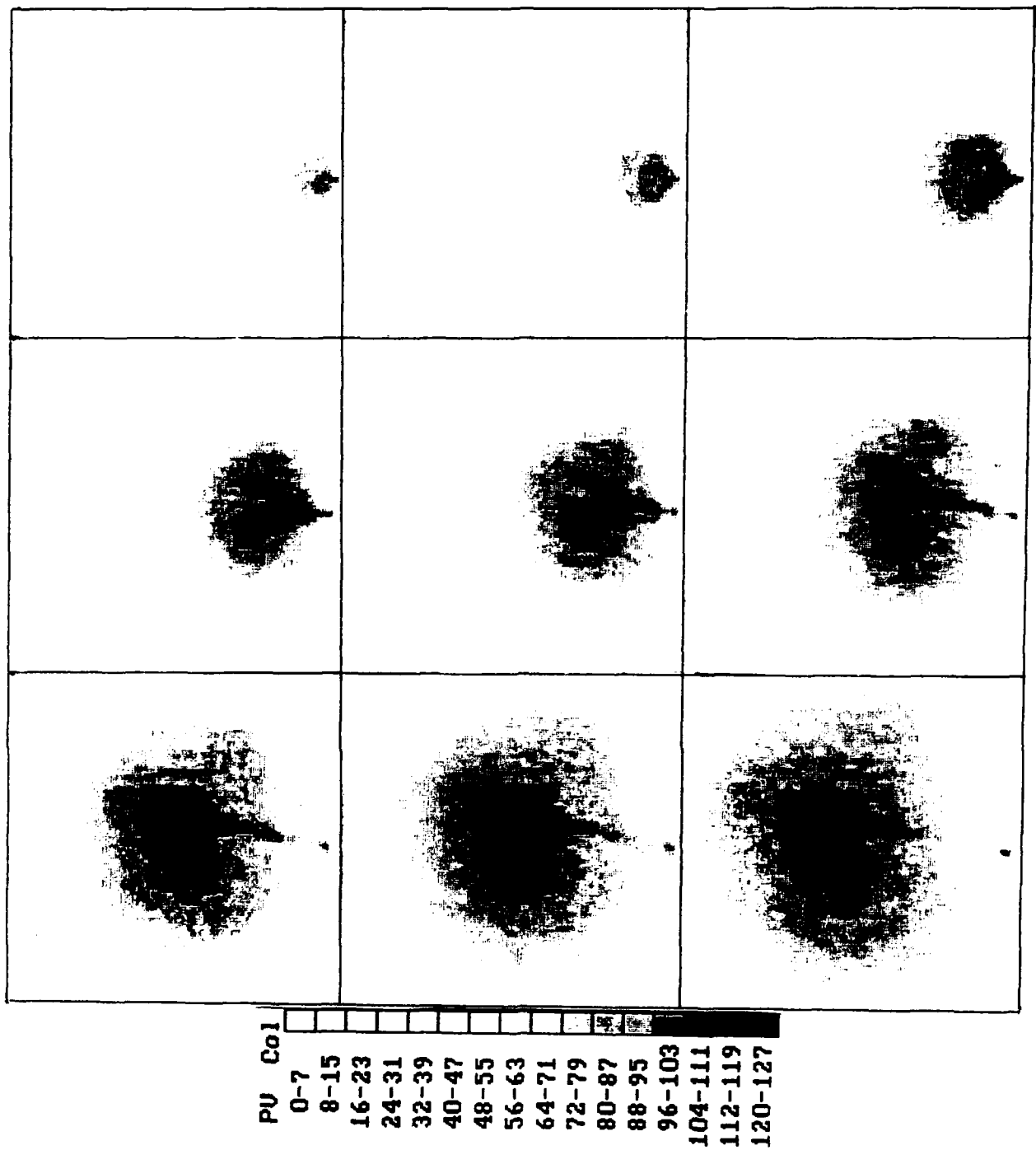
Figure 45.   Enlargement of the first 9 frames of STS-33 Ram Burn A, showing the initial luminosity extending from two PRCS engines.   The horizontal and vertical distance scales of the frames are 1.3 and 1.1 km.   (See Figure 23.)

52
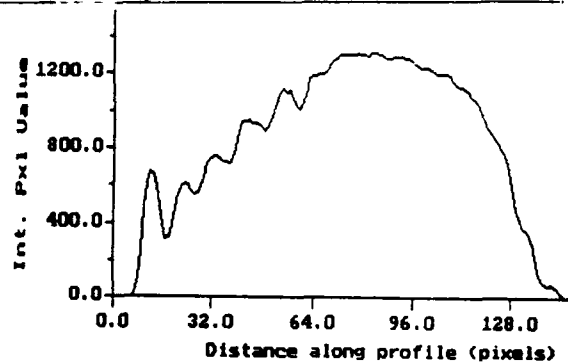
Figure 46.   Enlargement of Frames 2-7 of STS-33 Ram Burn C.   The horizontal and vertical distance scales are 0.8 km and 0.7 km.   The sum of five adjoining photocurrent traces at lower right is through the area of Frame 7 image that contains Shuttle Orbiter.

A similar phenomenon, also evident in the STS-29 firing (see Fig. 17), takes place when the rocket thruster engines turn off. The afterpulse expands outward while the side of the main luminous volume toward the spacecraft erodes (as no further exhaust gas is arriving), leaving a dark ring between the two radiating areas. Figure 47a illustrates this minimum in Frame 115 after engine turnon, which is 0.8 s after turnoff. We determined the phase velocity of this outward-expanding dark region from measurements of the photocurrents along the line

63
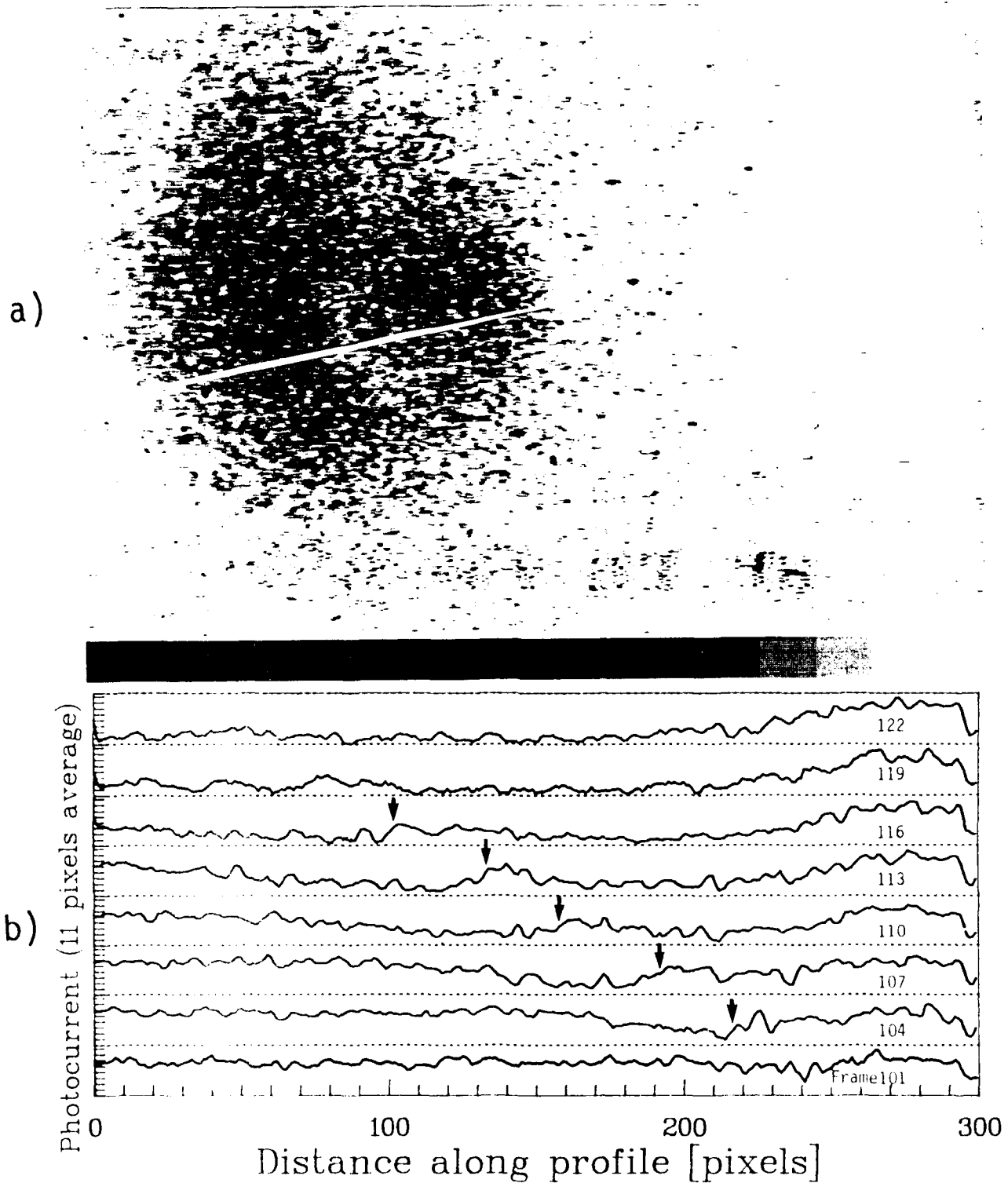
Figure 47.   a) Image of an engine shutoff wave, produced by subtracting an average of 16 pre-shutoff frames from the frame. Profiles through the exhaust interaction volume cloud along the line shown in a) which intercepts the spacecraft are plotted in b) for every third frame after the thrusters turn off (time increasing vertically, distance from Orbiter increasing to the left). The velocity of the minimum stated in the text was derived from the points indicated by arrows.

through the spacecraft shown (pixels from 11 adjoining parallel scans were coadded to reduce noise), defining the measurement point as the beginning of the steep incline in the trailing edge of the minimum; refer to Fig. 47b. Between Frames 110 and 122 this velocity was essentially constant at 2.3 km/s. This figure is in effect the rate of advance of the apparent edge of the luminosity from the combustion-exhaust interaction in the frame of reference of the spacecraft (which moves 3 km during this period).

Yields of Optical Radiation

Figures 48-51 compare the spatially-summed photocurrents from PRCS thruster firings toward the three directions and between similarly-directed firings, and Table 6 summarizes the maximum yields in the S-20R spectral band from the exhaust-interaction volumes derived to date. A comparison among absolute yield rates from the three series of STS-33 experiments would require further calibrations of the AMOS cameras against star fields, insofar as the calibrations described in Section 3 refer only to Burns C (with the further assumption that the electronic gain of the AATS camera does not change during the -27 s of data); these took place the night after Burns A and B, which themselves were separated by one orbit or 94 min. The uncertainties associated with the calibration procedure and the gain of the two types of groundbased camera lead to an estimated potential error of $\pm$ a factor 2 in the absolute yield rates from within this field of view, a somewhat larger error in the maximum surface radiances listed in Table 6, and substantially more error in the AATS 0.5°-field data (on which more in the discussion of Table 6). Further uncertainty in the correction for the chemiluminescence that originates from outside the field of this camera leads to a still larger potential error in the total sterances.

Figure 48 compares the integrated pixel values from the two STS-33 ram burns analyzed. The congruence of the two "irradiance" plots is more or less coincidental, as Ram Burn C is both -20% closer to AMOS and at a lower zenith angle (so that the air mass along the sight path is somewhat smaller); it also extends beyond the camera's field of view earlier in the thruster firing, as its tracking caused Shuttle Orbiter to lie closer to the edge of this field. The upward curvature of the relative yields in the first -½ s after thruster turnon is most probably due to the more rapid than linear increase of the number of atmospheric oxygen atoms encountered by the diverging exhaust gas steam, that is, to the decrease in average depletion of this reactant as the flux (or fluence) of combustion-product molecules decreases.

No such effect is evident in Wake Burn A (Fig. 49), the sterance from which may actually be evidencing a small downward curvature. The optical yield from the ram-directed firing that took place a few s earlier increases much more rapidly, so that the ratio of yield rates reaches a factor almost 60 by ½ s.

65
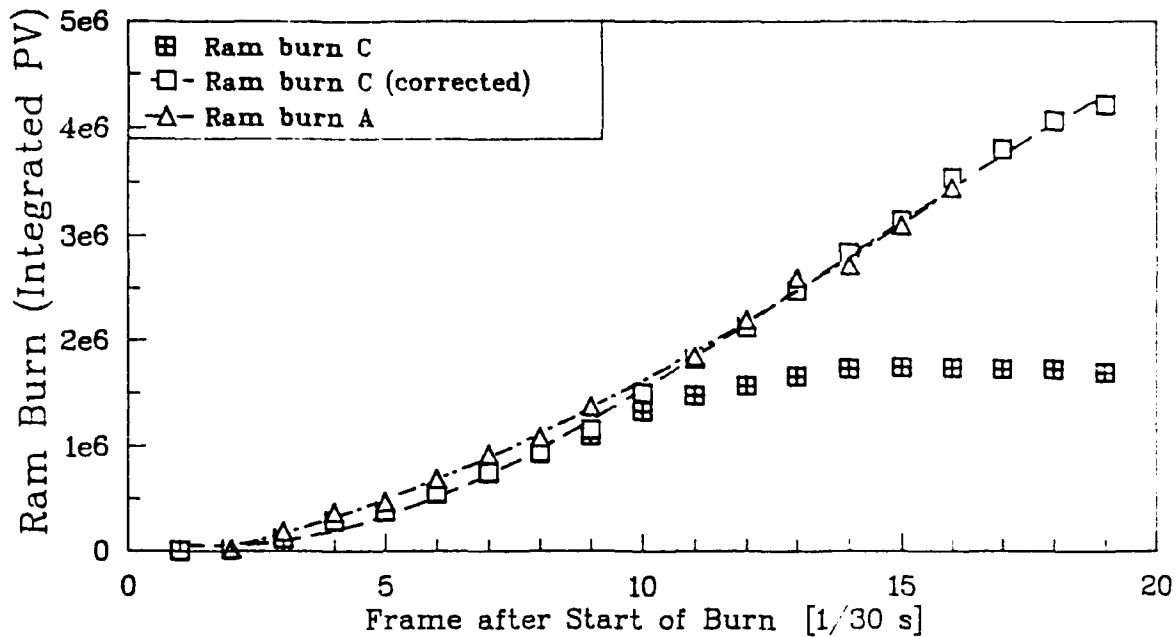
Figure 48. Comparison of the total integrated pixel values during the first 2/3 s of the two ram burns analyzed. The correction for the segment of Ram Burn C outside of the AATS camera's field of view was based on a spherically-symmetric Gaussian distribution of radiance. The ratio of ranges to AMOS from the two firings is 531 km (A):424 km (C) and the atmosphere transmissions are about the same.
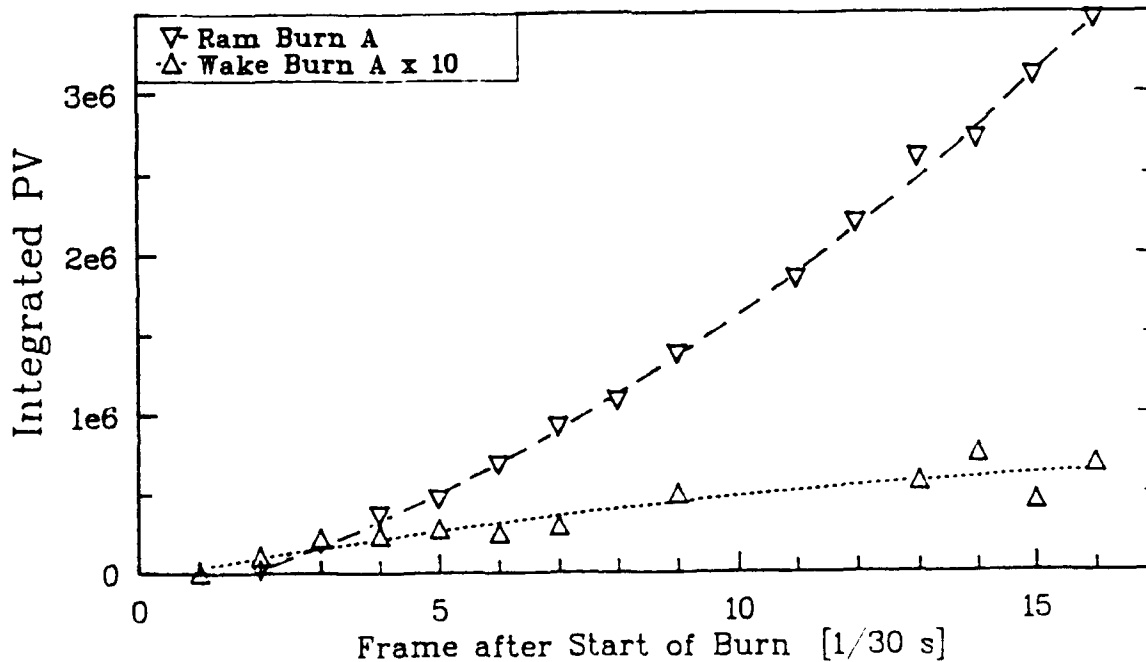
Figure 49. Comparison of the first ½ s of Ram and Wake Burns A. The wake interaction volume has expanded out of the field of view by frame 15, at which time the ratio of sterances is about 60.
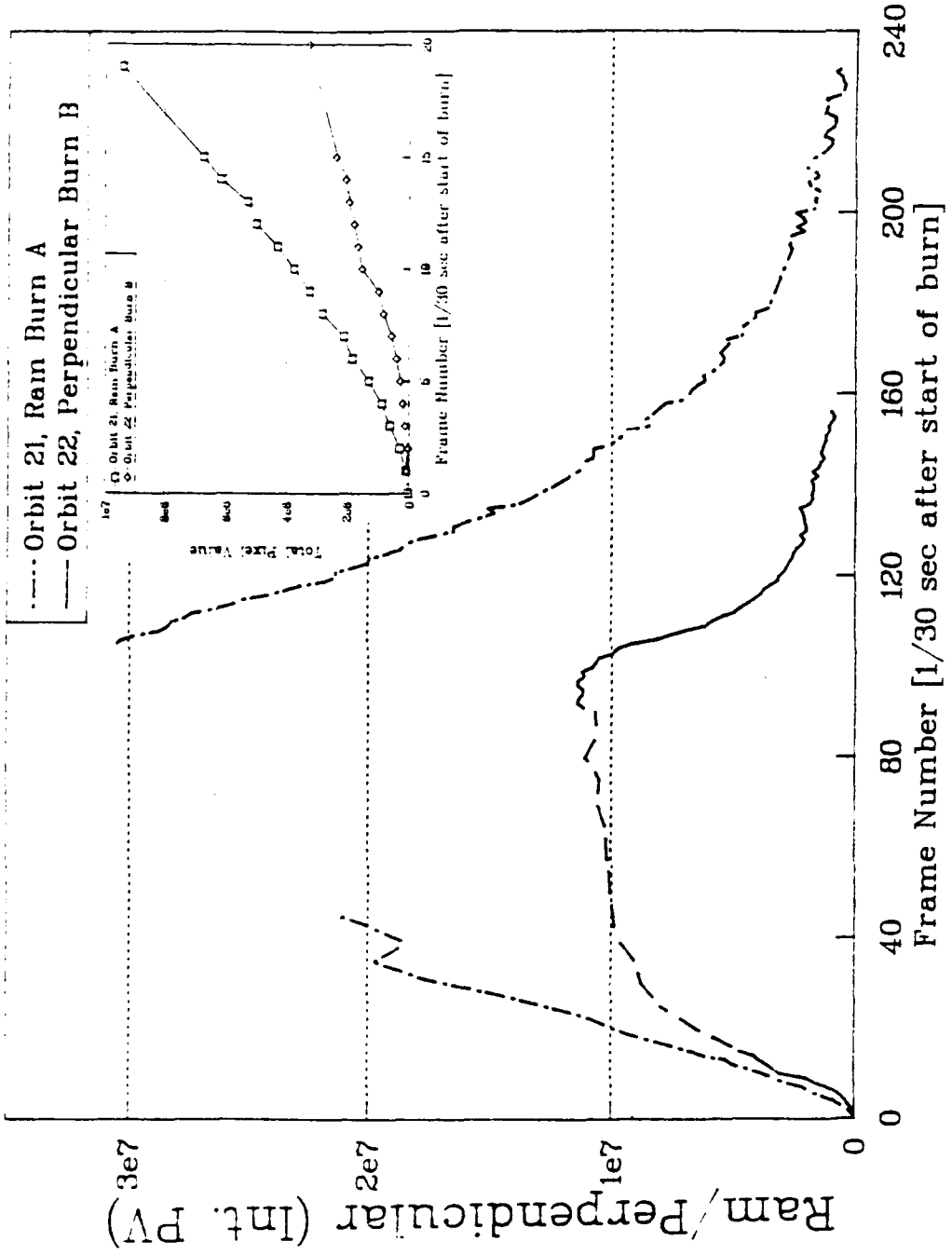
Figure 50. Comparison of Ram Burn A and Perpendicular Upward Burn B. The dashed portion of the perpendicular firing connects the period in which the interaction volume has extended beyond the field of view (see Figure 25); no correction was made to the total sterance because (unlike the ram volume) the radiance distribution from the perpendicular burns does not fit an extrapolable shape. The inset is a comparison of the first 2/3 s of the two burns.
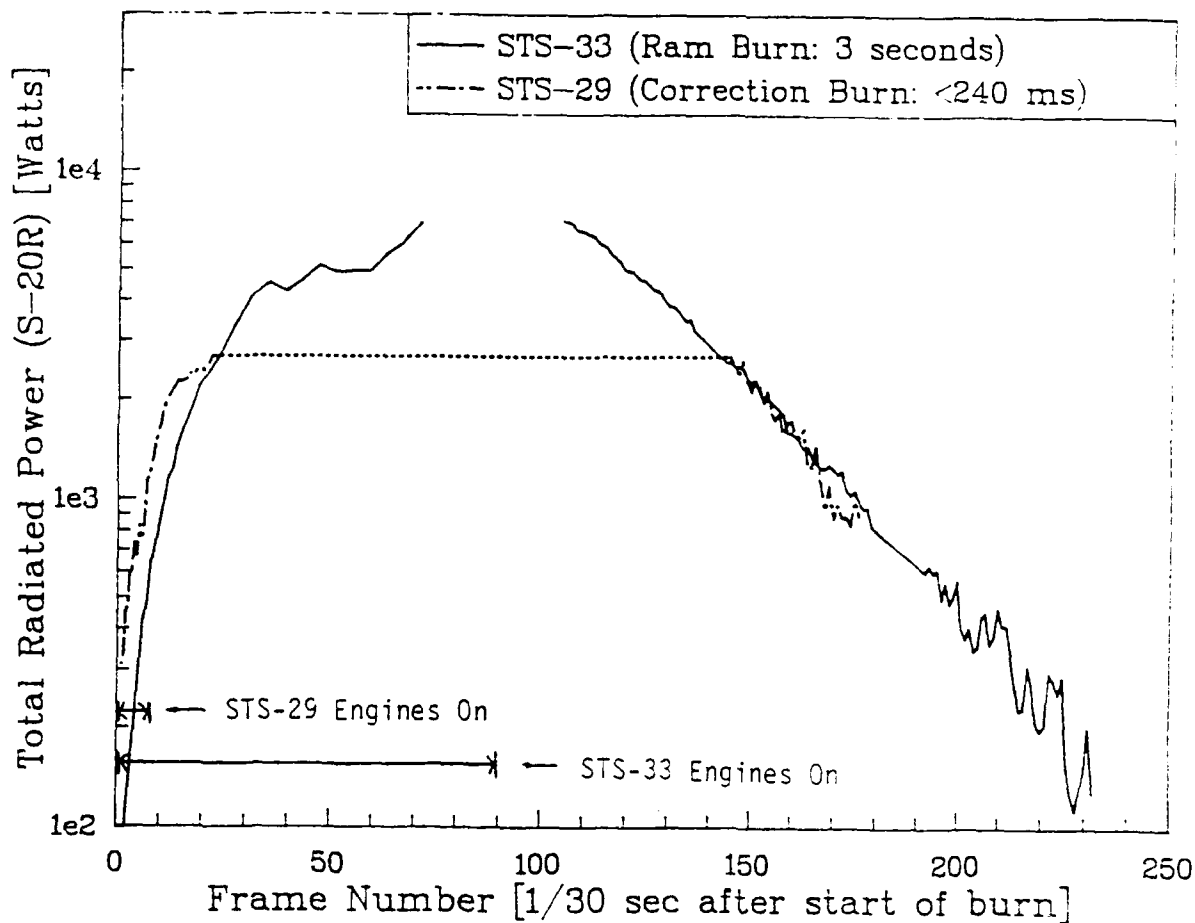
Figure 51.   Comparison of the total radiated power from the STS-29 ram-hemisphere burn
and STS-33 Ram Burn A. The maximum of the STS-33 burn was taken from
the GEODSS calibration.

Figure 50 compares sterances from Ram Burn A with those from the perpendicular-upward firing of experiment series B.   The spatially-summed photocurrents from the ram exhaust interaction volume are roughly four times these from the perpendicular-directed firing during the two time periods plotted, in large part because the spacecraft was substantially closer (see Table 1 and Fig. 22). The perpendicular burn shows a somewhat slower rise with some upward curvature (perhaps and artifact of the correction for the out-of-field luminosity), and about the same fractional rate of decrease. Comparison of the absolute optical yields from these two burns is subject to substantial error because of the uncertainty in the fractions of the total radiating volumes that lie outside the AATS camera's field of view.

Figure 51 illustrates the similarity between the sterances of STS-33 Ram Burn A and the unscheduled, much shorter-duration STS-29 firing at the angles to the trajectory in the ram hemisphere presented near the beginning of this Section. The rise times are about the same,

and the absolute values appear to be within a factor 2 in the first ½ s. (The absolute optical power output from the STS-33 exhaust interaction volume was derived using the GEODSS calibration, as mentioned in the caption of Fig. 51; and the decay segment of the shorter-duration burn is arbitrarily fit to the longer burn.) As the decrease of the STS-33 luminosity after turnoff refers to the small segment of AATS 0.5° camera field stated in the caption of Fig. 40, it is not directly comparable with the decrease in total sterance of the STS-29 luminosity confined to within the AATS 3° camera field. Nonetheless the similarity of "shapes" of the two sterance plots--from ram-directed and largely perpendicular-directed firings--indicates the essential stationarity of the initial increase and eventual falloff of optical yields from thruster firings with a wide range of total durations and over a modestly wide range of exhaust axis directions relative to the trajectory.

While the absolute values of optical yields from the fully-developed exhaust-interaction volumes in Table 6 show considerable variability, the ratios of total emission rates are expected to be reasonably reliable. The figures refer to a radiation source that is spectrally flat between 3000Å and 9000Å. If the actual emission spectrum of the luminosity were that of 6500K or 3000K black bodies, the optical yields over this spectral range would be 15% lower and 33% higher respectively. These "corrections" are of course well within the systematic error of the reduced data in Table 6.

The maximum total ram-burn power derived with the help of the more reliable GEODSS calibration is ~8 x 10^3 watts, or somewhat less than 10^{-3} of the total kinetic energy of the exhaust gas from two PRCS thruster engines. The similar value based on the AATS 0.5°-field calibration against the streaked image of the single star in Fig. 15 is so much lower that the possibility of some systematic error in our standardization procedure must be considered. In view of the internal consistency of the GEODSS calibration against 18 known stars in Fig. 8, and the reasonable agreement with the optical yield from the thruster firings at 67° from ram in the STS-29--33° AATS measurement, we give credence to the higher optical yield rate.

This latter maximum yield, measured with a reasonably reliable calibration (the images of each of ~20 stars are confined to less than 1/150 of the width of the video camera's field), is 1/3 that of the ram luminosity inferred from the GEODSS auxiliary camera data. In view of the aforementioned large angle to Orbiter's trajectory of the axes of the two "D" thruster engines, this figure can be considered in good agreement with the STS-33 perpendicular/ram yield rate ratio derived from the GEODSS data. Similarly the perpendicular/wake yield ratios [again, at maximum development of the exhaust interaction] from GEODSS--with the assumption that the gain of this camera remained constant--are in satisfactory agreement with those measured in experiment series A by the AATS 0.5° field camera.

Table 6. Maximum Yields of Radiation from PRCS Thruster Exhaust-Interaction Volumes

MISSION Day/UT (PRCS)	SENSOR, FOV (Calibration)	MAXIMUM TOTAL POWER [Watts] S-20R*			MAXIMUM SURFACE BRIGHTNESS [kR] S-20R		
		Ram	Perpendicular	Wake	Ram	Perpendicular	Wake
STS-29 076/15:34 1989 (3 engines)	MOTIF-AATS 3° (Fair)	—	2700	Below Threshold	—	300	Below Threshold
STS-33 329/07:51 1989 (2 engines)	MOTIF-AATS 0.5° (Poor)	>170	>90 ~Sequence C-	15	—	Single-Star Calibration (see text)	—
	AATS relative GEODSS absolute	8500**	—	230**			
STS-33 329/07:51 1989 (2 engines)	GEODSS 6.0° (Good)	7000 inferred from AATS	3400 (Up)† 7900 (Down)†	690	—	1700 (Up)§ 5100 (Down)§	140
STS-41 280/03:20 1990 (2 engines)	AI/S on AATS 12 0.50-km pixels, 1-D imaging Spectrograph (Very good, performed in the laboratory)				>>100 (Spatial average, sum over spectrum)	—	Below Threshold
STS-38 321/07:24 1990 (2 engines)	AI/S on AATS Higher resolution spectra at two regions of interest near 3360Å and 6300Å			Data not yet reduced			

* Divide by 4π to derive sterances 3000-9000Å.
** Transfer of GEODSS calibration to AATS through frame 14 of Wake Burn C to derive Ram Burn C maximum total power.
† Corrected for saturation, uncorrected for sterance of the rocket engine; assumes same sensitivity in experiments A and B as C.
§ Interpolation from isophote contours, uncorrected for radiation from the rocket engine.

The maximum radiances of the fully-developed exhaust-interaction volume are of the order of one megarayleigh (neglecting the apparently-faulted AATS 0.5° field images). These peak surface brightnesses in Table 6 are subject not only to the aforementioned errors in photometry, but also to the further uncertainty inherent in converting irradiances from known stars to radiances of extended objects. The brightnesses derived from the GD/Arizona spectrograph are lower limits to the maxima, as they refer to some average over the several imaging channels.

SECTION 4

EMISSION SPECTRA OF THE EXHAUST-INTERACTION VOLUMES

Introduction

Space- and time-resolved spectra of the luminosity from ram and perpendicular-to-track PRCS firings from STS-41 and STS-38 were obtained with the one dimensional imaging instrument described in Section 2. (The spectral radiances from the air in which wake-directed exhaust gas reacted were below this sensor's threshold.) The original -0.8 s-duration traces such as appear in Fig. 4 (the conditions of which appear in its caption) were coadded in space and time to produce composite spectra with improved signal/noise ratios, such as are illustrated in Fig. 52.

These recently-obtained spectrum data are still preliminary, as they have been only partially reduced by the Lunar and Planetary Laboratory, the averaging-weighting procedures and the corrections for extinction by the atmosphere and--in particular--background from the moonlit sky are undocumented, and the relative numbers of counts contributed to the composite results from the several image fields and times after thruster turn-on are not specified. In consequence this new information is reviewed only briefly here, for the limited purposes of provisionally identifying the radiating species toward validating the ideas presented in Section 1 about how they are excited, and of providing guidance for interpreting the wide spectral range ("visible light") images of the exhaust interaction volumes in Section 3.

Emission Features

Figures 52a and b are composite spectra from the ram- and upward perpendicular-directed PRCS exhaust of the 290-km altitude STS-41 experiment, annotated (by the Lunar and Planetary Laboratory) with approximate mean radiances of the principal features. (The scattered radiation from the atmosphere illuminated by the 91%-full moon at 83° el, 300° az-- in the backward hemisphere, 27° from the ram exhaust volume--has been subtracted.) The el-az and range of the spacecraft during the two firings appear in the caption. As its trajectory took it almost directly over AMOS, its azimuth angle stays about constant, and in the ram firing the line of sight makes an angle of 67° (= arc cos 0.92) with the exhaust axis. The free spectral range of the instrument was decreased for the measurement of the perpendicular-to-track exhaust interaction to improve identification of the emission peaks at the longer wavelengths, which would include the hydroxyl vibrational bands predicted (in Ref's 3 and 4) to make a major contribution to the luminosities measured by the AMOS video cameras.
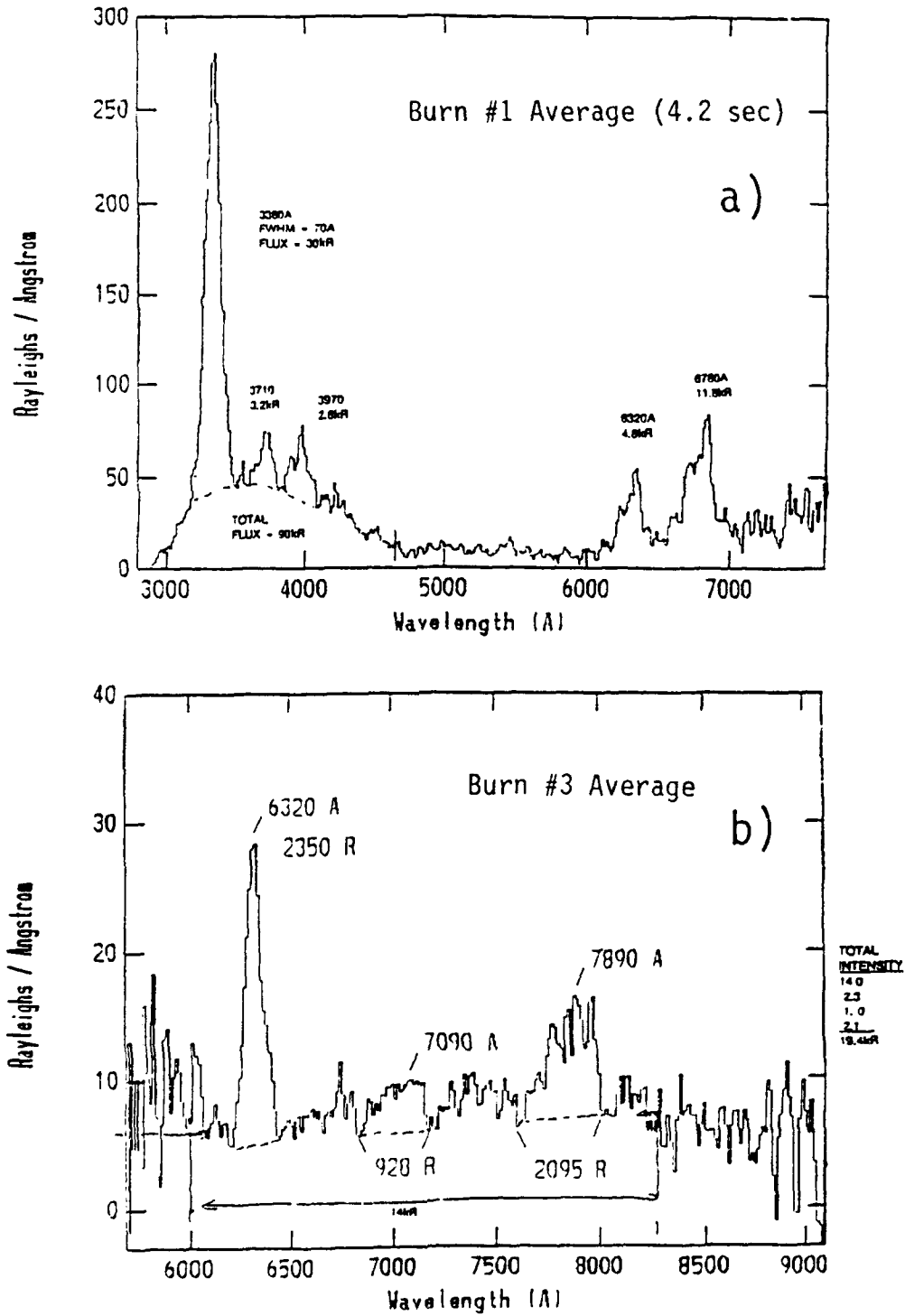
Figure 52. Space- and time-averaged ram (a; see Figure 4) and perpendicular-to-orbital track (b) emission spectra from STS-41. The spacecraft is at 290 km altitude, and its el-az angles and ranges are 67°-66°, 314 km and 50°-68°, 375 km respectively.

Table 7 lists the features provisionally identified in these (and other) initial processings of the data from the imaging spectrograph. The highest contrast feature at wavelengths below ~8500Å that are transmitted by the atmosphere is centered at 3365Å. A banded region with what appears to be an underlying continuum then extends to almost 5000Å, longward of which a narrow peak (in view of the instrument resolution) is prominent near 6320Å. Broader maximums that may be the expected hydroxyl emission (only the $\Delta v \geq 4$ sequences lie within the sensor's spectral range; see later Fig. 54) are present near 6700, 7000, and 7900Å. Synthetic spectra of the vibrational cascade of OH ($X^2\Pi$) (compiled by the Lunar and Planetary Laboratory, unpublished) lend some credence to this identification.

The strong narrow band at 3365Å can be confidently identified as due to NH radicals, some other observations on and properties of which are stated in Table 8. The ultraviolet NH ($A^3\Pi \to X^3\Sigma$) bands are well known to be prominent in the decomposition of hydrazine compounds in flames and electric discharges, and--in particular--when monomethyl hydrazine is heated in an oxygen atmosphere (Ref 18). In consequence this emission can be ascribed to a reaction with the orbital atmosphere of uncombusted thruster fuel or one or more of its fragment species. A very rough estimate of the total yield of NH($A \to X$) radiation from the ram firing, made by scaling the spectral intensities and referencing to the total yields of visible light measured by the video cameras (at STS-33; see Table 6), is 10^3 watts. (This estimate assumes that the spatial distribution at 3365Å is the same as that of the images, as is in fact suggested by Fig. 53.) This power output would result from a production rate of ~2×10^{21} NH(A) radicals/s (all depopulating by radiation, as collisional quenching is negligible); and since the PRCS engines consume about 10^{25} MMH molecules/s, chemiluminous reactions of a few hundredths percent of this thruster rocket fuel would produce the observed radiation from electronically excited NH.

As for spectral identification, the shape of this 3365Å-centered feature is satisfactorily fit by a blend of the Q branches of the (0,0), and (1,1) $A \to X$ bands of NH at vibrational temperatures of order 2000K, and furthermore the relative count rate in the broader spectrum peak near 3650Å in Fig. 52a is consistent with the branching ratios for the (0,1) and (1,2) transitions. The appearance of some 3365Å emission in the spectral "image" of the wake as well as the ram direction (refer to Fig. 53), should this be a real effect rather than due to offset of the spectrograph's field of regard, may provide information about the excitation mechanism (as discussed below).

The spectral resolution is so far inadequate for reliable identification of several close-lying features to the red of these NH bands. Candidate radiating species, whose excitation is also discussed below, include CO-CO_2 (the flame-bands combination of peaks and quasicontinuum extending between 3500 and 5000Å) and the other carbon atom-continuing

74

Table 7.   Preliminary Ideas on Excitation of the Near UV-Visible Exhaust-Interaction Radiations

FEATURE	PROBABLE REACTION	IMPLICATION/EXPERIMENT
3365 and 3650 Å	Unidentified	Comparable UV emission in NO γ, OH A $\rightarrow$ X, other bands
-4000 - 5000Å (overlapping molecular bands, or continuum)	Transfer of excitation to radicals present at low concentrations in the exhaust volume; CO + O	Measure concentrations of metastable species [such as N_2 (A)] in laboratory engine exhaust
6300 and 6364Å	$H_2O + O^+ \rightarrow$ $O(^1D) + H_2O^+$ $\hookrightarrow O(^3P)$ red doublet	Yield independent of H_2O exhaust rate, depends on (naturally - variable) ionospheric [O^+]
	H_2O or $N_2 + O^3(P) \rightarrow$ H_2O or $N_2 + O(^1D)$	Excitation transfer from $O(^1D)$ leads to further radiations
6200 - 7800Å	$H_2O + O \rightarrow$ $OH(X, v=0 - 7) + OH$ $\hookrightarrow$ "Meinel" Vibrational bands	2 to 3 orders of magnitude more NIR - SWIR photons emitted than in the S-20R spectral range
		$\rightarrow OH(A, v=0 - 3)$ as in the laboratory $\hookrightarrow$ 3064Å, other UV bands

75

Table 8.   Summary of Observations on Excitation of NH

NH(A → X) is a persisting emission in the decomposition of hydrazine ($H_2N\text{-}NH_2$) compounds in flames, discharges,...

1)   The *spectral shape* of the feature near 3365Å closely resembles a blend of the NH(A → X) 0, 0 and 1, 1 Q branches.

2)   The *position and relative intensity* [to 3365 Å] of the spectrum feature near 3650Å are consistent with the 0, 1 and 1, 2 bands of NH.

3a) PRCS *engine fuel* is MonoMethylHydrazine ($H_2N\text{-}NHCH_3$). Steady burning consumes ~6 x 10^{24} MMH/s.

3b) The total observed *yield* of about 10^3 watts at 3365Å corresponds to a production rate of ~2 x 10^{21} NH(A)/s.

4)   NH(A → X) radiation may arise from the *wake* as well as the forward hemisphere during ram engine burns.

5)   Population of the NH (A) state leads also to emission of ~1 *vibrational photon* at 3.1 μm (direct excitation of NH† by chemical reactions would also be expected).

---

6)   The ~1/2 μs radiative lifetime of NH(A) suggests that the radiation is due to

  • a) *excitation* of NH(X) by a longlived precursor,   or
  • b) *chemiluminescence* of an N_mH_n-containing exhaust product--including MMH (in droplets also).

7)   In laboratory experiments (Ref 18)
     MMH (heated with O_2)   → NH* , OH* , NH$_2^*$, NO* and
                                    $N_2(A)$ (2 s radiative lifetime, 6 eV internal energy)
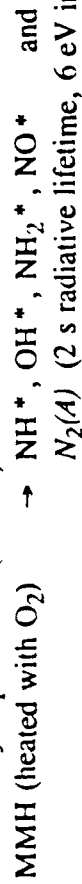
Interpretation: - - $N_2(A)$ + exhaust NH(X) → NH(A) + $N_2(X)$

Consequence: - - Excitation can also be transferred from $N_2(A)$ to these other molecular fragments, as well as CN, CH, C_2,...

76

a)

b)
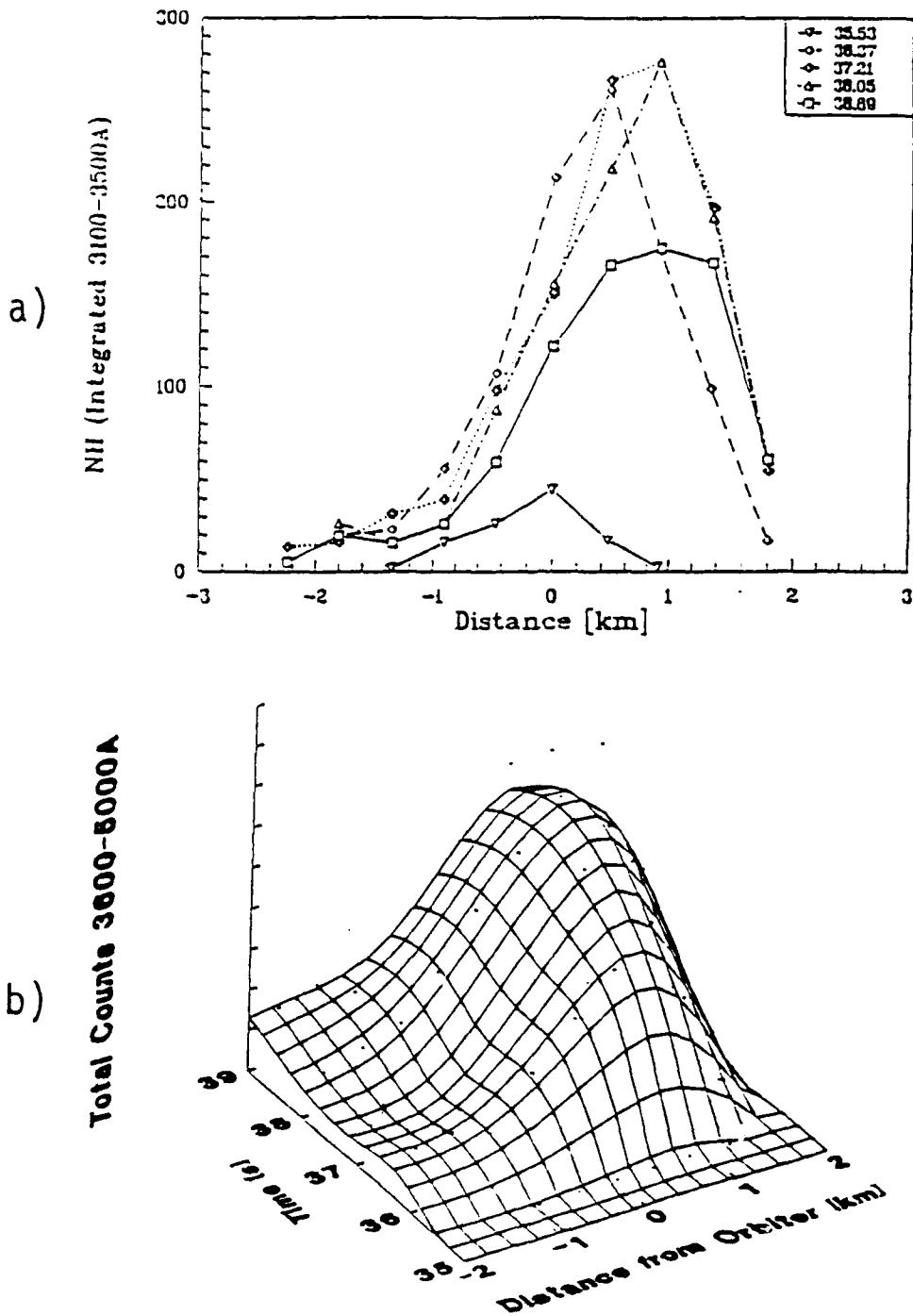
Figure 53.   a) Integration over the spectrum range 3100-3500Å of the data shown in Fig. 4, which are dominated by the NH Q branches. The profile position relative to the exhaust interaction volume is indicated in Figure 3. b) Similar profiles for the 3600-5000Å region of the spectrum with Orbiter nominally at 0 km.

molecules listed in Tables 7 and 9. Some of this emission also appears in the reportedly wake-viewing spectrograph channels; again, refer to Fig. 53.

The spectrally relatively narrow peak near 6320Å has been tentatively identified as the forbidden atomic oxygen ($^1D \rightarrow {}^3P$) doublet at 6300 (¾ of the photons) and 6364Å (¼). (Recall that the nominal resolution of the instrument is 70-80Å.)

Interpretation -- UV and Blue Features

Table 9 presents our preliminary interpretation of these spectrum features, with its implications for emission at other wavelengths and ideas for further PRCS-firing experiments.

Some 3365Å radiation appears in Orbiter's wake in the imaging spectra (see Fig. 53). If this is a real physical effect (rather than due to mispointing of the instrument), since the ~10^{-6} s radiative lifetime of NH ($A^3\Pi$) is extremely short compared with molecule times-of-flight this state must be populated either by excitation-transferring collisions of NH ($X^3\Sigma$) with a longlived precursor or by a chemiluminescent reaction with ambient O of some N_mH_n-containing exhaust species. The latter could be intact MMH--even in droplets, which very rapidly evaporate in the near-vacuum of low earth orbit. A similar process would then also explain the longer-wavelength emissions that also appear to arise from the region behind the spacecraft.

While the journal literature contains numerous references to electronic excitation of NH in combustion (not only of amine compounds) and discharges--in ammonia gas, for example--little information is available on the underlying chemical mechanisms. In the previously-mentioned laboratory experiments involving heating of MMH in O_2, electronic bands of NH_2 (widely spread through the visible), OH ((A $\rightarrow$ X) near 3000Å), and NO (near-ultraviolet γ (A $\rightarrow$ X)) were also observed; this phenomenon was interpreted as due to excitation transfer to these species from long-lived (2-s radiative lifetime) N_2 ($A^3\Sigma^+$) molecules. The 6 eV internal energy of N_2(A) is sufficient to excite also electronic bands of CN (B $\rightarrow$ A; the violet system, extending to 4500Å), CH (A $\rightarrow$ X; "4300Å" system, with some emission to 4900Å), and C_2 (A $\rightarrow$ X; the Swan bands persistent in shocked air, extending over almost the whole visible spectrum). However, at chemical equilibrium the concentration of purported-precursor N_2(A) in the 3000K (¼-eV temperature) thruster exhaust gas would be extremely small. (If N_2(A) is indeed the precursor the largely-ultraviolet Vegard-Kaplan (A $\rightarrow$ X) bands would be weak, as the sequence is spread over many individual transitions and is principally at wavelengths almost completely absorbed by the atmosphere's ozone molecules.)

The broad ultraviolet-blue feature in Fig. 52a is consistent with the carbon monoxide flame spectrum, which at low gas pressure shows the discrete bands enhanced over

78

Table 9. Features Provisionally Identified in the Spectra of Ram Exhaust-Interaction Glow

Wavelength	Location	Probable Transition	Lifetime	Current Question
3365Å (Narrow)	Ram and Wake	$NH(A^3\Pi \rightarrow X^3\Sigma)$ 0,0 and 1,1 Q Branch	0.5 μs	Excitation source
3650Å (Band-like)	Ram (and Wake?)	$NH (A \rightarrow X)$ 0,1 and 1,2	~1.5 μs	Excitation source
~4000Å (Band-like)	Ram	?		Identification
4000-5000Å (Many bands overlapping)	Ram	$CO-CO_2$ flame, C_2, CN, CH, N_2(V-K), $N_2(2^+)$,...		Identification
6200, 6500-6800, 7000, 7800Å (Band-like)	Ram	$OH(X^2\Pi, \Delta v = 4$ and 5) "Meinel" bands	< 10 ms (Upper state) ~1 s (For transition)	
6300 and 6364Å	Ram (and Wake?)	$O (^1D \rightarrow {}^3P)$ doublet	200 s unquenched	$H_2O + O \rightarrow 2OH$ --IR implications-- Neutral or ion process (or both); dependence on c.m. KE; excitation transfer upon quenching

the accompanying continuum. This radiation is observed when CO burns in air or an oxygen atmosphere. Its continuum component (at least) has been associated with the recombination of CO with O atoms.

Interpretation -- Oxygen Red Doublet

The upper state of the OI forbidden red lines lies 1.97 eV above the ground electronic state, the endothermicity of charge transfer from O^+ to H_2O is only 0.96 eV, and the c.m. translational energy of O^+ - H_2O available in ram or perpendicular firings is ~5 eV. Consequently some of the population of this state could be by charge-transferring collisions, as is discussed in Table 10. However the natural concentrations of O^+ are so low that even if all the ions in the interaction volume observed by the AMOS cameras transfer their charge to H_2O, leaving all the resulting neutral O atoms in the metastable (200-s radiative lifetime) ^1D state, this process could not be dominant. The yield of the component of the 6320Å emission that arises from this charge exchange varies with the ionospheric plasma density; it would therefore depend on the elevation angle of the sun ($[O^+]$ increases by a factor ~5 near dawn, for example), and also change with season, latitude, and phase of the solar cycle, which also determine the fluxes of ultraviolet solar photons that ionize oxygen atoms.

$O(^1D)$ may also be excited by nonadiabatic collisions of neutral oxygen atoms with exhaust N_2 or H_2O (or the somewhat less abundant CO and CO_2, or even high velocity O in the gas flow), that is, by Type 2) processes. As mentioned in Section 1, the cross-sections for these excitative reactions with the initially high-energy and moderated (by elastic collisions) combustion-product molecules have not been directly measured, and furthermore the theoretical treatments (for example Ref's 23-24) are both incomplete and in only partial agreement. (Estimates of these cross-sections from the rate coefficients for the reverse reactions at typically 300 K--collisional quenching of $O(^1D)$--are subject to uncertainty from the very limited information available about the distributions of energy disposal in these depopulations of the excited state.)

The disappearance of this 6320Å feature in the spectrums after the PRCS shuts off indicates that the lifetime of $O(^1D)$ atoms in this instrument's narrow field(s) is less than about 1 s. This finding is qualitatively corroborated by the video images and the sterances derived from them, which evidence no persisting luminosity such as would result from this (actually relatively weak) component of the total visible-light signal. Thus the fractional rate of decrease of column density of $O(^1D)$ in the regions of these images that are above the AATS and GEODSS camera thresholds also exceeds 1 per second.

This rapid falloff in the number of excited atoms per unit projected area is due to a combination of their collisional depopulation and outward diffusion. Table 11 lists the rate

80

Table 9. Features Provisionally Identified in the Spectra of Ram Exhaust-Interaction Glow

<u>Wavelength</u>	<u>Location</u>	<u>Probable Transition</u>	<u>Lifetime</u>	<u>Current Question</u>
3365Å (Narrow)	Ram and Wake	$NH(A^3\Pi \rightarrow X^3\Sigma)$ 0,0 and 1,1 Q Branch	0.5 μs	Excitation source
3650Å (Band-like)	Ram (and Wake?)	$NH (A \rightarrow X)$ 0,1 and 1,2	~1.5 μs	Excitation source
~4000Å (Band-like)	Ram	?		Identification
4000-5000Å (Many bands overlapping)	Ram	$CO-CO_2$ flame, C_2, CN, CH, N_2(V-K), $N_2(2^+)$,...		Identification
6200, 6500-6800, 7000, 7800Å (Band-like)	Ram	$OH(X^2\Pi, \Delta v = 4$ and 5) "Meinel" bands	< 10 ms (Upper state) ~1 s (For transition)	$H_2O + O \rightarrow 2OH$ --IR implications--
6300 and 6364Å	Ram (and Wake?)	$O (^1D \rightarrow {}^3P)$ doublet	200 s unquenched	Neutral or ion process (or both); dependence on c.m. KE; excitation transfer upon quenching

79

the accompanying continuum. This radiation is observed when CO burns in air or an oxygen atmosphere. Its continuum component (at least) has been associated with the recombination of CO with O atoms.

Interpretation -- Oxygen Red Doublet

The upper state of the OI forbidden red lines lies 1.97 eV above the ground electronic state, the endothermicity of charge transfer from O^+ to H_2O is only 0.96 eV, and the c.m. translational energy of O^+ - H_2O available in ram or perpendicular firings is ~5 eV. Consequently some of the population of this state could be by charge-transferring collisions, as is discussed in Table 10. However the natural concentrations of O^+ are so low that even if all the ions in the interaction volume observed by the AMOS cameras transfer their charge to H_2O, leaving all the resulting neutral O atoms in the metastable (200-s radiative lifetime) ^1D state, this process could not be dominant. The yield of the component of the 6320Å emission that arises from this charge exchange varies with the ionospheric plasma density; it would therefore depend on the elevation angle of the sun ($[O^+]$ increases by a factor ~5 near dawn, for example), and also change with season, latitude, and phase of the solar cycle, which also determine the fluxes of ultraviolet solar photons that ionize oxygen atoms.

$O(^1D)$ may also be excited by nonadiabatic collisions of neutral oxygen atoms with exhaust N_2 or H_2O (or the somewhat less abundant CO and CO_2, or even high velocity O in the gas flow), that is by Type 2) processes. As mentioned in Section 1, the cross-sections for these excitative reactions with the initially high-energy and moderated (by elastic collisions) combustion-product molecules have not been directly measured, and furthermore the theoretical treatments (for example Ref's 23-24) are both incomplete and in only partial agreement. (Estimates of these cross-sections from the rate coefficients for the reverse reactions at typically 300 K--collisional quenching of $O(^1D)$--are subject to uncertainty from the very limited information available about the distributions of energy disposal in these depopulations of the excited state.)

The disappearance of this 6320Å feature in the spectrums after the PRCS shuts off indicates that the lifetime of $O(^1D)$ atoms in this instrument's narrow field(s) is less than about 1 s. This finding is qualitatively corroborated by the video images and the sterances derived from them, which evidence no persisting luminosity such as would result from this (actually relatively weak) component of the total visible-light signal. Thus the fractional rate of decrease of column density of $O(^1D)$ in the regions of these images that are above the AATS and GEODSS camera thresholds also exceeds 1 per second.

This rapid falloff in the number of excited atoms per unit projected area is due to a combination of their collisional depopulation and outward diffusion. Table 11 lists the rate

Table 10.   Summary of Ideas on Exhaust H_2O + Ambient O^+ $\rightarrow$ $O(^1D)$ + H_2O^+

1) **Energetics**

   Endothermicity   0.96 eV for zero kinetic energy of the reaction products

   c.m. KE in wake-directed burns   0.45 eV

               in ram burns   5.7 eV

   (The Imaging Spectrometer saw $O(^1D) \rightarrow O(^3P)$ red line emission primarily ahead of STS-41)

2) **Yield**

   Ram energy deposition rate per PRCS engine (c.m. system) 30×10^6 w

   Yield of red-lines radiation, from AMOS spectrum data   10 – 100 w

   Maximum yield if all ionospheric O^+ ions in the ram glow volume $\rightarrow O^1D$ atoms   30 w

   (Assuming 2×10^5 O^+/cm^3, no quenching of the 150-s radiative lifetime state)

3) **Lifetime**

   The short ($\leqslant$ 1s) persistence of the red lines in the AI/S-AATS spectrums is most probably due to the combined effect of quenching of $O(^1D)$ by the dense exhaust gas (see Table 11) and diffusion of $O(^1D)$, which reduce the radiances below the threshold of the instrument

4) **Consequences**

   The yield of $O(^1D)$ radiation

   --would be independent of the number of PRCS engines operating ($[O^+]$ limits the reaction rate)

   --would be proportional to the ionospheric electron (O^+) density, which in turn varies with *sza, season, latitude, solar cycle*

5) **Further Measurement**

   Filter imaging to determine the spatial distribution of the luminosity in the oxygen red lines

coefficients and main product species of quenching by the thruster exhaust gases and ambient oxygen atoms. (These are generally accepted values from Ref's 23-26 and the references therein; the partial rate coefficients and temperature dependences in particular remain in question.) The ~6 x 10^{25} molecules exiting per second (from two largely-parallel PRCS engines) into a quasiconical volume of effective length 3 km and radius 1 km (~2 x 10^{15} cm^3) result in a mean density of very roughly 3 x 10^{10}/cm^3, which since the deactivation rate coefficients are of the order of 10^{-10} cm^3/s as (Table 11 shows) would result in the observed less than about 1-s lifetime of O(^{1}D) atoms. As the diffusion coefficient in air at this particle concentration is approximately 10^{10} cm^2/s, the characteristic transport distance in 1 s is approximately 2 km, and therefore outward diffusion also plays some part in reducing the column densities of metastable oxygen within the instantaneous fields of the cameras and spectrograph.

This collisional deactivation of the major fraction of the O(^{1}D) atoms would result in production of the further species listed in Table 11, in numbers at least an order of magnitude greater than the total number of 6300-6364Å photons that emerge from the exhaust-interaction volume. The quenching reactions represent a second potential source of visible and infrared radiations, in particular since some of the remaining translational energy of the O(^{1}D) atoms and the exhaust species would be converted to internal excitation. For example, vibrationally-excited OH could be produced by the reactions of O(^{1}D) with the relatively abundant H$_2$O and H$_2$ molecules of the exhaust.

The individual and coadded STS-41 emission spectra show no evidence of the OI (^{1}S → ^{1}D) forbidden green line at 5577.3Å, although its upper state is also energetically

Table 11. Collisional Depopulation of O^{1}D by Exhaust Gases

Quenching Species	Rate Coefficient*	Product Species, Energy
H$_2$O	3.5 x 10^{-10}	Principally 2OH, some O$_2$(a) and (b)
N$_2$	2.4 x 10^{-11}	Average v of N$_2$ is 1.2; much KE
CO	7 x 10^{-11}	All vibrationally-excited CO and KE
CO$_2$	6 x 10^{-11}	Some O$_2$ (a) and (b) + CO; much KE
H$_2$	3 x 10^{-10}	OH + H
O	8 x 10^{-12}	2 O(^{3}P), KE

* Consensus from Ref's 23-26, cm^3/s at ~300K; generally decreasing with increasing temperature, except H$_2$O.

accessible in collisions of the four principal exhaust species mentioned above on O atoms in ram-directed thruster firings--and furthermore, the transition rate is some 200 times that of $O(^1D \rightarrow {}^3P)$. The (noisy) spectrum data indicate that the mean column intensity in the green line must be less than about 1/10 that of the red doublet, so that the initial column-concentrations of $O(^1S)$ are three orders of magnitude less than those of $O(^1D)$.

We note also that excitation of $O(^1D)$ from MMH reactions appears improbable, and that the deactivation of $N_2(A)$ by $O(^3P)$ is not known to branch significantly to $O(^1D)$ despite the fact that the reaction is spin-permitted.

Interpretation -- Longer Wavelength Features

The broad maxima to the red of the 6320Å peak make an indifferent fit to synthetic spectra of the vibrational cascade of hydroxyl radicals (compiled by the Lunar and Planetary Laboratory), rotationally-hot ($\sim$ ¼ eV) or otherwise. Such calculated spectral distributions of course depend on the initial vibrational population assumed, as well as on the rotational development, which has not been measured from reactions of $H_2O(\bar{X})$ + $O(^3P)$ that produce OH^+. (At the low collision rates of the exhaust interaction volume the distribution of rotational states does not have time to come into equilibrium with the kinetic temperature before radiative depopulation takes place; that is, the emission spectrum shows the nascent rotational distribution.) The theory reviewed in Ref 3 (the process is of Type 1) in Section 1) indicates that in ram-directed firings the rovibrational cascade should develop from a population of up to v = 7 or 8 in the $OH(X^2\Pi)$ state from H_2O + O reactions. The STS-41 and -38 spectra do not in their present state of processing as yet have sufficient wavelength and intensity resolution to validate this idea, or to allow quantification of the infrared spectral yields in the much more probable Δv = 1, 2, and 3 transitions.

Electronic and vibrational emission from OH is commonly observed when liquid hydrazine-based rocket fuel and amine species are vented at low earth-orbital altitudes. In consequence the hydroxyl radiations could be due in part to reactions of incompletely-burned MMH, as well as to the excitative reaction of energetic H_2O molecules with $O(^3P)$ considered in Ref's 3 and 4 and the similar second-stage reaction of H_2O with $O(^1D)$ discussed in the previous subsection.

Figure 54 indicates the response of the AMOS cameras to the electronic and vibrational bands of OH. Since the Einstein coefficients of the vibrational transitions from individual upper states increase by two orders of magnitude between Δv = 6 and Δv = 4, despite the rapid falloff of sensitivity toward the red the longer-wavelength bands could be contributing a substantial fraction of the component of the video signal that comes from hydroxyl. (As is alluded to above, the initial populations of OH(v) are needed to quantify this fraction through a
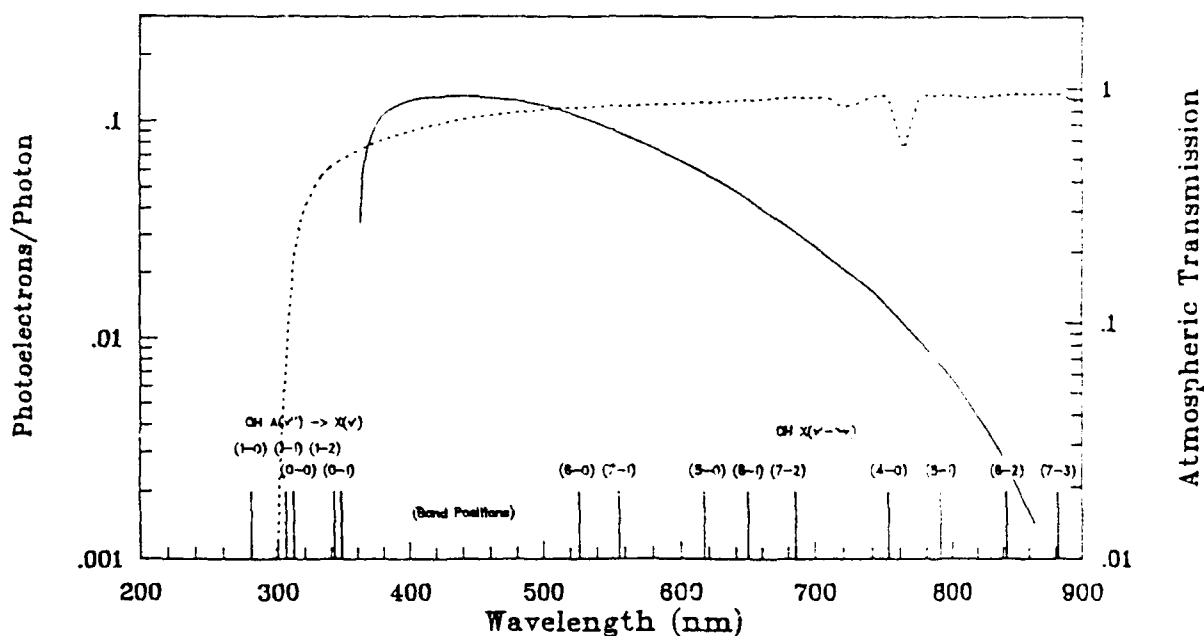
Figure 54. Spectral locations of the electronic bands (A $^3\Sigma \rightarrow$ X $^3\Pi$) and vibrational bands of hydroxyl relative to the transmission of the atmosphere above AMOS (dotted line) and response of S-20R photocathodes (solid line). The Einstein coefficients of Δv = 4, 5, and 6 OH vibrational transitions originating from the same upper state are very approximately in the ratio 100:10:1; the vertical lines are intended to serve only as markers, and the rotational development of the bands is not indicated (rotational "temperature" is not known).

calculation of the emission rates in each sequence of the vibrational cascade.) The cameras have low sensitivity to the ultraviolet electronic bands of OH (A $\rightarrow$ X), which are furthermore strongly absorbed/outscattered by the atmosphere above AMOS. (This radiation could be detected at ground stations as described in Ref 2.)

In any case, it is clear that these "red" photons do not dominate the visible emission spectrum, and indeed (as we show below) whether the features are rovibrational bands of hydroxyl or not they make only a relatively modest contribution to the brightnesses recorded by the AMOS-AATS and GEODSS video cameras. If OH (A$^2\Sigma^-$) is excited by the reaction of H$_2$O with O (see Ref 3), the (0,1) transition to the electronic ground state, whose R1 branch head is at 3428Å, would lie well within the sensor's spectral range. However, any such radiation--which is closely 1/10 as intense as the (0,0) band (outside the atmosphere)--is undetectable over the instrument-spread Q branches of NH near 3365 Å

Space and Time Dependences

The signal/noise of the individual 1-D imaging spectra of the STS-41 ram exhaust interaction (Fig. 4) is adequate for measurement of the spatial distributions of column intensity in both this NH band and the broad region extending almost to 5000Å. These patterns are shown in Fig. 53, in two different plotting modes. Both indicate that roughly one-quarter of the total feature emission measured by the spectrograph originates from Orbiter's wake region (refer to the projection of the instrument's field of regard in Fig. 3; the view is from essentially underneath the luminous volume, at an angle of 67° to the trajectory direction). Furthermore, a substantial fraction of the photocurrent appears to originate from the 3 x 16 CCD pixel segment that projects into object space to include the spacecraft body itself.

In contrast, the AATS video images in Section 3—composed by a camera also precisely tracked on the orbiting vehicle—show below-threshold radiances in this rearward area, and furthermore only weak emission from the locality of Shuttle Orbiter (the issue treated in Section 5). This discrepancy between the two optical sensors may be an effect of the limited dynamic range of the intensified camera (which clips the weak radiances), coupled with some scattering of light along the slit direction in the spectrograph (which is single-pass). It is more likely due to inaccurate pointing of the latter instrument, which is not permanently coaligned with the main MOTIF telescope as is the finder camera. Indeed, an angular offset along the slit direction of as little as 2 millirad—1/10°—would virtually eliminate the apparent signal from the wake direction.

Figure 53 shows that averaged over the PRCS firing the full-widths to half-maximum count rate in these two wavelength spans are closely 2 km, when the data segment that appears to originate from the wake direction is included. (The -8% correction for the non-normal projection to the exhaust axis is within the error of this measurement.) This spatial spread is very near the average observed in the wide spectral-band images (see Fig. 35), which suggests that light of wavelength between 3600 and 5000Å is responsible for much of the video exposure; we return to this issue shortly. Further, the observation that the emission from NH roughly tracks in 1-D space this as yet-unidentified broader-band emission suggests that similar processes are responsible for excitation of the two (or more) features of the exhaust-interaction spectrum; for example, both could be stem from the same precursor species.

Figure 55 plots the dependence on time during the firing of the numbers of photon counts in the NH peak summed over all the imaging-spectrum channels, from this same data set. As the PRCS burn begins relatively late in the first 8/10 s-duration sampling period, the apparent "rise time" is not comparable with that of the total visible sterances or maximum radiances in Fig's 19 and 51. The principal point made by these coadded spectrum data is that the total rate of emission of photons in the NH Q-branches from the -80 x 5000 m slice
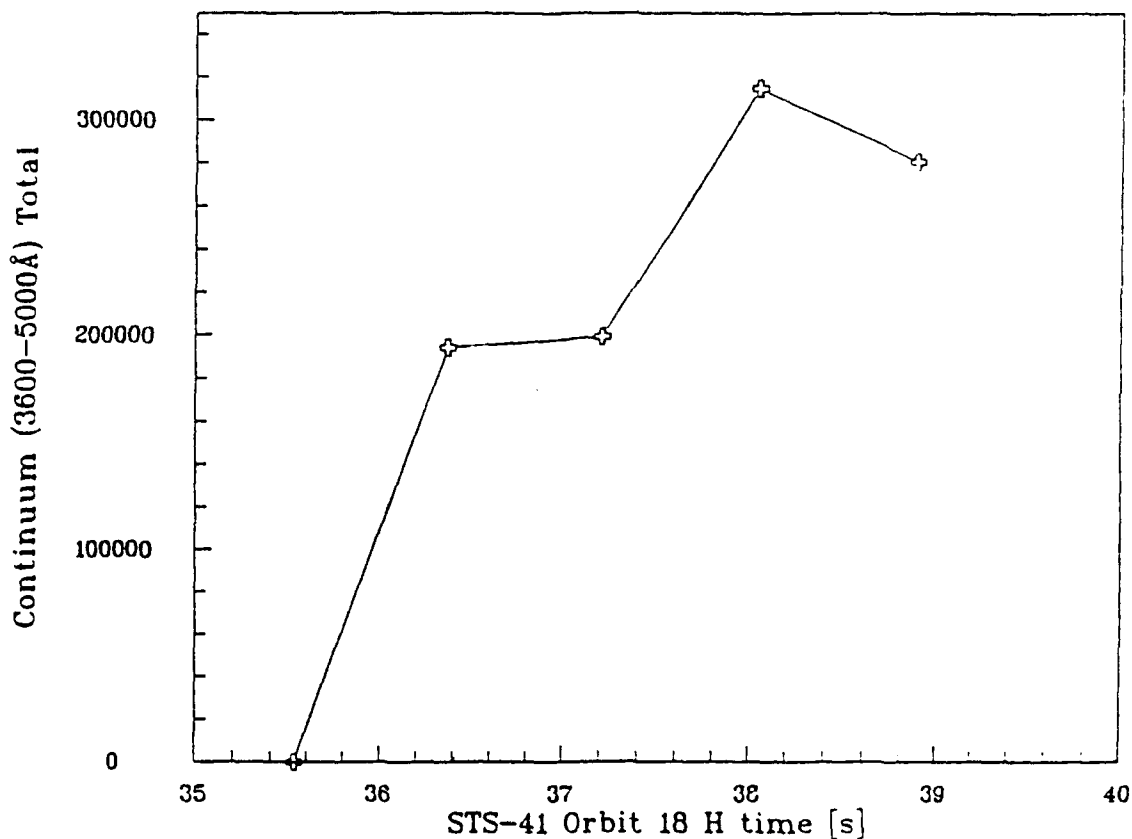
Figure 55.   Integration over the continuum-plus-bands region (3600-5000Å) of the spectrum as a function of time during the 4.25 second ram firing of STS-41.

through the exhaust-interaction volume (including the substantial fraction that appears to originate from behind the spacecraft) undergoes little change after -1 s; that is, the temporal behavior of the "line" sterance in this principal ultraviolet emission feature follows within the rather large experimental uncertainty that of the total visible ram-firing sterance measured by the AATS camera (see Fig's. 48-50).

Implications for Infrared Emission

We consider next the information about the accompanying infrared radiations that can be derived from these near-UV-and-visible spectra and the AMOS video images.

Short wavelength infrared photons would be emitted from NH in the vibrational cascade following its electronic transitions to other than its lowest vibrational state; through direct excitation of vibrational levels of its ground electronic state in formation reactions; and (to some extent) also by impact excitation of, or transfer of internal energy from other species to, NH molecules that may be present in the thruster exhaust gas. Its vibrational fundamental

86

($A \rightarrow X$) bands are below the spectrograph's threshold leads to the expectation that the concurrent infrared radiation from the direct excitation process far exceeds that which follows electronic excitation of OH(A, $v = 0$ to about 2).

Source of the AMOS Video Image Signal

Figure 56 is a plot of a composite ram emission spectrum (compiled and processed by the Lunar and Planetary Laboratory) and the wavelength sensitivity of the S-20R photocathodes of the AMOS cameras corrected for the transmission of the clear subtropical maritime atmosphere in their 67°-elevation sight path to STS-41. (We have as usual taken the
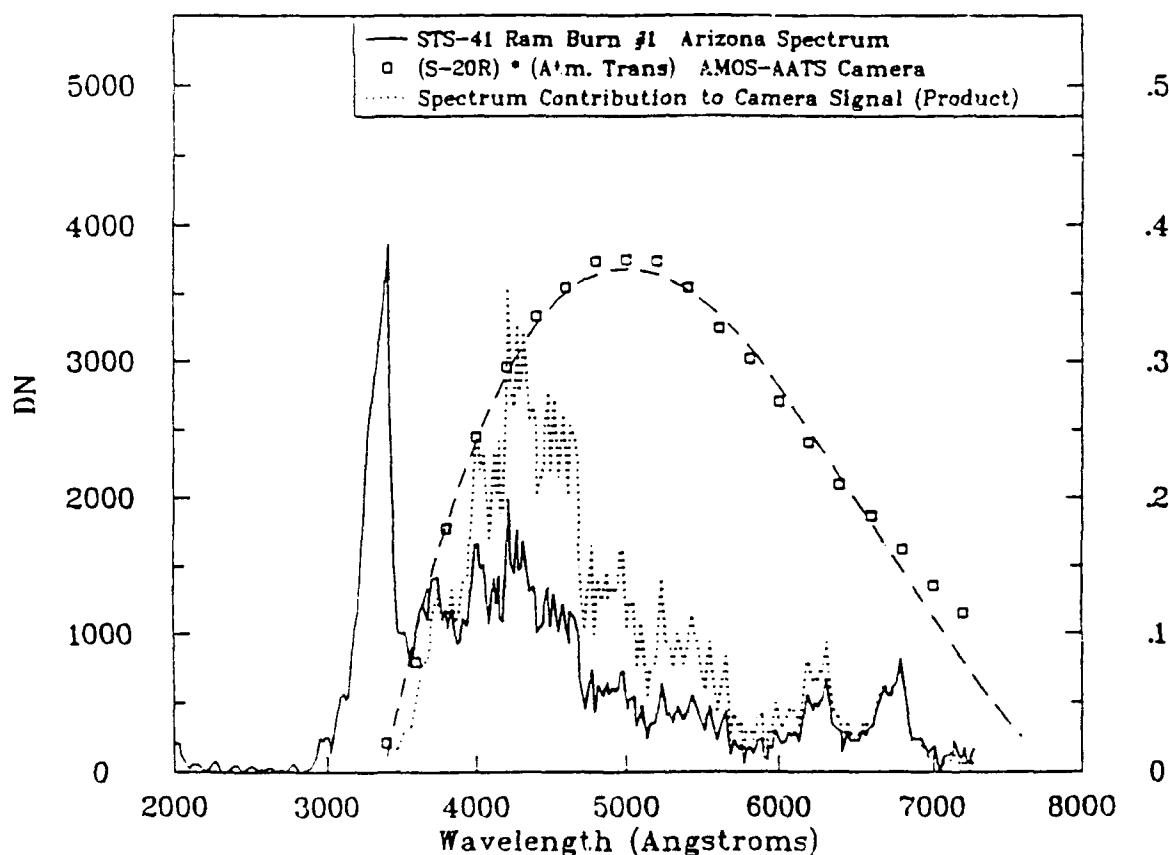
Figure 56.   Averaged emission spectrum of the STS-41 ram luminosity measured by the GD/Arizona imaging spectrograph and nominal spectral sensitivity of the AMOS-AATS camera that produced the images shown in Section 3 (photon units). The unresolved features between about 3500 and 5000Å can be seen to produce most of the video signal.

optical transmission of these largely-reflective camera systems as spectrally uniform.) With adoption of the hypothesis that the spectrum data in projections of the type illustrated in Fig. 3 indeed relate directly to the broad-spectral-range 2-D image data--as they appear from their halfwidths and time dependences to do--, the dotted line shows the relative contribution of the photons in narrow wavelength intervals to the photocurrents from the video cameras. Most of the output signal can be seen to be due to the as yet-unidentified "blue" radiations. The AMOS cameras are insensitive to the ultraviolet NH bands, and the purported hydroxyl vibrational sequences (and also the OI red doublet) beyond 6000Å appear to be making only a minor contribution to the video output. (Refer also to Fig. 54.)

Conclusions, Comments

The 1-D spatial distribution of these principal exhaust-interaction features to which the AMOS cameras respond (Fig. 56), and their near-constant emission rates (Fig. 55), are consistent with the corresponding radiometric quantities that we have extracted from 2-D video data (Fig's. 34 and 39). Error in pointing the spectrograph may be responsible for the radiation component that appears (in Fig. 53) to be coming from Orbiter's wake direction during the PRCS firing into ram. Furthermore the individual imaging spectra show no dramatic variations relative to one another in space or time. These observations indicate that the spectral intensities at visible wavelengths by and large represent the distribution responsible for the STS-33 and STS-29 video images shown in Section 3. (A caveat: the afterpulse may, as mentioned, have a different spectral distribution, unresolved because of the long (0.8-s) integration time of the instrument.)

The actinic radiation producing these video images is principally the discrete-bands-plus-apparent-continuum between about 3600 and 5000Å, some ideas on whose origin are presented above. The Q branches of the NH (A → X) $\Delta v = 0$ bands, which make a negligible contribution to the camera exposures, can be identified with confidence in the spectra; the narrow peak near 6320Å is provisionally assigned as the familiar OI ($^1D \rightarrow {}^3P$) doublet (the spectrograph's nominal 70Å resolution does not reproduce a minimum between the two emission lines with 3:1 intensity ratio separated by 64Å); and, in no small part in the absence of other plausible hypotheses, the broader red features are thought to be hydroxyl vibrational band sequences. Low signal/noise in this last region of the spectrum precludes identification of individual OH transitions (a problem complicated by their unknown rotational development), much less measurement of visible column intensities from which quantitative infrared ($\Delta v = 1, 2$, and 3) yields could be readily calculated applying the known branching ratios of the vibrational cascade. (As mentioned, synthetic spectra so far provide less than convincing evidence that these red features are indeed the OH "Meinel" bands.)

Failure to detect the (A → X) electronic bands of OH could be due to a combination of low atmospheric transmission of the (0,0) (discussed in Ref 2) and overlay of both the (0,1) and (1,1) (near 3200Å) by the very strong NH emission. We estimate from the composite ram exhaust spectrum in Fig. 52a that up to 3 kilorayleighs of (0,1)-band radiation could be unresolved under the peak centered at 3365Å; this upper limit would lead to about 50 kR of OH (0,0) outside the atmosphere, a yield rate of the same order as in the NH(A → X) feature.

As mentioned, the emission spectrum data from STS-41 and STS-38 are preliminary and largely undocumented, and hence our conclusions here remain tentative. An increase of as little as a factor 2 in radiometric signal/noise ratios--which is presumably achievable by further processing of existing spectra, and by increasing the light grasp and reducing the free spectral range in future remote sensing of PRCS exhaust-interaction volumes--would result in significant improvement in the reliability with which the emission features can be identified.

SECTION 5

VISIBLE RADIATION FROM THE IMMEDIATE VICINITY
OF THE SPACECRAFT

Introduction

We consider in this Section the PRCS operation-associated radiations from Shuttle Orbiter and the space closely surrounding it that is unresolved by the 0.5''-field AMOS-AATS camera. The visible signature of this region quite obviously applies in identifying the thruster-carrying hard body against the extended selfluminous exhaust gas interaction volumes for surveillance/tracking purposes.

When the control rocket engines are not operating, this spacecraft area is sporadically detectable above the fluctuations in dark current during the overpasses of STS-33 diagrammed in Fig. 21; indeed, the photocurrents from this stationary region of the video images are even sometimes high enough to result in undershoots of the type shown in Fig. 13b. Figure 57 shows a typical frame at approximately 1 s after the start of one of the nighttime ram firings (in sequence B of the STS-33 experiments; see Table 1), with the view projection about normal to the orbital path near culmination. The full-width to half-maximum output current from the spacecraft region can be seen to be about five picture elements. Other such "images" of Orbiter with its immediate surround appear in Fig's. 23-29 and (in particular) 46.

The initial analysis here refers to these featureless small--and in view of the finite observed halfwidths of stars, instrument-spread--patches, which can be resolved above the broad luminescence from the interaction of the exhaust through virtually all of the ram, wake, and perpendicular engine firing periods. These areas exhibit very roughly the same total sterances during each type of burn, except when the thermally-radiating rocket combustion volume itself or its reflection off Orbiter's surfaces come into the line of sight of the camera (an example is Fig. 26, in which downward-pointed thrusters were operated). As the identities of the specific thruster engines operated during the STS-33 experiments are not yet available, the dependence of these optical yields on angular orientation and position of the thruster(s) relative to the observing station remains to be addressed.

Discussion

At the typically 530-km range to Orbiter of STS-33 firings A a single video picture element of 0.5° AATS projects to 7 m. and when the irradiances at the focal plane do not saturate the CCD photodetector the characteristic scale of the "images" of the spacecraft region formed by the camera optics is (as mentioned) five pixels. While the apparent transverse

90
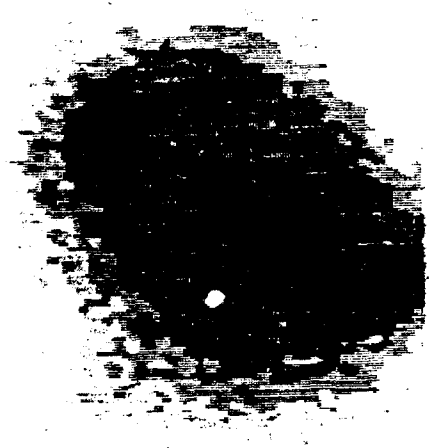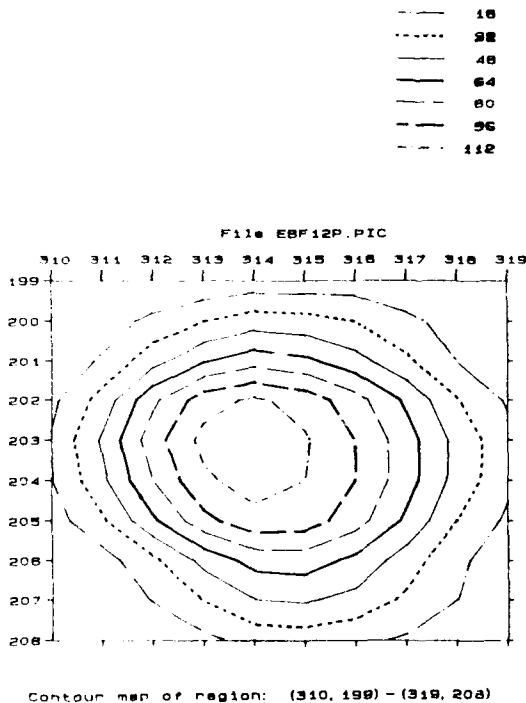
Figure 57.   a) Isophote contour plot of Shuttle Orbiter area and Ram Burn C of STS-33 at 0.3-s. b) Enlargement of Orbiter area, with local background subtracted.

width of stars--point objects--with visual magnitude ≥ 9 is also of this order, the response of the intensified-video system is such that emission from the vehicle body proper can not be deconvolved or discriminated from emission originating from the space within, say, 3 pixels or 20 m offboard. The normal atmospheric scintillation of a few arc seconds is too small to produce by itself the observed lateral spread in the video photographs.

The patterns of apparent scene radiance reproduced by the groundbased long-focus camera could thus be due to a mix of the following light sources.

1)   Luminescence from reactions of incident atmospheric species catalyzed by vehicle surfaces exposed to the ram air flow, that is, "spacecraft glow" of the type reviewed in Ref 3.

2)   Chemiluminescence from gas-phase reactions of desorbed species formed by such surface-mediated processes, taking place within approximately 20 m from Orbiter.

3)   Excitative reactions with the incident atmosphere of adsorbed exhaust gas that has directly impinged on, or was scattered onto, outer vehicle surfaces.

4)   Processes similar to Item 2) involving products of the reactions of Item 3).

5) Radiative depopulation of metastable states of combustion species.

6) A "close-in" component of the interaction of this thruster exhaust with the natural and/or vehicle-outgas atmosphere.

7a) Thermal emission from the rocket combustion chamber itself or other hot interior walls, and such radiation reflected off illuminated vehicle surfaces, when these areas are visible from the ground station (as they appear to be in "downward" parallel firings); and

7b) this intense radiation scattered off particulate matter and gases in the vicinity of the spacecraft (some of which could be associated with the PRCS firing).

8) Crew cabin and other operating lights of Shuttle Orbiter.

The sterances from all of these light sources would be enhanced by reflections off the largely-white upper exposed surfaces of space shuttle.

The spectral distribution of these locally-originating emissions would be expected to differ from that of the exhaust-interaction volumes, and furthermore the spectrum may also be different during and between PRCS firings. In consequence our comparison of radiant intensities during thruster operation (Fig. 59b) refers only to the wavelengths of instrument sensitivity and atmospheric transmission illustrated in Section 2, and is subject to the usual error in interpretation due to differences in the emission spectra.

Photographs taken by outward-viewing cameras onboard Orbiter while the PRCS is operating indicate that most of the visible light (other than that coming directly from the engines themselves, Item 7a)) originates from the surrounding space rather than the vehicle's outer surfaces. Information about the spatial distributions remains sketchy, however, in large part due to the unfavorable view projections from inside the spacecraft. Furthermore the intensities of surface glow increase during and in the few seconds after the control rocket firings, an effect (Item 3) above) that has been ascribed to recombination of (principally) backscattered NO molecules with ambient O atoms to produce the yellow-green-infrared pseudocontinuum from NO_2^*.

In this regard, the sterances in the direction of AMOS resulting from excitative reactions catalyzed by exposed windward surfaces (Items 1) and 3)) would depend on the location of these surface areas relative to the ground station. As all the scheduled STS-33 thruster firings took place when the trajectory of the spacecraft was essentially perpendicular to the line of sight, the camera has at best oblique views of its ram-facing areas; refer to Fig. 22. The observation that the sterances are of about the same magnitude during firings of thrusters toward all directions other than downward would suggest that the directly PRCS-related local luminosity is largely due to reactions taking place in the unresolved space surrounding the hard body (Items 2), 4), and/or 6)). Radiation from exhaust gases in metastable states (Item 5)) would make only a small contribution to the observed signal from this local volume, as was

indicated by a brief review of the transitions of the primary combustion-product species listed in Section 1, which failed to identify any low-lying such upper electronic states with lifetimes less than the transit time across tne volume ($\approx$ 20 m/3500 m s^{-1} or 1/175 s).

In the periods between thruster operation onboard cameras see offboard radiation originating only from the first few cm to windward, that is, "shuttle glow" caused by excitative recombination of the incident atmosphere on ram-directed surfaces (see Ref 3 and the references therein). Applying the calibration in Section 2 from GEODSS, we find that the mean irradiance at AMOS from the spacecraft region in the period between STS-33 "experiment A" burns is equivalent to that from an approximately 12th-magnitude star, roughly 2 x 10^{-17} w/cm^2. An ~1-watt isotropic source of visible light at the 530-km range would produce this weak irradiance. The column intensities (viewing outward) of the recombination glow extending from windward surfaces of space shuttle orbiting near 330 km altitude have been found to be of the order of 100 Rayleighs--10^8 photons/cm^2 s--, which leads to a total such power of less than 10^{-4} watts radiated from off the approximately 50-m^2 exposed area of the spacecraft. Thus shuttle glow (Item 1)) could not be the source of the quiescent optical signal. (This conclusion is supported by the observation that the visible radiations induced by their passage do not lead to the detection of low earth orbiting spacecraft at night by GEODSS, or by telescopes used for astronomy.) The normal lighting of space shuttle's work area (Item 8)) would appear to be a more reasonable explanation of the "baseline" irradiances; it furthermore can at least qualitatively explain the observed variations in irradiance between thruster firings--as the exposure of crew cabin windows toward AMOS changes, for example.

Thermal radiation from the ~10^7-watt power output PRCS thrusters themselves (Item 7)) is of course a further potential source of visible signal. Large photocurrents would result from even oblique camera views into a ~3000K reaction chamber, or of Orbiter surfaces that "see" such volumes, as is evidenced by the off-scale irradiances in downward perpendicular-to-track thruster firings (Fig's. 26 and 28).

Data

With this notable exception, the area integrals of irradiance from the image patches surrounding spatially-unresolved Shuttle Orbiter appear roughly the same during PRCS thruster firings toward the three directions. We reduced the photocurrents relating to ram burn A (Fig's. 22 and 23, and top diagram in Fig. 21), subtracting the dark-current baseline measured just before the experiment took place. Figure 58 plots the resulting digitized pixel values over a 40-second period extending to just before the planned succeeding wake firing. Early in this data segment an unscheduled (for the experiment) ~3-s operation of what may
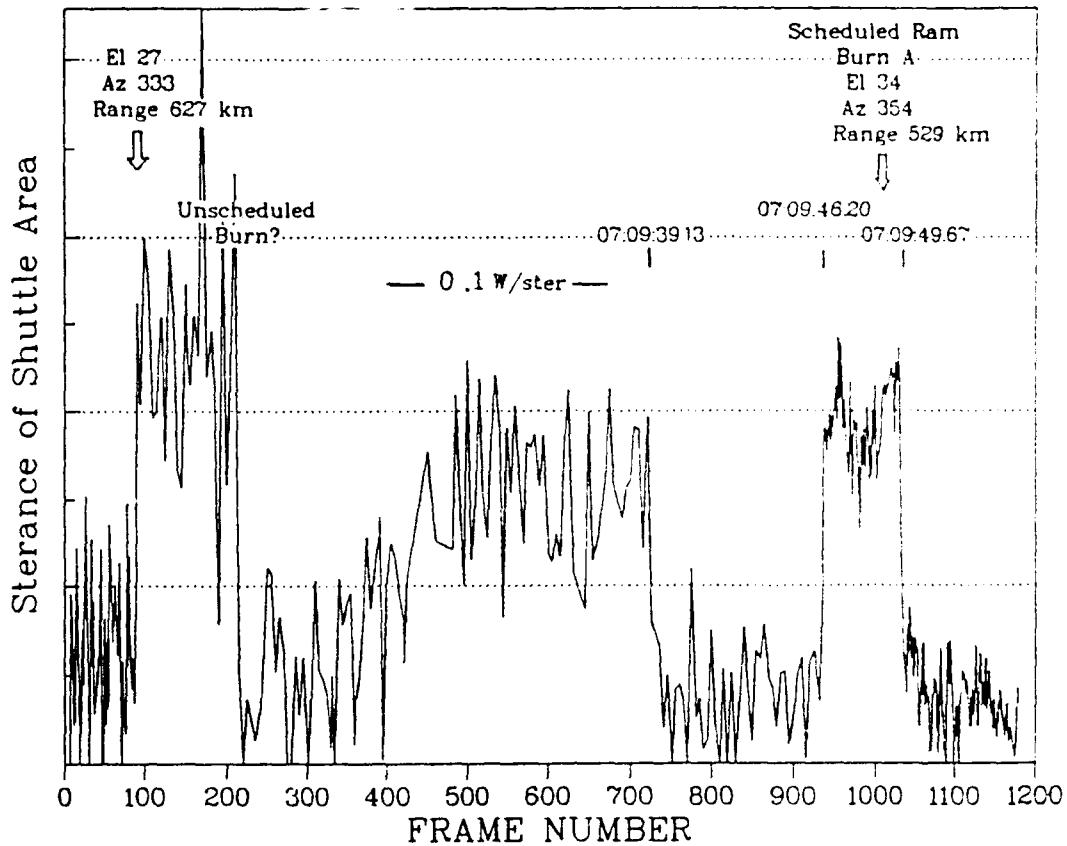
Figure 58.   Space-integrated photocurrents from the region surrounding Shuttle Orbiter in connection with Ram Burn A (Table 1), with averaged pre-firing baseline subtracted. Each video frame before the unscheduled (for the experiment) firing of what may have been a vernier or PRCS aspect-controlling thrusters is reduced; each fifth frame during this earlier burn and in the -22-s period until ram burn A is reduced; and each frame during the ram firing and in the succeeding -5 s is reduced. The variability indicates the precision of the image data reduction. Refer also to Figure 59 and 60.

have been a PRCS or a vernier (40 kgf) aspect-controlling thruster occurred; the video images show a weak, diffuse luminosity not inconsistent with a wake hemisphere-directed PRCS burn. While this firing near 07:09:19 (see Fig. 58) may have been intended to orient Shuttle Orbiter so that its thruster engines could be operated in the exhaust directions desired, the pitch-roll-yaw angles of the vehicle in fact change only negligibly in the period between the unscheduled and experiment ram burn.

Figure 59 presents an enlarged view of the sterances during and after the planned firing, and a comparison with the corresponding total yield rates per unit solid angle from the much larger rocket exhaust gas interaction volume. Figure 60 is a further gross enlargement of the radiometry data for the period immediately following turnoff of the engines. The

94
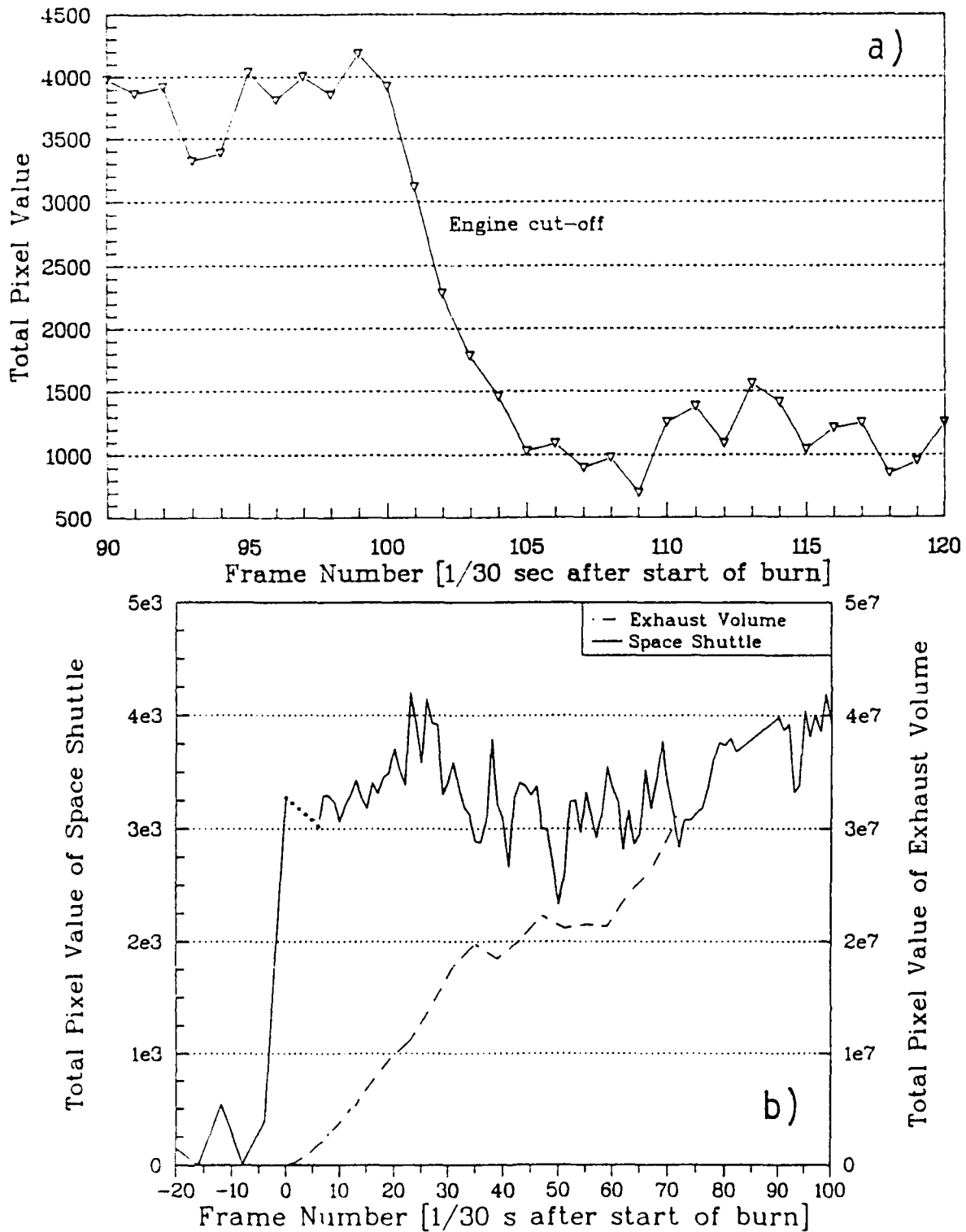
Figure 59.   a) Sterances from the Orbiter-containing volume, with each video frame reduced during and after the ram-directed engine firing. b) Comparison of irradiances from this unresolved local volume and the ram exhaust-interaction volume. The small area is unresolvable where the dotted line segment appears.

95
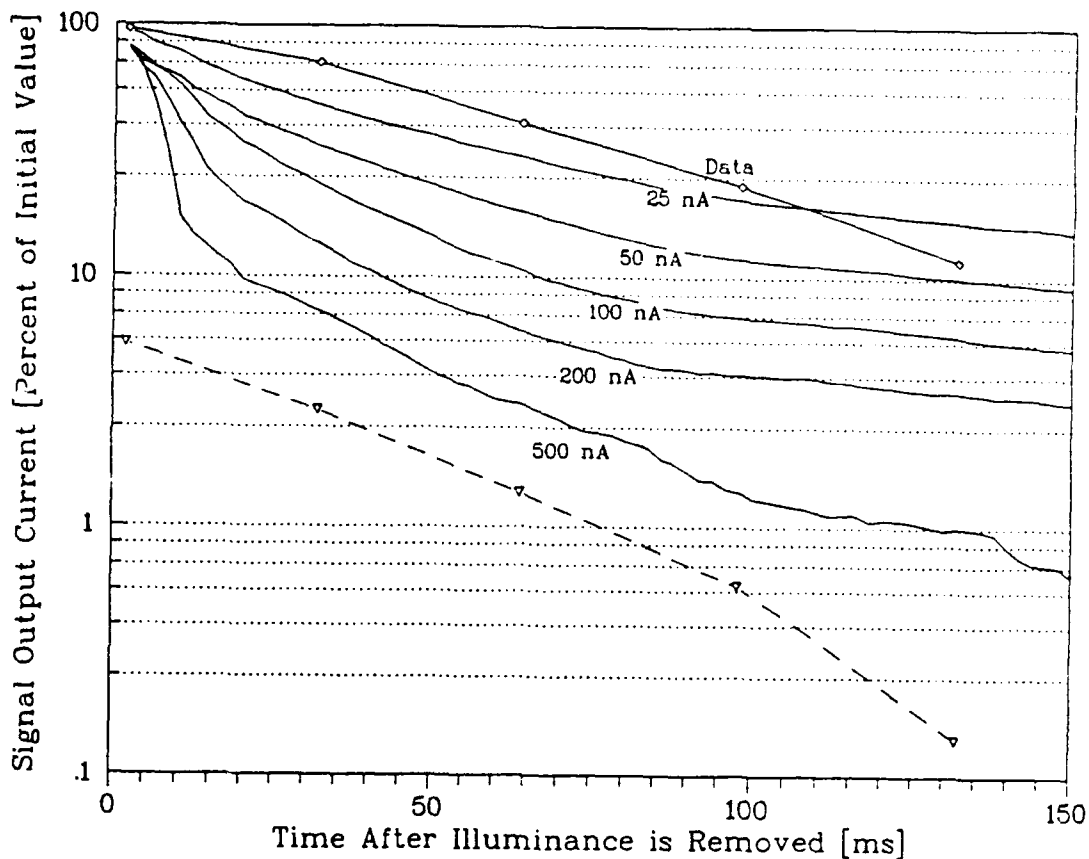
Figure 60. Comparison of sterance from the Shuttle Orbiter area after engines turnoff, with RCA data on the persistence of 4849/H series ISIT camera tubes. Photocurrent baseline for the sterances was taken as the average of Frames 106-110 (see Fig. 59). The dashed line at lower left is the relative sterance after correction for instrument persistence as described in the text.

variability among results from nearby frames in Fig. 59 is a measure of the precision of these derived sterance values. The principal features of these plots are as follows.

--Before the unscheduled thruster firing, the sterance from the region that includes the spacecraft remains sensibly constant (at about 0.02 w/steradian). The NASA housekeeping data show the orientation of Orbiter--and its crew cabin windows--to be changing very little during this brief period.

--At the start of the unscheduled firing, this sterance increases by a factor 3 or 4 (only) within one video frame, and at the end it rapidly decreases to essentially its previous value. In the scheduled PRCS firing, a similar rapid rise in light output is observed, but to only about 80% of that of the earlier burn. The initial very steep decline upon turnoff illustrated in Fig. 59a is followed by a slow further decrease (with what appears to be ~3 s characteristic decay time).

96

Figure 60 compares on a time-stretched, logarithmic scale the decrease in sterance in the ~1/10 s after the PRCS shuts off with the persistence of output current from RCA 4849/H series ISIT camera tubes (from the manufacturer's data) following irradiances that produce currents between 25 nanoamperes and about-saturation 500 na. (The nominal dark current from the AMOS video camera under the operation conditions of the experiment exceeds 25 na.) The maximum photocurrents in the "image" of the spacecraft area are near the high end of this dynamic range. Application of these RCA performan. . data indicates that the decay of sterance is a real effect. We deconvolved its magnitude from the logarithmic slopes of the currents, by working backward from the "end" of the steep decay at 4 video frames after the engines turn off. This rough procedure--which involves judgement of the mean output current to be adopted in making the correction--led to the relative sterances from the Shuttle-Orbiter area shown by the curve at lower left in Fig. 60. The decrease in the first 100 ms is found to be approximately logarithmic, with a characteristic time of 0.05 s $\pm$ 0.05 s.

--After the unscheduled firing and rapid return to photocurrent baseline, the sterance increases for several seconds, levels out, and then abruptly drops to near or below the video system's threshold. This behavior could result from a change in the projection to AMOS of the windows of the illuminated crew cabin, perhaps associated with the changing azimuth of Orbiter (as mentioned, the spacecraft does not rotate during this period, and maintains the orientation illustrated in Fig. 22). Alternatively, these variations may be an artifact of the gain control of the ISIT video system (upward drift followed by a discrete decrease); too few identifiable stars are in the narrow field of view of the AMOS camera to allow checking of this hypothesis. A still further possibility is that Orbiter's cabin lighting is being adjusted, which could account for the rapid decrease in optical signal.

--During the period that the PRCS thrusters operate, the sterance is somewhat less than that during the unscheduled burn that occurred 26 s earlier. This relatively high signal from the unplanned event can be interpreted as two simultaneous firings of PRCS thrusters. Alternatively, if the first firing was that of a vernier control engine this near-equality would indicate that some saturation effect is taking place, perhaps stemming from the fractional coverage of the spacecraft's surface by backscattered exhaust species that react with incident oxygen atoms. While the slow decay following steep falloff after the identified engine burn could be evidence that the first-fired thruster is of a different type, this decrease in sterance is on the other hand conceptually no different from the increase during the long period starting just after the earlier firing; or, it may be related to the reported rotation of Orbiter's body that was induced by the operation of the (aspect-controlling) thruster.

--During both firings, the sterance remains constant within the precision of the image data. That is, no transient or hysteresis effects are evident.

--These sterances from the immediate vicinity of Orbiter are four orders of magnitude smaller than those from the "steady-state" ram exhaust-interaction volume (see Fig. 59b). Even in the first video frame in which the latter luminescence appears its total light yield is much greater than that from the unresolved spacecraft area. The apparent maximum surface brightnesses of the two separated regions, in contrast, are not substantially different.

Conclusions, Recommendations

The finite spatial spread in the AATS images of the photocurrents from the region surrounding Shuttle Orbiter at 330 km altitude could be either due to real off-surface light emission or an artifact of the camera optics. The number of visible photons (or more specifically, those to which S-20R type photoemissive cathode arrays respond) from this area is very small in comparison with the total from the interaction volumes of PRCS combustion-product gases exhausted toward ram, perpendicular to the trajectory, and even into the wake. Nonetheless since the equivalent radiances are comparable, in ram and perpendicular-to-track firings the physical separation of this small patch from the typically 10^4-times larger projected area luminescence would allow its detection by high spatial-resolution imaging systems--at least in view projections in which it does not overlie the interaction volume (as in the STS-33 experiment). In view of the uncertainties in the infrared radiances from reactions of exhaust products with the atmosphere and--in particular, since the mechanisms exciting the visible emission are even less well understood--from the volume of space that includes Orbiter, little can now be inferred about the prospects for discrimination-detection of the hard body by imaging sensors operating at infrared wavelengths.

The visible sterance in the periods between thruster firings would not be due to so-called spacecraft glow or persisting luminescence of metastable exhaust products, and is instead consistent with being from the space vehicle's housekeeping and indicator lights. The corresponding infrared signal would then be directly derivable from the emission spectrum of this onboard illumination and its transmission through Orbiter' windows and the air along the sight path (for endoatmospheric sensors). Lack of information about the contribution to the irradiances at the ground station from this variable-sterance onboard "beacon" precludes reliable interpretation of the few-seconds persistence of (some of) the visible signal after the single firing of thrusters considered here. The -1/10-second initial persistence component apparent in Fig. 60 is in contrast most likely a real effect of the thruster exhaust.

We recognize that this analysis of the locally-originating radiant intensities before, during, and immediately after only one of the programmed PRCS firings raises at least as many questions as it answers (even without considering the issue of which engines were operated). Nonetheless despite the obvious limitations of our data interpretation the absolute

yields of visible light, and their comparison with those from the air volumes where the exhaust interacts, provide a heuristic basis for planning optical surveillance of Shuttle Orbiter and other space objects whose aspect and/or trajectory are controlled by liquid-fuel MMH-N_2O_4 thruster engines.

Further critical information about the optical signature of Orbiter plus its immediate surround can readily be derived from the large unreduced database on scheduled PRCS firings (Table 1). For exampl the patterns of slow change between burns and the effect of the view projection from AMOS could be clarified, the two temporal-components luminosity that appears to follow the ram burn investigated, and systematic differences among sterances in the three directions of the exhaust gases (and between individual overflights of Orbiter) quantified. When the specific thrusters operated become identified the contribution to the sterances from thermal radiation originating in the rocket engines, and possibly also from the cabin lights, can be assessed; this information applies directly in extrapolating this AMOS-AATS visible light data set to infrared-surveillance wavelengths.

Future images from the groundbased video camera in its $0.1°$ field-of-view mode would serve to separate the on- and off-surface components of this optical radiation, which besides locating the spacecraft within the visible image patch(es) could lead to identification of the principal excitation process(es) and thus provide information about the infrared signature of the hard body. In addition control should be exercised over the lighting of Shuttle Orbiter's crew cabin and payload bay during future thruster firing experiments.

We note in conclusion that a straightforward calculation shows that the conventional (silver-halide) color photography with tracked AATS-like cameras would readily identify the color(s) of both the close-in luminosity associated with PRCS operation and--even more important--that of the thruster exhaust interaction volume. Such rough "spectrum" information could of course also be derived using narrow wavelength band-isolating filters in the existing AATS or other long-focus video cameras.

SECTION 6

SUMMARY, RECOMMENDATIONS

This report has characterized the spatial, spectral, and temporal distributions of the optical radiations produced by the interaction between the exhaust products of space shuttle's liquid-fueled PRCS engines and the orbital residual atmosphere. Section 3 reviews the geometry of the visible glows that resulted from a standard set of thruster firings near culmination of STS-33 as measured by long focal-length cameras at AMOS, and Section 4 analyzes preliminary near UV-visible imaging spectra from a new electro-optical sensor at that mountaintop observatory. We focused on the ram-directed exhaust, which has the most kinetic energy available for chemiluminescent reactions and which produced near-symmetric and thus relatively conveniently analyzed emission patterns. A significant fraction of the total sterance from the interaction volumes arises from beyond the 0.5°-diagonal field of view of the high-resolution AATS tracking camera; the 6° field of the essentially stationary GEODSS auxiliary camera at AMOS provides useful further information about the brightness distributions produced by thruster firings toward Orbiter's wake and perpendicular to its trajectory.

The order-of-magnitude greater emission yields from the windward and perpendicular firings than from those directed into the vehicle's wake--a best-estimate ratio is 10:5:1--show that the translational energy of the combustion-product gases plays a critical part in reactions from which emerge species in radiative upper states. The essentially Gaussian shape of the spatial distribution from ram burns and the similarly broad transverse spread in the perpendicular firings, along with the ~kms physical separation of the thruster engines from the luminous air volumes, suggest that elastic scatterings are slowing the exhaust molecules to relative velocities at which the excitation cross-sections are higher than at their initial speeds (beyond a threshold indicated by the weak wake radiation). (This separation is explained by the SOCRATES code calculations, which input cross-sections that increase monotonically with energy, as being due to depletion of the ambient atomic oxygen reactant by chemical consumption and shock effects.)

The velocities of the "fronts" of the outward-expanding radiating volumes were about as expected from the known (3½ km/s) directed velocity of the exhaust gases from PRCS rocket engines. Maximums in radiance and total sterance are approached within about 1 s, after which the emitting region, which appears to move at the spacecraft velocity, expands (and otherwise changes) only slowly. A distinct afterpulse associated with shutoff of the engines, which is particularly pronounced in the < ¼-s duration STS-29 firing into the ram hemisphere, moves outward at about half the speed of the main radiation pulse. We interpret

100

this transient brightness enhancement as the result of a short-lived increase in the fraction of unburned (or partially-burned) monomethyl hydrazine fuel--a known characteristic of this type of rocket engine--, which rapidly reacts with the atmosphere's oxygen atoms. Similarly in the period within ~¼ s of turnon of the STS-33 thrusters a "finger" of increased surface radiance can be seen to extend outward from the spacecraft into the larger luminous volume, an effect that most probably stems from the same chemiluminescence process(es).

Some of the AMOS-AATS and -GEODSS video data were absolutely calibrated against the irradiances from known stars, with a model clear atmosphere adopted for calculating the sterances of the visible glows that would be measured from exoatmospheric sensor platforms. The 0.5°-field Orbiter-tracking camera produced longer than anticipated streaked images of stars, whose use as irradiance standards leads to much smaller sterances of the exhaust interaction volumes than were similarly measured by the 3°-field AATS and the 6° GEODSS (star field-tracking) cameras. Reasonable agreement was found in a comparison of the total sterances from thruster firings of different durations and on different shuttle missions. The fraction of the 20-megawatt kinetic energy of the thruster exhaust radiated in the S-20R spectrum band (essentially, the visible wavelength range) by the reactions of the combustion product gases--including unburned fuel and oxidizer--was about 10^{-5-4} in wake firings and 10^{-4-3} in ram; refer to Table 6.

One definite, a few highly probable, and several possible sources of this actinic radiation could be identified from the preliminary, incompletely-reduced spectral data on ram firings from STS-41. Electronic bands of the NH radical centered at 3365Å (with some emission in other branches of these $\Delta v = 0$ transitions) are the dominant discrete feature in these space-resolving spectra. Several exothermic or slightly endothermic reactions with ambient oxygen of fragments from partially-burned MMH could be responsible for this luminescence. The forbidden red doublet of atomic oxygen $O(^1D - {}^3P)$ also appears to be present, most likely primarily excited by electronically nonadiabatic collisions of the abundant exhaust N_2, H_2O, CO_2, and CO molecules on atmospheric $O(^3P)$. The < 1-s decay time of the population density of $O(^1D)$ after the thruster engines shut off shows that oxygen atoms in this low-lying excited state are rapidly collisionally quenched by the exhaust gas; thus through their deexcitation reactions (Table 11) these atoms would produce further radiations in several infrared molecular vibrational bands.

Hydroxyl vibrational emission was expected on theoretical grounds (see Ref 3), and may in fact also be contributing to the total from the exhaust interaction. We estimated by a straightforward cascade calculation the infrared radiant intensities from the $\Delta v \leq 3$ transitions of OH, starting from a preliminary identification of the features near 7500Å and 6200Å as its $\Delta v = 4 - 6$ bands; about 500 times as many photons are emitted in its fundamental and first

two overtones as in the shorter-wavelength sequences to which the imaging spectrograph responds. Hydroxyl radiation could also be arising from reactions of $O(^1D)$ with the abundant water vapor of the rocket exhaust, as well as from the previously-considered collisions of high kinetic energy H_2O on ambient $O(^3P)$.

A major fraction of the total radiation in the S-20R wavelength region was found to be in a quasi-continuum overlaid by discrete bands at the blue end of the spectrum, and indeed most of the video exposure is due to this feature. Table 9 identifies the radiative upper states that we considered as its possible sources; these may be excited by energy transfer from longlived $N_2(A^3\Sigma^+)$ molecules present in the rocket exhaust, or in part by the familiar CO-O reaction. The imaging spectra so far suggest that the spatial distributions of both this broad feature and the strong narrow peak centered at 3365Å are similar to those in the wide wavelength-span video photographs. Further processing of the existing spectrum data would improve the reliability of identification of the emitting species, and should precede further spectrographic measurements.

We also briefly investigated (in Section 5) the optical signature of the region of space immediately surrounding and including Shuttle Orbiter, which is of obvious interest for space surveillance. The sterance from this unresolved small segment of the scene during ram-directed PRCS firings is typically 10^{-4} that of the exhaust-interaction volume [in the S-20R spectrum band], while its maximum apparent radiance--after it has been spatially spread by the video camera--was approximately the same as that of this volume. The angular resolution of the 0.5^o-field AATS is insufficient to discriminate the hard body against the luminosity of the region surrounding it; use of this camera's 0.1^o-field option may discriminate between the two areas to determine the contribution to the luminosity of surface-catalyzed chemiluminescence, natural decay of metastable species in the thruster exhaust, scattering of light emitted from the combustion chamber of a PRCS engine, or some close-in component of the exhaust's interaction (for example with the space vehicle's outgas cloud). Since the radiant intensity of the small local patch does not appear to depend on the direction of thruster firing the excess light may be coming from the extended (~30 m radius) volume around the spacecraft. This emission appears to persist for about 1/10 s after the thrusters are turned off. The variable sterance from the spacecraft area between thruster firings may be due to the routine operation of cabin or payload lighting being detected by the AMOS camera; such interfering light sources (they have stellar magnitude ~9) should be controlled during future thruster-firing experiments.

REFERENCES

1. I. L. Kofsky, N. H. Tran, M. A. Maris, and C. A. Trowbridge, Measurement of Optical Radiations in the Spacecraft Environment, *Scientific Report No. 1*, GL-TR-89-0168, 15 June 1989, ADA213814.

2. I. L. Kofsky, N. H. Tran, M. A. Maris, D. L. A. Rall, and C. A. Trowbridge, Photometric-Photogrammetric Analysis of Video Images of a Venting of Water from Space Shuttle Discovery, *Scientific Report No. 2*, GL-TR-90-0187, 15 June 1990, AD A233452.

3. I. L. Kofsky, J. L. Barrett, T. E. Brownrigg, P. J. McNicholl, N. H. Tran, and C. A. Trowbridge, Excitation and Diagnostics of Optical Contamination in the Spacecraft Environment, AFGL-TR-88-0293, 01 Jul 1988, ADA202429.

4. E. Murad, D. J. Knecht, R. A. Viereck, C. P. Pike, I. L. Kofsky, C. A. Trowbridge, D. L. A. Rall, G. Ashley, L. Twist, J. B. Elgin, A. Setayesh, A. T. Stair, Jr., and J. E. Blaha, Visible light emission excited by interaction of space shuttle exhaust with the atmosphere, *Geophys. Res. Lett.* 17, 2205-2208, 1990.

5. J. B. Elgin, D. C. Cooke, M. F. Tautz, and E. Murad, Modeling of atmospherically induced gas phase optical contamination from orbiting spacecraft, *J. Geophys. Res.* 95, 12,197-12,208, 1990.

6. C. P. Pike, D. J. Knecht, R. A. Viereck, E. Murad, I. L. Kofsky, M. A. Maris, N. H. Tran, G. Ashley, L. Twist, M. E. Gersh, J. B. Elgin, A. Berk, A. T. Stair, Jr., J. P. Bagian, and J. F. Buchli, Release of liquid water from the space shuttle, *Geophys. Res. Lett.* 17, 139-142, 1990.

7. I. L. Kofsky, Excitation of N_2 Lyman-Birge-Hopfield bands emission by low earth-orbiting spacecraft, *Geophys. Res. Lett.* 15, 241-244, 1988.

8. H. Trinks and R. J. Hoffman, Experimental investigation of bipropellant exhaust plume flowfield, heating, and contamination and comparison with the CONTAM computer model predictions, in *Spacecraft Contamination: Sources and Prevention*, J. A. Roux and T. D. McCay (eds.), AIAA, New York, 1984.

9. J. S. Pickett, G. R. Murphy, W. S. Kurth, C. K. Goertz, and S. D. Shawhan, Effects of chemical releases by the STS-3 Orbiter on the ionosphere, *J. Geophys. Res.* 90, 3487-3497, 1985.

10. R. J. Hoffman, A. Kawasaki, H. Trinks, I. Bidermann, and W. Ewering, The CONTAM 3.2 Plume Flowfield Analysis and Contamination Prediction Computer Program: Analysis Model and Experimental Verification, *AIAA 20th Thermophysics Conf.*, AIAA-85-0928, Williamsburg, VA, 19-21 June 1985.

11. H. Trinks, Bipropellant engines surface contamination and heating effects, *AIAA 21st Joint Propulsion Conf*, Monterey, 8-13 July 1985.

12. E. Wulf and U. von Zahn, The shuttle environment: Effects of thruster firings on gas density and composition in the payload bay, *J. Geophys. Res.* 91, 3270, 1986.

13. R. E. Meyerott, G. Swenson, E. L. Schweitzer, and D. G. Koch. Excitation of the low lying vibrational levels of H_2O by $O(^3P)$ as measured on Spacelab 2, *Proceedings of the Vehicle Interaction Conf.*, Johns Hopkins Applied Physics Laboratory, 11-13 March 1991.

14. P. A. Bernhardt, W. E. Swartz, M. C. Kelley, M. P. Sulzer, and S. J. Noble, Spacelab 2 upper atmosphere modification experiment over Arecibo. 2. Plasma dynamics, *Astrophys. Comm. Lett.* 27, 183-198, 1988.

15. I. L. Kofsky, D. P. Villanucci, and E. R. Huppi. Preliminary Report on Aircraft Measurements of Optical/IR Afterglows from a Major Ionospheric Perturbation, in *Proceedings of the Workshop/Symposium on the Preliminary Evaluation of the Ionospheric Disturbances Associated with the HAEO-C Launch, with Applications to the SPS Environmental Assessment*, M. Mendillo and J. Baumgardner (eds.), Conf. 7911108, August 1980.

16. R. A. Dressler, J. A. Gardner, D. L. Cooke, and E. Murad. Analysis of ion densities in the vicinity of space vehicles: Ion-neutral chemical kinetics, *J. Geophys. Res.*, in press, 1991.

17. M. Heninger, S. Fenistein, G. Mauclaire, and R. Marx. Review of the reaction of O^+ with H_2O and its bearing on composition measurements from the space shuttle, *Geophys. Res. Lett.* 16, 139-141, 1989.

18. K. H. Becker and K. D. Bayes, A study of the chemiluminescence from oxygen atom-hydrazine flames, *J. Phys. Chem.* 71, 371-375, 1967.

19. *AMOS User's Manual*, Revision 7, AERLM 1176, May 1989.

20. W. H. Warren, Jr., Documentation for the Machine-Readable Character-Coded Version of the Sky Map Catalogue, NSSDC/WDC-A-R&S, 81-05, July 1981.

21. A. S. Jursa (ed.), *Handbook of Geophysics and Space Environments*, AFGL-TR-85-0315, Chapter 25, 1985, ADA167000.

22. R. Viereck (PL/GD/WSSI), private communication, 1991.

23. G. E. Zahr, R. K. Preston, and W. H. Miller. Theoretical treatment of quenching in $O(^1D) + N_2$ collisions, *J. Chem. Phys.* 62, 1127-1135, 1975.

24. J. C. Tully, Reactions of $O(^1D)$ with atmospheric molecules, *J. Chem. Phys.* 62, 1893-1898, 1975.

25. G. E. Streit, C. J. Howard, A. I. Schmeltekopf, J. A. Davidson, and H. I. Schiff, Temperature dependence of $O(^1D)$ rate constants for reactions with O_2, N_2, CO_2 O_3, and H_2O, *J. Chem. Phys.* 65, 4761-4764, 1976.

26. F. Gilmore (R&D Associates), private communication, 1991.